technische universität
dortmund

Fluorescence microscopy studies on the fibrillation of IAPP at model and cellular lipid interfaces - from mechanism to potential strategies in type II diabetes mellitus

Dissertation zur Erlangung des Doktorgrades

der Naturwissenschaften

(Dr. rer. nat.)

eingereicht beim

Fachbereich Chemie
der Technische Universität Dortmund

von

M.Sc. BMB Diana Radovan

aus Timişoara, Rumänien

2009
Dortmund

First Referee: Prof. Dr. R. Winter

Second Referee: Prof. Dr. H. Rehage

Acknowledgements

I would first of all like to express my gratitude towards Prof. Dr. Roland Winter for giving me the chance to further develop my interest in lipid research and cytotoxicity tests, but also to become familiar with and get specialized in the fascinating area of amyloidogenic proteins and diseases, as well as in advanced imaging techniques.

I would particularly like to thank Dr. Norbert Opitz from MPI Dortmund, for his help and experimental support in performing the confocal and two-photon excited microscopy experiments. Thanks to Dr. Claus Csezlik for his constant experimental advice and useful discussions. I would also like to thank Dr. Nagarajan Periasamy for guiding my first steps in the field of GUVs, Andrea Gohlke who was actively co-involved in the development of the cell culture lab, Dr. Rajesh Mishra for many useful discussions in the field of amyloids, Dr. Vytautas Smirnovas, Dr. Katrin Weise and Suman Jha for getting me familiar with FT-IR, CD spectroscopy and AFM. I am grateful to Christian Denter for his contribution in optimizing the electroformation protocol on ITO slides for our newly developed ITO chamber during his master thesis work in our group. To all the group members for creating a nice working environment and giving me the chance to practice my German day by day, especially my office mates Bertina Schuppan and Dr. Lally Mitra, and to Jonas Markgraf and Daniel Sellin for correcting the german summary of this thesis. I would like to thank Dr. Gurpreet Singh, Dr. Nadeem Javid, Dr. Karsten Vogtt, Dr. Michael Sulc, Dr. Roland Krivanek and Dr. Lucia Krivanekova, for many interesting and helpful discussions. I am also grateful to the IMPRS-CB for giving me the chance to carry out my Ph.D. studies in the program.

Additionally, I would like to acknowledge the working group of Prof. Dr. Enrico Gratton where my first two photon excitation microscopy experiments were carried out, Laboratory for Fluorescence Dynamics, LFD, UCI, USA, especially Dr. Susana Sanchez, Dr. Theodore Hazlett, Dr. Oliver Holub, and Dr. Christian Hellriegel. I would like to thank the IMPRS-CB from the MPI for Molecular Physiology Dortmund for financial support. The help with administrative issues provided by Dr. Jutta Rötter, Christina Hornemann, Waltraud Hoffman-Goody, Dr. Werner Horstmann, Andrea Kreusel and Kirsten Skozdik is duly acknowledged.

I am grateful to Prof. Dr. Detlef Gabel, Dr. Doaa Awad, Tanja Schaffran and Daniel Dărăban, who initiated me in the work with lipids, fluorescence spectroscopy techniques, and cytotoxicity tests during my master studies at the University of Bremen.

I would like to thank all the people who have contributed to the development of my personality both as scientist and human being, to my parents and to all my friends, regardless of their professional interests and geographic coordinates.

List of Abbreviations

Aβ	amyloid beta peptide
AFM	atomic force microscopy
ANF	atrial amyloidosis down
APP	Alzheimer's disease
ATR-FTIR	attenuated total reflection Fourier-transformed spectroscopy
ATTR	senile systemic amyloidosis
Bodipy-FL	4,4-difluoro-5,7-dimethyl-4-bora-3a, 4a-diaza-s-indacene-3-propionic acid
CAA	hereditary cerebral amyloid angiopathy
CAL	medullary carcinoma of the thyroid (calcitonin-related)
CD	circular dichroism
CCD	charge coupled device
CF	carboxyfluorescein
chol	cholesterol
DOPC	1,2-dioleyl-sn-glycero-3-phosphocholine
DOPE	1,2-dioleyl-sn-glycero-3-phosphoethanolamine
DOPG	1,2-dioleyl-sn-glycero-3-[phospho-*rac*-(1-glycerol)]
DPPC	1,2-dipalmitoyl-sn-gylcero-3-phosphatidylcholine
DSC	differential scanning calorimetry
FHSA	Finnish hereditary systemic amyloidosis
FT-IR	Fourier-transformed Infra-Red
GUVs	giant unilamellar vesicles
HEPES	2-[4-(2-hydroxyethyl)-1-piperazinyl]-ethanesulfonic acid
HHP	high hydrostatic pressure
HRA	haemodialysis-related amyloidosis
IAPP	islet amyloid polypeptide
ILA	injection-localized amyloidosis
INS-1E	insulinoma pancreatic islet β-cell line of rat origin, clone derived from the INS-1 rat islet cell line
ITO	Indium-Tin oxide

LUVs	large unilamellar vesicles
MLVs	multilamellar vesicles
MVLs	multivesicular liposomes
NNSA	hereditary non-neuropathic systemic amyloidosis
PD	Parkinson's disease
PE	phosphatidyl ethanol amine
PEG	poly(ethylene glycol)
PC	phosphatidyl choline
PrP	prion protein
PS	phosphatidyl serine
PSA	primary systemic amyloidosis
Rhodamine-DHPE	N-(Lissamine-Rhodamine B sulfonyl)-1,2-dihexadecanoyl-sn-glycero-3-phosphoethanolamine, triethylammonium salt
RIN-m5F	insulinoma pancreatic islet β-cell line, clone derived from the RIN-m rat islet cell line
rpm	revolutions per minute
SAA1	secondary systemic amyloidosis
SANS	small angle neutron scattering
SAXS	small angle X-ray scattering
SUVs	small unilamellar vesicles
t	time
T2DM	type II diabetes mellitus
ThT	thioflavin T
T_m	(gel- to liquid-) phase transition temperature
TTR	transthyretin
ULVs	unilamellar vesicles
UV-VIS	ultraviolet-visible
wt %	weight percentage

Table of contents

Publications:

Weise K., Sellin D., **Radovan D.**, Opitz N., and Winter R (2009) Interaction of human islet amyloid polypeptide (hIAPP) with model raft membranes: the permeabilizing effect of hIAPP oligomers. *submitted*.

Radovan D., Opitz N., and Winter, R (2009) Fluorescence microscopy studies on islet amyloid polypeptide fibrillation at heterogeneous and cellular membrane interfaces and its inhibition by resveratrol. *FEBS Letters 583*, 1439-45.

Mishra R., Sellin D., **Radovan D.**, Gohlke A., and Winter, R. (2009) Inhibiting islet amyloid polypeptide fibril formation by the red wine compound resveratrol. *ChemBioChem 10*, 445–9.

Radovan D., Smirnovas V., and Winter, R. (2008) Effect of pressure on islet amyloid polypeptide aggregation: revealing the polymorphic nature of the fibrillation process. *Biochemistry* 47*,* 6352–60.

Gabel D., Awad D., Schaffran T., **Radovan D**., Dărăban D., Damian L., Winterhalter M., Karlsson G., and Edwards K. (2007) The anionic boron cluster $(B12H11SH)^{2}$- as a means to trigger release of liposome contents. *ChemMedChem 2,* 51-3.

Hiermit versichere ich, dass ich die vorliegende Dissertation selbstständig verfasst und keine anderen als die angegebenen Quellen und Hilfsmittel benutzt sowie die Zitate kenntlich gemacht habe.

Dortmund, 28.08.2009

_____

Diana Radovan

1. Introduction

1.1. Amyloidogenic proteins and peptides

1.1.1. The problem of protein folding *vs.* protein aggregation and associated conformational diseases

Currently, several proteins and peptides are known to be associated with so-called "conformational" or "amyloidogenic" diseases, e.g. type 2 diabetes mellitus (T2DM); Alzheimer's disease, Parkinson's disease, and Creutzfeld-Jakobs disease. In such degenerative human conditions, proteins, which share no common primary structure similarities, form amyloid fibrils-fibrillar polypeptide aggregates (*1*), which are stable against the action of proteases. Unlike ordinary protein fibrils, amyloid fibrils possess a conserved structural motif encompassing β-sheets within a β-cross arrangement. The size of the fibrils is generally in the range of several tens of nanometers (*2, 3*). Around 30 such nonhomologous polypeptide sequences are currently known, but the basic ability to adopt such a structure is a more general feature, also for other polypeptides (*4*). It is considered that amyloid fibrils arise primarly from an intrinsic property of the chiral polypeptide main chain that is often suppressed in nature by unfavourable physicochemical conditions, side-chain arrangements, and evolutionary adaptations (*5, 6*). Generally, amyloid is regarded as a nonnative quaternary structure that forms in response to a defect in the normal folding or clearance pathways (*3*).

It has been speculated that, based on environmental conditions, any protein or peptide could be influenced to form fibrils. Nevertheless, even if this holds true for non-native conditions *in vitro*, conditions under which proteins can form fibrils (e.g. insulin, pH 2, 60º C (*7-9*) , it is to be kept in mind that cellular systems keep a balance between protein synthesis and degradation with the help of molecular chaperones and the proteasome, and the quality-control mechanisms in the cell prevent deposition of partially folded, misfolded, or degraded protein (*10*). When the balance between protein synthesis and protein degradation is disturbed, pathological conditions can appear in the form of amyloid deposits, which can be found in different organs, such as the brain, liver, spleen and pancreas (*11, 12*).

Some of the essential amyloids and associated diseases are listed in Table 1.

Nr.	*Amyloid*	*Protein/polypeptide*	*Associated diseases*
1	APP	Aβ peptides**,** τ protein	Alzheimer's disease
2	PrP^{Sc}	prion protein	spongiform encephalopathies
3	PD	α-synuclein	Parkinson's disease
4	**IAPP**	**islet amyloid polypeptide (amylin)**	**type 2 diabetes mellitus (T2DM)**
5	HRA	β2 –microglobulin	haemodialysis-related amyloidosis
6	PSA	Ig light chains	primary systemic amyloidosis
7	SAA1	serum amyloid A	secondary systemic amyloidosis
8	ATTR	transthyretin	senile systemic amyloidosis
9	HG	huntingtin	Huntington's disease
10	CAA	cystatin C	hereditary cerebral amyloid angiopathy
11	FHSA	gelsolin (71 residues)	Finnish hereditary systemic amyloidosis
12	ILA	insulin	injection-localized amyloidosis
13	CAL	calcitonin	medullary carcinoma of the thyroid
14	ANF	atrial natriuretic factor	atrial amyloidosis
15	NNSA	lysozyme	hereditary non-neuropathic systemic amyloidosis
16	HRA	fibrinogen α-A chain	hereditary renal amyloidosis

Table 1 The major amyloidogenic proteins and their associated diseases. The peptide of interest for this project, IAPP, and T2DM, the associated disease, are marked in bolded characters.

In the up-dated protein folding/misfolding energy landscape, a multitude of possible folding and partially folded intermediate states are suggeseted, as spikes; the native state is shown to be stabilized mainly via intramolecular contacts, corresponding to one energy minimum, thus representing a kinetically stable state, whereas the amyloidogenic form is stabilized through intermolecular contacts, possibly corresponding to several global energy minima, representing thermodynamically stable states in the aggregation funnel (*13*).

The nature of the early and intermediate aggregation species (early oligomers), their polyporphism and corresponding cytotoxicity, as well as the triggering factors of fibril formation *in vivo*, the effects of membranes, as well as strategies against protein aggregation and fibril formation, are currently challenging debate topics in amyloid-related research.

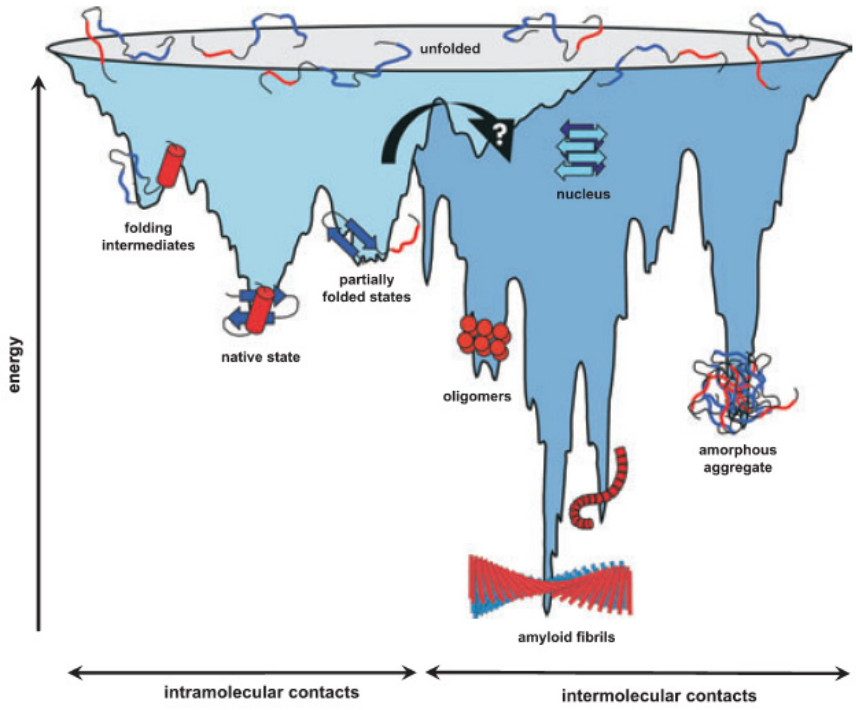

Figure 1 A schematic energy landscape for protein folding and aggregation. The surface shows the multitude of conformations funneling towards the native state via intramolecular contacts, or towards the formation of amyloid fibrils via intermolecular contacts (*13*).

Two basic models are generally used to interpret the sigmoidal profile of fibrillogenesis kinetics, i.e. the nucleation-dependent polymerization (NDP) (*14*) and diffusion-limited aggregation (DLA) (*15*).

In the NDP model, two main steps are involved: the initial slow nucleation or the lag phase and the subsequent fast elongation or growth. Nucleation involves monomer association into a critical oligomeric nucleus, which represents the highest energy state and thus the thermodynamically unfavourable species along the polymerization pathway. Once a critical nucleus size is reached, further elongation via attachment of additional monomers becomes energetically more favourable, resulting in

exponential fibril growth. The nucleus formation or the lag phase is the rate-limiting step, followed by an exponential decrease in monomer concentration, and substantial increase of the reaction rate upon the addition of preformed fibrils (seeding effect) (*16, 17*).

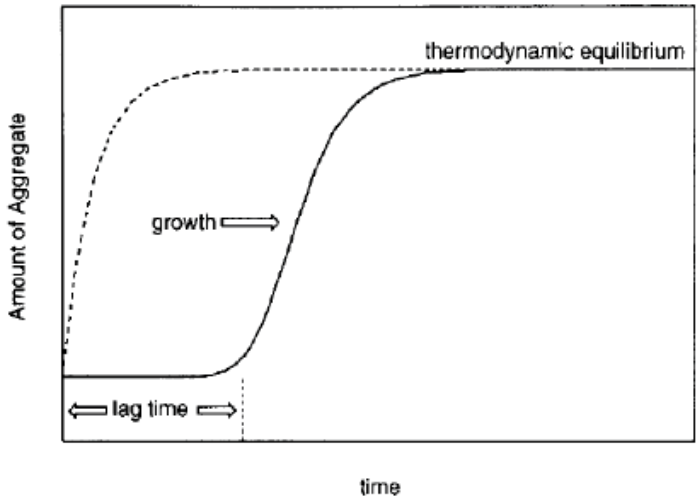

Figure 2 Experimentally observable formation of an aggregate for a nucleation dependent process, above its critical concentration (*17*).

The DLA model was proposed originally for the Aβ peptide (*15*), hypothesizing that peptide monomers spontaneously convert into octamers, which then stack into fibrils, further fibril elongation occurring thereafter through diffusion-limited end-to-end association of the shorter fibrils. The model allows the time-dependence of fibril length, but is not so accurate in postulating the complete conversion of monomers to oligomers. Other mechanisms are known as template assembly (TA), monomer-directed conversion (MDC) and nucleated conformational conversion (NCC) (*18*).

1.1.2. The importance of lipid membranes for amyloid fibril formation

Amyloid isolated from patients has been shown to have a high lipid content (*19, 20*). The multi-step process of protein fibrillization can be modulated by lipid-protein interactions, and experimental data indicate a membrane influence on both the amyloid fibril assembly and on the toxicity of pre-fibrillar aggregates. The process can be termed "membrane-mediated protein fibrillization" (*21*). Amyloid proteins and peptides have been also shown to possess the ability to

interact with lipids *in vitro* (*22, 23*). The structural transformation of the polypeptide chain into a partially folding conformation upon interaction with lipid membranes may lead to an increase in the local concentration of a protein upon membrane binding, followed by aggregation-favouring orientation of the bound protein and variation in the depth of bilayer penetration, thus affecting the nucleation propensity of the membrane associated protein.

Disease	Protein or peptide determinant	Membrane system
Parkinson's disease, Lewy body variant of Alzeihmer's disease, multiple system atrophy	α-synuclein	PA/PG, PG/PC, PS/PC, PG/PE vesicles, planar PC/PS bilayers, PC, PA, PS, PI vesicles, brain membrane fractions, synaptosomal membranes
Alzheimer's disease	Aβ peptide	Total membrane lipid bilayers, PC/PG vesicles, PC/ganglioside vesicles, PA, PS, PI, PIP, PIP2, CL, PC, PE, SM, Chol, DG, gangliosides, sonicated lipid suspensions
T2DM	islet amyloid polypeptide	PG/PC vesicles, rat insulinoma tumour cells
Alzheimer's disease	tau	PS vesicles
spongiform encephalopathies	prion protein	PG, PC, PG/Chol/SM vesicles
familial polyneuropathy, systemic amyloidosis	transthyretin	PC/PS, PG/PS vesicles
systemic amyloidosis	lysozyme	PC/PS, PG/PS vesicles
thyroid carcinoma	calcitonin	PC/Chol, PC/PS, PC/ganglioside vesicles

Table 2 *In vitro* studies regarding interactions of membrane with amyloidogenic proteins and peptides which might be relevant for fibril formation *in vivo* (*21*).

One hypothesis suggests that the toxicity of lipid-induced pre-fibrillar aggregates might have presented a very strong negative selection pressure in the evolution of amino acid sequences (*24*). Amyloid formation has been reported to induce membrane permeabilization resulting from

alterations in the bilayer structure and/or uptake of lipids into the forming fiber (*25*). Another hypothesis regarding the bioactivity of amyloid structures, called the channel hypothesis, relates this bioactivity with the perforation of biological lipid membranes through pore structures containing the amyloid species (*26*). However, whether the interaction between amyloidogenic proteins/peptides and membranes occurs mainly through a barrel-stave or a carpet, detergent-like mechanism, is still a largely debated topic, far from being entirely understood, as no unitary view exists so far regarding a universally valid mechanism. An overview of *in vitro* studies regarding the involvement of membranes in fibril formation by amyloidogenic proteins and peptides is illustrated in Table 2.

Interestingly, the comparison of different types of human amyloidoses showed a conserved lipid pattern consisting mainly of hydrophobic lipids, such as cholesterol, and small amounts of more polar lipids, such as phosphatidylcholine (PC) and phosphatidylethanolamine (PE) (*19*). Raft lipids have been found in several types of amyloidoses (*20*). Moreover, amyloid deposits are enriched in lyso-PC, free fatty acids, and ceramides (CEs), which normally do not occur in biological membranes, but rather accumulate specifically in tissue degradation processes and necrosis (*19*). Although such degrading processes manifest only small effects on the main membrane lipids, such as sphingomyelin (SM) and cholesterol, it is reasonable to assume that, due to the CE and lyso-PC content, that they might represent an additional factor involved in the clinical deposition of amyloid.

It has become apparent in recent years that amyloid fibril formation is strongly promoted at hydrophobic interfaces (*27*), affecting both the rate and the extent of unfolding and aggregation. Proteins adsorbed onto different lipid surfaces have been reported to show faster unfolding kinetics than those in the bulk and the β-sheet content and growth kinetics differed at the interface compared to the bulk (*28*). It is reasonable to assume that lipid bilayers provide a generic environment where protein molecules adopt conformations and orientations promoting their assembly into protofibrillar and fibrillar structures. Furthermore, cellular membranes are thought to be the direct target mediating amyloid-induced cell death (*25*).

1.1.3. Islet Amyloid Polypeptide (IAPP) and type II diabetes (T2DM)

Islet amyloid polypeptide (IAPP) or amylin is the main component of human islet amyloid deposits found *post-mortem* in 95% patients suffering of T2DM; it is a 37 amino-acid residue pancreatic hormone synthesized in the form of proIAPP and processed in secretary granules along with insulin, stimulating glycogen breakdown in skeletal muscle and liver, acting as insulin antagonist under normal conditions. Additionally, IAPP is involved in the regulation of satiety with respect to food intake, and in maintenance processes of bone, renal proximal tubular and islet β-cells (*29-34*). Under pathological conditions, it represents the cytotoxic constituent of amyloid deposits found in the islets of Langerhans in 95% cases of patients with non-insulin-dependent T2DM (*35, 36*). Extracellular accumulation of this peptide results in damage to insulin-producting β-cell membranes and cell death (*37*). The amino-acid sequence of IAPP is highly conserved between species, with a few variations, only, mostly occurring in the 20-29 region, which displays marked species divergence (*38*).

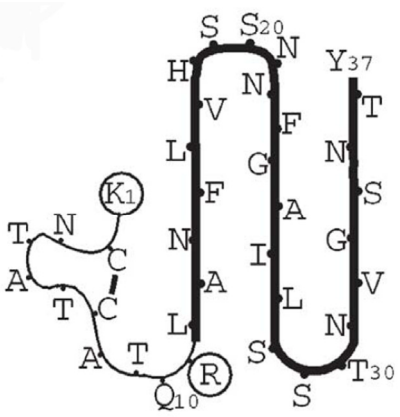

Figure 3 β-serpentine model fold for human IAPP (*39*). The model has three β-strands. Charged residues are circled. The first 11 residues, which contain a disulfide-bonded loop that would be incompatible with extending the serpentine on this side, are shown by a thin line. Accordingly, the first 11 residues are not considered to be part of the serpentine core.

The first stages of IAPP amyloid formation *in vivo* remain so far largely unclear. Autopsy studies of human pancreas have indicated that the deposition of islet amyloid is always an extracellular event, while studies on human islet transplanted into nude mice (*40*) and in islet of human IAPP transgenic mice (*41*) have indicated that the early stages of islet amyloid formation may take place intracellularly. One hypothesis is that the intracellular aggregates of proIAPP act as

a nucleus to which mature IAPP can associate, leading to increased extracellular amyloid deposition (*42*).

1.1.3.1. The fibrillation of IAPP *vs.* IAPP fragments

It has been suggested that the initial stages of IAPP fibril formation are driven by the increase in the level of solvent exposure of hydrophobic patches (*43*) and that the IAPP aggregation process has two distinct phases, a lateral growth of oligomers and a longitudinal growth into mature fibrils (*43-46*).

The structural changes behind the fibrillation process are still poorly understood, however. Since the three-dimensional structure of IAPP is not yet exactly known, experimental studies on fragments of this peptide can provide further insights into the mechanism of aggregation. Several studies indicate that amino acid residues 20-29 make up the main amyloidogenic region (*47*), with a particular emphasis on the penta- and hexapeptide sequences IAPP 23-27 (FGAIL) and IAPP 22-27 (NFGAIL), respectively, as minimal peptide sequences required for aggregation (*48*). IAPP has not only one but several amyloidogenic cores that are interacting to form an organized aggregate structure and hydrophobic interactions may drive the initial stage of the aggregation process. According to the literature, aggregation of the C-terminal domain of IAPP (amino acid residues 20-29 and 30-37) (*49*) is thought to be most likely driven by hydrophobic interactions (*50*).

Experimental studies, showing aggregation into ordered fibrillar structures of fragments 8-20 and 8-37 (*47, 50*), have been reported as well. Within these larger sequences, fragments IAPP 15-19 (FLHVS) (see also Appendix, figure A) and IAPP 14-18 (NFVHL) and the possible importance of aromatic residues (and thus π-π interactions) for amyloid fibril formation were also discussed (*48, 51*), while the N-terminal region of residues 1-19 is considered essential for the interaction with membranes (*52-54*).

Region 1-13, however, has been reported not to form fibrils, while IAPP 8-20 was found capabable of self-assembly *in vitro* (*49*). To complement these studies, we decided to investigate the aggregation of C-terminally amidated synthetic human IAPP 1-19 N-amidated and human IAPP 1-29, both containing a disulfide bridge between Cys 2 and Cys 7, in comparison with the full-length peptide. The C-terminal amidation is essential for a more realistic comparison with the

physiologically active peptide hormone, in which this modification seems to play an essential role in its hormonal function *in vivo* (*34*).

1.1.3.2. The effect of membranes on IAPP fibril formation

There is clear evidence that IAPP-lipid interactions might play an important role in the pathogenesis of T2DM, by accelerating the formation of amyloid fibrils and toxic oligomers and triggering the permeabilization of lipid membranes (*37, 55-57*). It was suggested that these two are separate processes, i.e., membrane disruption can occur independent of amyloid formation (*58*). There are recent indications that the fibrillogenic property of membrane-bound IAPP is largely determined by the chemical nature of membrane lipids. Polar and electrostatic interactions can be stabilized through head groups of the phospholipid, whereas hydrophobic interactions can occur in the lipid chain region. For instance, it has been demonstrated that IAPP aggregation is enhanced in the presence of membranes containing anionic lipids such as phosphatidylglycerol (PG) or phosphatidylserine (PS), and a mechanism of interaction has been proposed (*25, 26, 35, 37, 52, 53, 56, 59, 60*).

In the presence of vesicles composed of zwitterionic (PC) and anionic (PG) phospholipids mixtures (see also Appendix, Figure B), IAPP aggregation was demonstrated to exhibit a sigmoidal profile, with an initial lag phase of relatively slow fiber nucleation and a rapid elongation phase, during which the remainder of the soluble peptide is converted into fibers (*37*). It has been suggested that IAPP inserts into lipid mono- and bilayers via the positively charged N-terminus as a monomer *in vitro*, possibly representing an essential first step required to induce IAPP-induced membrane damage in type II diabetes *in vivo* (*53*). At a surface charge corresponding to 70% mol PG, the rate of fibrillogenesis is maximal, and the rate of fiber formation is limited by the self-assembly of peptide at the lipid-water interface. CD and fluorescence spectroscopy studies have revealed also that negatively charged PS vesicles induce significant acceleration of formation of IAPP aggregates (*60*).

An opposite effect on the kinetics and extent of IAPP aggregation has been only recently shown for membranes including cholesterol (*61*). However, information on the interaction of IAPP with heterogeneous membranes such as lipid raft containing membranes is missing until now, even though there is evidence that raft lipids may be common components of human extracellular

amyloid fibrils (*19*). Moreover, the fibril formation and membrane interaction of amyloid beta (Aβ), another amyloidogenic peptide, which is known to be associated with Alzheimer′s disease, has already been shown to be modulated by cholesterol (*62-65*). Additionally, it was suggested that lipid raft domains, which are enriched in cholesterol and sphingolipids, initiate and promote the pathophysiology of Alzheimer′s disease by serving as a platform for generation, aggregation, or degradation of Aβ (*66, 67*). Since IAPP and Aβ display an amino-acid similarity in their presumably ordered region and a secondary structure similarity in their fibrillar states (*68*), it is tempting to speculate that lipid rafts could also be involved in the pathogenesis of IAPP.

1.1.3.3. IAPP cytotoxicity - mechanism and inhibition

Although it is not clear how IAPP forms amyloid deposits, the mechanism underlying its toxicity is assumed to include as first step the interaction of IAPP with the membranes of the producing islet pancreatic β-cells.

Studies have suggested that, at cytotoxic concentrations, amylin forms voltage-dependent, relatively non-selective, ion-permeable channels in planar phospholipid bilayer membranes, and that the formation of the channel is highly dependent on lipid membrane composition, ionic strength and membrane potential (*26*). One view is that protofibrillar IAPP permeabilizes synthetic vesicles by a pore-like mechanism (*26*). The formation of IAPP amyloid pore is temporally correlated to the formation of early IAPP oligomers and its dispappearance to the appearance of amyloid fibrils. The pore theory would correlate to the pathogenicity of the amyloid pores that were hypothesized to play a key role in Alzheimer's disease and Parkinson's disease (*69*). Nonetheless, studies on the nature of IAPP cytotoxic species and strategies of its inhibition are not conclusive, and no unitary view exists so far. However, it is generally believed that the prefibrillar oligomeric (protofibrillar) IAPP is cytotoxic, thus the "intermediate-sized toxic amyloid particles" (*56*), and not the mature fibrils (*70*). Therefore, the understanding of the nature of the cytotoxic species involved in amyloid formation in T2DM and the mechanism of such toxic effects are obviously of interest, and require further investigations.

Additionally, preventing IAPP amyloid fibril formation is a rational approach in the direction of drug discovery for T2DM. It has been difficult to rationally design drugs due to the lack of structural information about the prefibrillar and fibrillar states of IAPP and of

amyloidogenic peptides in general. Despite the limited knowledge about the structure of the amyloid fibrils screening of inhibitors, in particular, small-molecule inhibitors, might prove promising. Many small molecules are capable of crossing the blood–brain barrier, being stable in biological fluids and avoiding (retarding) the immunological response, respectively. Amyloid fibrils share overall basic features at a molecular level, like cross β-sheet-rich hydrogen-bonded fibrils. Hence, corresponding studies on other amyloids, e.g. Aβ and τ, the Alzheimer peptides, might help us explore strategies for inhibition of IAPP amyloid formation. Based on this assumption it has been recently shown that rhodanine-based small-molecule inhibitors, which are active against τ-fibril formation (*71*) are also effective against IAPP amyloid fibril formation (*72*). Heparin-induced τ-filament assembly can also be inhibited by different classes of compounds like phenothiazines, porphyrins and polyphenols, and, interestingly, these compounds also inhibited Aβ (1–40) fibril formation (*73*). In another approach, based on peptide inhibitors, small fragments of the peptide have been methylated to prevent IAPP fibril formation, but crossing of the lipid membrane by these peptides remains a challenge. A group of compounds, called polyphenols, with more than one aromatic phenolic rings has emerged as inhibitors of Aβ, α-synuclein, and prion amyloids (*74*). In a recent study, a polyphenol, (-)-epigallochatechin gallate (EGCG), has been shown to divert aggregation-prone proteins like A β and α-synuclein into an off-pathway, and thus to prevent fibril formation (*75, 76*). Another phenolic compound from grapes, resveratrol, has been shown to be effective against Aβ (25–35) aggregation (*77*), leading to a reduction in secretion and cellular levels of Aβ (*78*). In fact, IAPP shares amino acid sequence similarity with Aβ in the presumably ordered region and shows a similar secondary structure in the fibrillar state (*68*).

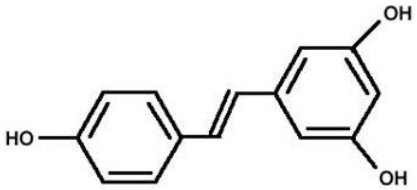

Figure 4 The structure of the red wine compound resveratrol (trans-3,5,4'-trihydroxystilbene).

Thus, we were interested in investigating the potential inhibitory effect of resveratrol (trans-3, 5, 4'-trihydroxystilbene, Figure 4), the afore-mentioned polyphenol found in significant amounts (130–220 μM) in red wine, on IAPP fibril formation.

1.2. Biological and model lipid membranes

1.2.1 Lipids in biological membranes-general considerations

Biological membranes function as the origin of most vital functions within living cells (*79*). Lipids are a fundamental part of all cellular membranes; most membranes containing around 40% lipids, the internal mithocondrial membrane around 20% lipids, and the myelinic membranes even up to 70% lipids. Genomic results indicate that more than 30% of the genome codes for proteins embedded in membranes (*80*). However, in the post-genomic area, biological membranes still represent molecular assemblies of extreme complexity, whose structure and function cannot be determined from the genome alone. Although they have been so far studied within disciplines such as physiology, pharmacology, molecular biology, and nutritional sciences, the progress in the fundamental understanding of biological membranes has not been so far as impressive as compared to the one achieved in protein and DNA-related studies (*80*).

The simple "fluid mosaic" model of cell membranes (*81*) has been recently re-evaluated by the postulation of the existence of the so-called "lipid rafts", of rather small dimensions, in the low nanometer range, defined as membrane microdomains, encountered in cell membranes which are rich in cholesterol and glycosphingolipids (*82*). Such raft domains could be essential for many different types of signalling processes, e.g. in endocytic events (*83*), intracellular trafficking (*84*), Ras-protein signalling (*85*) etc. The observation that the raft composition depends heavily on the method used to obtain it suggests that rafts are highly dynamic moving targets (*86*). The role of lipid compositional complexity has been acknowledged by the raft hypothesis; however, the physical basis behind membrane lateral organisation in biological systems, including the potential correlations with various membrane functions, still remains obscure (*87*). In this context, lipid-protein interactions are of considerable interest as a molecular basis for the structure of biological membranes.

Due to the different lipid compositions of the two opposing leaflets of the bilayer, the plasma membrane is asymmetrical. This may play a key role in keeping certain membrane proteins in the appropriate conformation. All membrane proteins are associated with the lipid bilayer in a highly asymmetrical fashion, a feature crucial to their function (*88*). Lipid-protein interactions

appear to be essential for a wide variety of cellular processes, such as signal transduction, intracellular transport, enzyme catalysis, energy conversion in the cell, antimicrobial defence, and control of membrane fusion (*21*). Lipid bilayers can affect protein structure and dynamics via both specific and non-specific interactions. The membrane can exert its control through various parameters, such as its phase state, bilayer curvature and elasticity, surface charge, degree of hydration, the chemical nature of the lipids, the extent of acyl chain unsaturation, conformation and dynamics of lipid head-groups and acyl chains, and protein-lipid selectivity based on the hydrophobic matching at the protein-lipid interface (*89-91*).

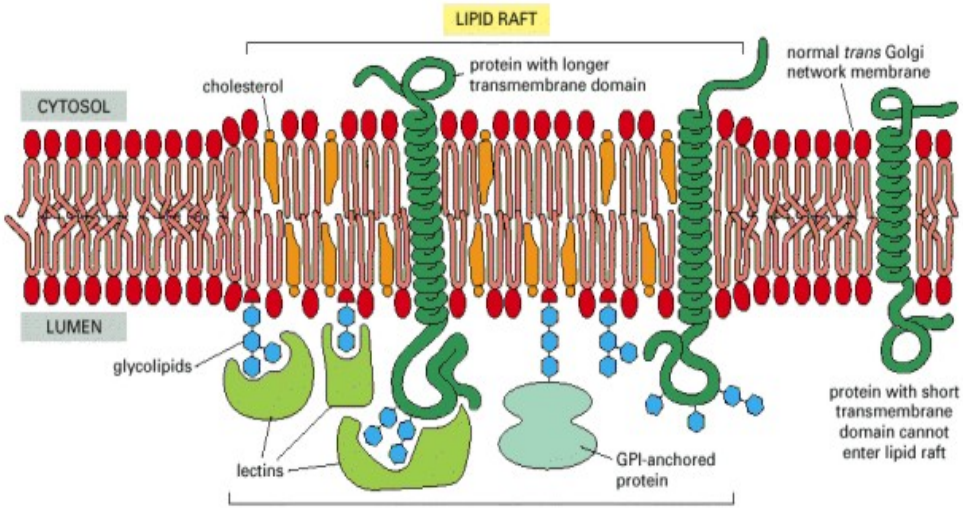

Figure 5 The heterogeneous structure of biological membranes, consisting of variable disordered and ordered lipid domains ("rafts") and embedded peptides and proteins.

1.2.2. Model lipid membranes

Artificial membranes can be used as model biomembranes. Model lipid membranes can be either planar (mono- and bilayers) or spherical (liposomes).

Liposomes can be most easily defined as microscopic spheres consisting of one or more lipid bilayers (usually phospholipids) arranged concentrically around a central aqueous core. They were first described over 35 years ago (*92*) and their potential as *models for biological membranes* and systems for drug delivery has soon been recognized (*93*).

As model closed membrane systems they have proven useful in studying functional roles of lipids, providing the tool to study lipid mobility, lipid phase behaviour and membrane

permeability. Being prepared from natural components, they are bio-absorbable, non-toxic, and non-immunogenic, which made them suitable as *drug carriers*. Based on the preparation methods, liposomes of various degrees of lamellarity and size can be produced, as follows: MLVs (multilamellar vesicles, 10 nm- 5 μm), ULVs (unilamellar vesicles), SUVs (small unilamellar vesicles, 25-90 nm), LUVs (large unilamellar vesicles >100 nm), GUVs (giant unilamellar vesicles, 5-100 μm) (*92*).

Liposome solutions can be used to explore physical properties of membranes (lateral structure and dynamics) by a broad range of experimental procedures, e.g. SAXS, SANS, DSC, NMR, FT-IR spectroscopy, fluorescence spectroscopy, fluorescence microscopy etc. During the last decade, several fluorescence microscopy techniques have been used to study the lateral structure of membranes using GUVs (see also chapter 2.3.2) as model system (*87*).

1.2.3. Classes of lipid molecules

There are three main classes of lipid molecules in the plasma membrane: phospholipids, sphingolipids and sterols, which will be briefly and thus non-exhaustively discussed here.

Phospholipids mainly consist of phosphatidyl cholines (PCs), phophatidylethanolamines (PEs) and phosphatidylserines (PSs). PC, also known as lecithin, constitutes the most encountered lipid class in biological membranes. Such molecules are amphipathic, containing a glycerol bridge which links a pair of hydrophobic acyl chains with the hydrophilic polar head-group (see Figure 4 for details). Unfavourable interactions between the bulk aqueous phase and the long hydrocarbon fatty acid chains are completely eliminated when the sheets fold on themselves to form closed sealed vesicles. PC presents a pronounced tendency to form bilayers sheets rather than micellar structures, unlike other amphipathic molecules (detergents, lysolecithin). This is due to the overall tubular shape provided by the double acid fatty chain, thus making the molecules more suitable for aggregation in planar sheets compared with detergents with a polar head and single chain (*92*). PCs can be derived from both natural and synthetic sources. Natural sources are egg yolk, soya bean, bovine heart and spinal cord. They represent the major phospholipid component of many cell membranes, they are chemically inert and posses an overall neutral charge; hence, they are used as principal phospholipid in liposomes for a wide range of applications. Lecithin from natural sources

is in fact a mixture of PCs, each with chains of different length and varying degrees of unsaturation (see Figure 6), which significantly affect the fluidity of the membrane. The main gel-to-fluid transition temperature (T_m) increases with the degree of saturation and the number of carbon atoms (chain length).

Sphingolipids (Figure 7) are based on ceramide and have either a phosphocholine head group (sphingomyelin) or one of a range of carbohydrate structures (glycosphingolipids). They display a highly asymmetrical distribution, being present in all animal cell plasma membranes in the outer membrane leaflet; their sugar groups being exposed on the outer surface of the cell. Sphingolipids contain long, largely saturated acyl chains, which leads to a tight packing and a much higher melting temperature than normally encountered for phospholipids.

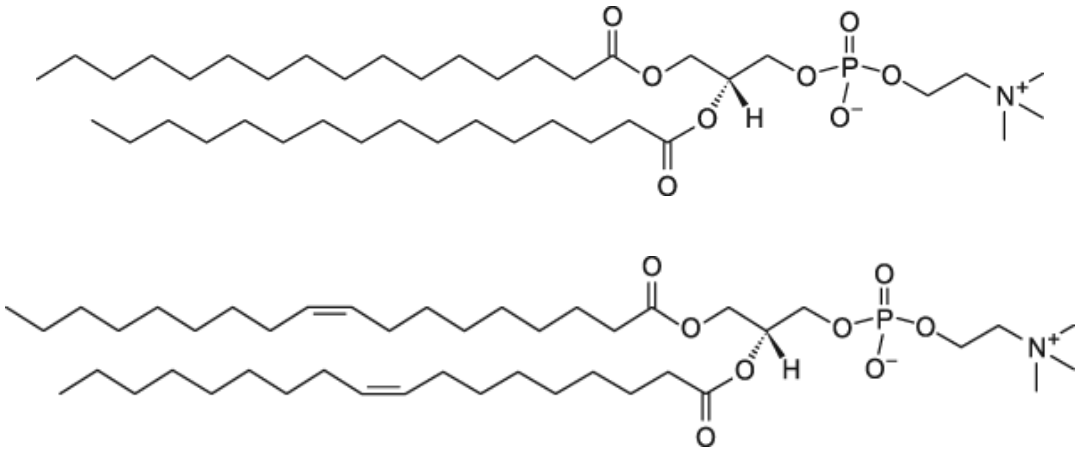

Figure 6 Structures of DPPC (top) and DOPC (bottom).

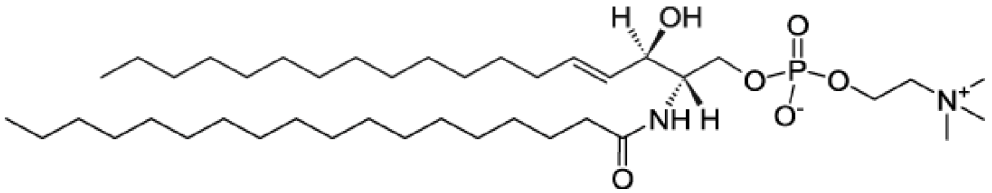

Figure 7 Structure of the predominant species present in brain SM.

Cholesterol (Figure 8), the main form of sterols found in vertebrates, can considerably influence membrane fluidity. Cholesterol by itself does not form bilayers structures, but it can be incorporated into phospholipid membranes at very high concentrations, up to 1:1 or even 2:1 molar

ratios of cholesterol to PC. In natural membranes, the molar ratio varies depending on the anatomical and cellular location (*92*). Being an amphipathic molecule, cholesterol inserts into the membrane with its hydroxyl group oriented towards the aqueous surface, and the aliphatic chain aligned parallel to the acyl chains in the centre of the bilayers.

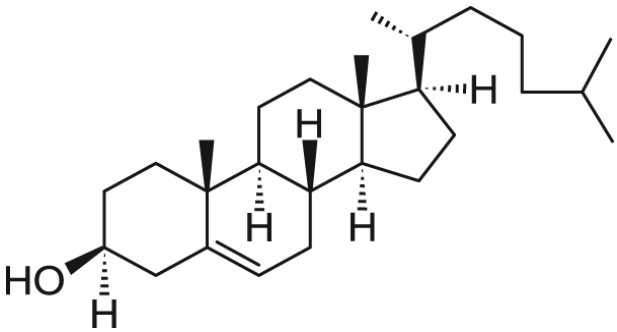

Figure 8 Structure of cholesterol, the predominant sterol in vertebrates.

1.2.4. Lipid phases and microdomains

Phase behaviour determines liposomal properties such as permeability, fusion, and protein binding. At different temperatures, PC membranes exist in different phases, and transitions from one phase to the other can be detected by physical techniques, e.g. microcalorimetry or FT-IR spectroscopy, as the temperature is increased (or decreased) (*94*). The *phase transition temperature* is the temperature at which the membrane passes from a tightly ordered "gel" or "solid" phase ($L_{\beta'}$), to a liquid-crystal fluid-like phase (L_{α}), as illustrated in figure 4. It is also referred to as T_m or main transition temperature and it depends on the hydrocarbon chain length and the degree of saturation. The solid phase is not thought to be of physiological relevance (*95, 96*). At low temperatures, fatty acids form all-*trans* straight chains. As the temperature increases, they tend to adopt *gauche* conformations; this tends to expand the area occupied by the chains, and thus the membrane, while the overall length of the hydrocarbon chains is reduced, therefore the bilayers thickness as well. The transition from the gel phase to the liquid - crystalline phase does not occur in a single step for pure PCs, but involves two transitions; a *pre-transition* takes place a few degrees below the *main transition*, e.g. for DPPC 16:0 the T_m is 41 ºC and the *pre-transition* occurs at 38 ºC, and changes in head-group orientation are believed to occur at that temperature. In

the temperature range between the two transitions, the membrane adopts a ruffled appearance, whereby it is transformed from a planar to an undulating surface with a long, regular periodicity (*92*). At increased temperatures the freedom of movement of individual molecules increases.

Experimentally detectable regions of different compositions and states are termed "phases" in the macroscopic range, whereas on the micro- and nanoscopic scale they are better described as "domains" (i.e. in cell biology) (*82*). Particularly, the presence of cholesterol in a system can change the phase behaviour drastically. At low concentrations, it does not prefer one of the lipid phases to the other. However, at higher concentrations (≥ 25%) cholesterol induces chain order in the liquid phase and breaks the crystallinity of the solid phase. This results in the formation of a new phase: the liquid-ordered phase, which is a liquid with respect to the translational degrees of freedom (lateral diffusion), but rigid with respect to the acyl chain order (*97*). For lipid/cholesterol mixtures, the gel phase is denoted by s_o, "s" standing for solid in two dimensions and "o" for ordered chains; the liquid-crystalline phase is known as l_d, "l" representing the two-dimensional liquid and "d" the disordered chains; the liquid - ordered phase is denoted by l_o (Figure 7). The l_o manifests highly increased mechanical strength over the l_d phase (*98*), the van der Waals interactions for the ordered chains in the lipid molecule being stronger in the latter case. This property, combined with the increased bilayer thickness, drastically reduces membrane permeability (*99*).

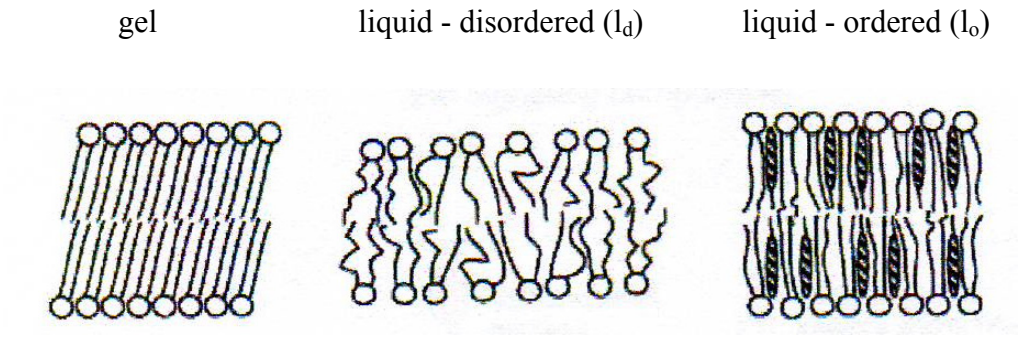

Figure 7 Membrane phases of the lipids of the plasma membranes. The gel phase melts above T_m to form a fluid phase (liquid-disordered (l_d), or "liquid-crystalline"). The presence of cholesterol (hatched ovals) forms an intermediate phase between gel and l_d, termed liquid-ordered (l_o).

Studies carried out on bilayers containing different cholesterol concentrations, indicated that the l_o and l_d states could be relevant to the question of biologically relevant lipid

microdomains. The cholesterol-rich l_o and cholesterol-poor l_d phases coexist within a single bilayer. Generally, lipids that contain exclusively saturated acyl chains promote the formation of the l_o phase because of their capacity to pack more readily against cholesterol. This feature is more dominant in sphingolipids due to their ability to form intermolecular hydrogen bonds (*100, 101*). The affinity of cholesterol varies significantly with the polar headgroup and backbone structure of the lipid molecule, generally decreasing in the order SM>PS>PC>PE. This more favourable interaction between SMs compared to PC would seem to favour the formation of segregated cholesterol-depleted l_d and cholesterol-enriched l_o domains in bilayers composed of SM/PC/Chol, and thus provide support for the lipid raft hypothesis (*102-104*). A bilayer composed of SM is 4.6 nm thick; hence, rafts should protrude from the non-raft background by ~ 1 nm. For PCs, the affinity of cholesterol decreases markedly with an increase in the degree of unsaturation of the lipid chains, thus making the affinity of cholesterol higher for e.g. DPPC (16:0, T_m = 41 ºC) than for DOPC (16:1, T_m = -20 ºC).

Micron-scale coexisting liquid domains can be observed in vesicle membranes *in vitro* with at least three components: a high T_m lipid (saturated), a low T_m lipid (unsaturated), and cholesterol, respectively, over a wide range of compositions and temperatures below a miscibility transition temperature T_{mix}. Diagrams of various lipid systems present different miscibility transition temperatures, i.e. shifts in transition temperatures, e.g. to higher temperatures in membranes containing saturated SM lipids compared to saturated PC lipids of comparable chain length, and to lower temperatures when the low T_m lipid component has a higher chain melting temperature, respectively. Membranes with higher T_m lipids and cholesterol contain more l_o phase and have a high T_{mix}, while membranes with lower T_m lipids contain more l_d phase and have a low T_{mix}. For many ternary lipid systems, 1:1:1 mixtures lie close to the steeply varying edge of the miscibility phase boundary (*102-104*). A useful system for biophysical investigations is the intensively studies model raft mixture DOPC: DPPC: cholesterol. DPPC and DOPC share the same phospholipid headgroup, thus allowing focusing on the role of the hydrocarbon tails. Additionally, experiments suggest that saturated PC (like DPPC) and SM lipids behave similarly in mixtures with DOPC. Although POPC is more biologically relevant than DOPC, its asymmetry could make interpretation of results more difficult. Moreover, immiscible liquid phases were observed in

vesicles over a wide range of lipid compositions when DOPC was used. It is thus tempting to speculate that results for the DOPC/DPPC/cholesterol system are applicable as biologically relevant mixtures.

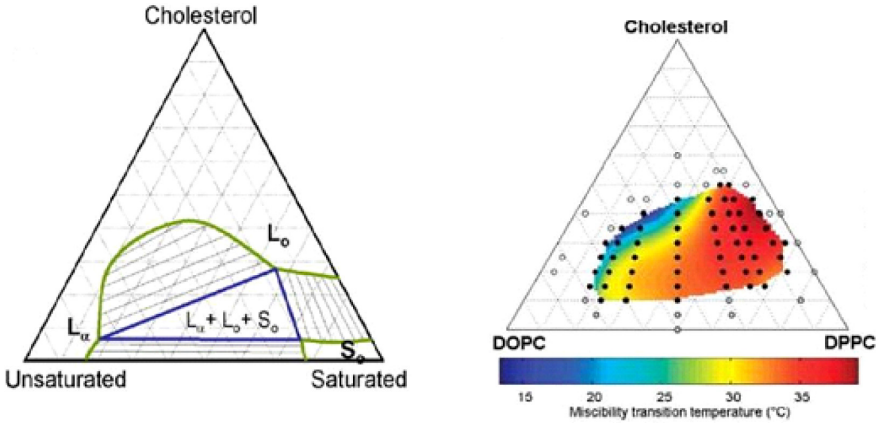

Figure 9 Typical phase diagram for a model raft system, composed of a high T_m lipid, a low T_m lipid and cholesterol, respectively (left), and the miscibility phase boundaries of the ternary lipid mixture DOPC: DPPC: cholesterol (right); (•) compositions where a miscibility transition is observed, (◦) only one liquid phase is present down to 10 °C, (coloured surface) extrapolated fit of measured T_{mix} values (*102*).

The graphical representation of the coexistence of phases is called phase diagram The phase diagram for a typical raft system and the membrane immiscibility region for DOPC: DPPC: cholesterol are illustrated in figure 9 (*102-104*).

1.3. Cellular models for T2DM research

INS-1E cells represent a stable and reliable β-cell model, aspect of major importance for diabetes research. The laboratory of Pierre Maechler established in the early 90s the insulin-secreting line INS-1 from a radiation rat-induced insulinoma (*105*), from which clonal INS-1 E cells were further isolated based on both their insulin content and secretory response to glucose. This represented at that time a compelling research need, since previous rat origin models showed poor resembles to primary cultures, e. g. RINm5F cells do not respond to glucose in the physiological concentration range (*106*), and BRIN-BD11 cells are poorly differentiated, exhibiting low insulin content and only a weak secretory response to glucose (*107*). On the other hand, the new clonal β-cell line INS-1E, derived from the parental INS-1 cells, displays a more suitable insulin content and an adequate proliferation rate (*107*).

1.4. Aim of the project

Our goal is to understand the aggregation of IAPP in the absence and presence of various lipid interfaces, to investigate the nature of the cytotoxic IAPP species and to develop strategies against fibril formation and associated toxicity.

First, we investigated the fibril formation of IAPP and IAPP fragments, with respect to the kinetics of fibril formation, polymorphism, aggregation-prone regions, stability to high hydrostatic pressure, and the role of hydrophobic and electrostatic interactions in the self-association process.

Additionally, we seeked to provide further insight into the mechanism of IAPP aggregation in the presence of membranes, not only the largely studied negatively charged homogenous lipid systems, but in the presence of model raft heterogeneous membranes as well, since extracellular amyloid fibril deposits seem to form by a common cellular mechanism involving lipid rafts. The use of GUVs as model biomembranes combined with advanced fluorescence microscopy techniques is a relatively new approach, which allows the direct microscopic visualization of domains and of their topology on the μm scale, the local and morphological changes on the membranes of different compositions on single vesicles after the addition of peptide, and the corresponding peptide morphologies involved, respectively.

Extending the membrane studies to cellular models, we were interested in determining which species are the most cytotoxic-monomers, early or late oligomers, protofibrillar or fibrillar states. For this purpose, isolating, characterizing and testing different oligomeric species is required, in a time- and concentration-dependent manner. Moreover, developing potential therapeutic strategies against IAPP fibril formation and cytotoxicity *in vivo* is obviously of major concern in the treatment of T2DM. Not only should inhibitors be designed to inhibit IAPP fibril formation in vitro, but they should display low toxicity and efficient inhibition in the presence of cellular membranes as well. A WST-1 assay can be used for such cytotoxicity tests, combined with confocal/two-photon excitation imaging in order to elucidate the interaction mechanism.

Understanding IAPP fibril formation under various conditions, the effect of raft model membranes, along with cytotoxicity-related aspects (major cytotoxic species, inhibitor design) will provide significant contributions in T2DM research for the future.

2. Materials and methods

2.1. Materials and preparation protocol for peptide samples

Chemicals

Bodipy-DHPE	Molecular Probes Invitrogen
$CaCl_2$	Sigma
Chloroform	Fisher Scientific
Cholesterol	Sigma
Congo Red	Sigma
DOPC	Avanti Polar Lipids
DOPG	Avanti Polar Lipids
DMSO	Applichem
DPPC (Dipalmitoylphosphatidylcholine)	Avanti Polar Lipids
DSPC (Distearoylphosphatidylcholine)	Avanti Polar Lipids
Fetal Calf Serum (FCS)	Brunschwig
Glucose	Sigma
HEPES	Applichem
HFIP	Riedel-de-Häen
IAPP	Calbiochem
IAPP 1-19	PSL
IAPP 1-29	PSL
IAPP-(1-37)-K-Bodipy-FL	PSL
INS-1E cells	Gift from Pierre Maechler, Geneva
Inzidur	Ecolab
2-Mercaptoethanol	Applichem
$MgCl_2$	Sigma
Natrium acetate	Sigma
Na_2HPO_4	Sigma
NaH_2PO_4	Sigma
$NaHCO_3$	Applichem

Natrium pyruvate	Applichem
PBS (phosphate buffer saline)	VWR
Penicillin/Streptomycin 10000 IE/10 mg/ml	Applichem
Rhodamine-DHPE	Molecular Probes Invitrogen
RPMI1640+ 2mM L-Glutamine	Gibco
Texas-Red DHPE	Molecular Probes Invitrogen
TFE	Sigma
Trypsin	Gibco
WST-1 reagent	Roche
Disposables	
96-well transparent microtiter plates	BD Falcon
BD-Falcon tubes (15, 50 mL)	BD Falcon
Cell culture flasks	BD Falcon
Cryo-tubes	VWR
Disposable 50-mL syringes	B-Braun Melsungen
Disposable pipette tips (10-200-1000 μL); sterile pipette tips	VWR
Eppendorf cups (0.2-1.5-2.0 mL)	Eppendorf
Pasteur pipettes	VWR
Pipettes (sterile, one-way)	VWR
Sterile filters	Sarstedt
Experimental devices	
AFM microscope	Digital Instruments
Autoclave	ThermoScientific
Balance	ThermoScientific
Centrifuge	ThermoScientific
Confocal Laser Scanning Microscope	BioRad, now Zeiss
Copper conductive tape	SPI Supplies

Digital thermometer	VWR
Fluorescence spectrometer	K2 ISS Urbana-Champaign
Freeze-dryer	Atrbiotech
FTIR spectrometer	Nicolet
Hemacytometer	Brand GmbH
High hydrostatic pressure cell	home-made
Incubator (37 C, 5% CO_2)	ThermoScientific
ITO slides	Sigma
Microtiter-plate (ELISA) reader	Tecan
Light microscope	Olympus
Pipette-boy	Hirschmann Laborgeräte
Pt wires	Advent Research Materials Ltd
Sterile bench	ThermoScientific
Thermostated water bath	VWR
Vacuum pump	VWR

Softwares

Adobe Photoshop	image processing
Corel Draw	image processing
i-control	microtiterplate-reader software
ISS K2 Vinci	fluorescence spectroscopy
GRAMS	ThermoScientific
Laser Sharp 2000, Laser Sharp 2000 Emulation	BioRad, now Zeiss-fluorescence microscopy imaging and data processing
Microsoft Excel	experimental data import and analysis
Origin	experimental data import and analysis
v513, v614	AFM data acquisition and processing

IAPP, IAPP-K-Bodipy-FL, IAPP 1-19 and IAPP 1-29, respectively, were dissolved in HFIP and kept at -20 ºC for at least 24 h, to ensure complete peptide disaggregation. Aliquots were prepared

and the HFIP removed in the freeze-dryer under high vacuum overnight, followed by rehydration in aqueous medium (water, buffer or cell culture medium), thus yielding the desired peptide concentrations for the planned experiments.

2.2. Studies on IAPP and IAPP fragments fibril formation in the absence of lipid membranes

High-pressure coupled with Fourier-transform Infrared (FT-IR) spectroscopic studies and atomic force microscopy (AFM) measurements were carried out to reveal the changes in IAPP, IAPP 1-19 and IAPP 1-29 aggregate and fibril formation under pressure-perturbation. These results could lead to a better understanding of the aggregation pathways and the possible amyloidogenic states of IAPP and may hence contribute to a better understanding of the pathogenesis of T2DM. Moreover, the results obtained may prove useful for the identification and molecular characterization of toxic intermediate states that may be used as targets for parallel searching of compounds that can interfere with their formation.

2.2.1. FT-IR spectroscopy

IR spectroscopy has become a standard method to investigate lipid model membranes, peptides and proteins (*108-110*). The method allows the identification of the structure of the measured molecules, and their interactions with the surroundings, depending on frequencies, widths, intensities, shapes and splitting of the IR absorption bands. In studies of proteins and peptides, FT-IR spectroscopy is useful in identifying secondary structure elements (*111-115*). The amide I' band (between 1600 and 1700 cm^{-1}) is mainly associated with the carbonyl stretching vibration of the amide groups, which is directly related to the backbone conformation and hydrogen bonding pattern of the protein/peptide (*116-121*).

The FTIR spectra of IAPP, IAPP 1-19, and IAPP 1-29, respectively, were recorded continuously for 24 h, every 5min, on a Nicolet 5700 FT-IR spectrometer equipped with a liquid nitrogen cooled MCT (HgCdTe) detector, using a cell with CaF_2 transmission windows separated by 50 μm Teflon spacers. The temperature in the cell was controlled through an external water-circuit, with a precision of 0.1 °C. For scanning the samples before and after pressure treatment, we used 50 mM NaH_2PO_4 (with 1 % residual TFE in D_2O for IAPP) at pD 7.4 and a peptide concentration of 0.1 % w/w and additionally 0.5 wt% for the fragments. For each spectrum, 256 interferograms of 2 cm^{-1} resolution were co-added. The sample chamber was continuously purged

with dry air. From the spectrum of each sample, a corresponding buffer spectrum was subtracted. The plots of the progress of α-helix–to–β-sheet refolding upon aggregation were calculated as $(I - I_\alpha)/(I_\beta - I_\alpha)$, where I_α is the spectral intensity at ~ 1620 cm^{-1} of the first spectrum, I_β is the intensity after complete aggregation, and I is a transient intensity at this wavenumber. All the spectra were baseline-corrected and normalized for the amide I' band area. All data processing was performed with the GRAMS software (Thermo Scientific).

2.2.2. Atomic force microscopy (AFM)

TappingMode™ (Figure 6) AFM operates by scanning a tip attached to the end of an oscillating cantilever across the sample surface.

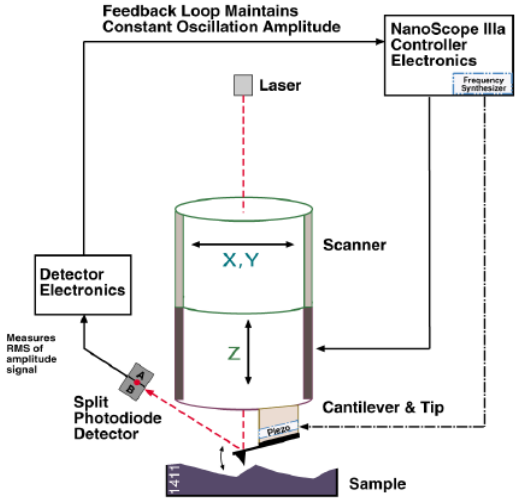

Figure 10 Scheme of AFM measurements using the TappingMode™ (adapted from the scanning probe microscopy training notebook, Digital Instruments).

The cantilever is oscillated at or near its resonance frequency with amplitude ranging typically from 20 nm to 100 nm. The tip lightly "taps" on the sample surface during scanning, contacting the surface at the bottom of its swing. The feedback loop keeps the oscillation amplitude constant by maintaining a constant root mean square of the oscillation signal acquired by the split photodiode detector. The vertical position (z) of the scanner at each (x, y) data point in order to maintain a constant "set - point" amplitude is stored by the computer to form the topographic image of the sample surface. By maintaining the oscillation amplitude fixed, a

constant tip-sample interaction is preserved during imaging. The operation can take place in either ambient or liquid environment. When imaging in air, the typical amplitude of the oscillation allows the tip to contact the surface through the adsorbed fluid layer without getting stuck (Scanning probe microscopy training notebook, Digital Instruments).

For the AFM measurements, samples were diluted with deionised water to yield a final concentration of 1 μM. 20 μL were applied onto freshly cleaved muscovite mica and allowed to dry. Data were acquired in the tapping mode on a Multi Mode TM SPM AFM microscope equipped with a Nanoscope IIIa Controller from Digital Instruments. As AFM probes, Silicon SPM Sensors "NCHR" (force constant, 42 N/m; length, 125 mm; resonance frequency, 300 kHz) from Nanosensors were used (*115, 122-124*). All images were recorded on a MultiMode scanning probe microscope equipped with a Nanoscope IIIa Controller from Digital Instruments (Santa Barbara, California, USA). The microscope was coupled to an AS-12 E-scanner (13-μm) or J-scanner (100-μm) and an Extender Electronics Module EX-II (Santa Barbara, California, USA), which allows for acquisition of phase images. Typical AFM-probes were Aluminium-coated NCHR silicon SPM sensors (force constant = 42 N/m; length = 125 μm; resonance frequency ~250-330 kHz; nominal tip radius of curvature ≤ 5 nm) from Nanosensors, Nanoworld or Budgetsensors, with the optical block and base placed atop a commercially available active, piezo-actuated vibration-damping desk from Halcyonics (Göttingen, Germany). All measurements were carried out in air using TappingMode™.

2.2.3. High hydrostatic pressure (HHP) as tool in protein studies

High hydrostatic pressure (HHP) has been widely used as a tool in understanding protein folding (*8, 111, 112, 122, 125-129*). High pressure tends to destabilize proteins due the fact that the protein-solvent system in the unfolded state occupies a smaller volume than the system in the native state. In a similar way, pressure leads to the dissociation of oligomeric proteins. These effects are caused by a combination of factors. The presence of cavities within the folded proteins, or at interfaces of oligomers, favours the unfolding or dissociation of these structures. The dissociation of electrostatic interactions also leads to a marked reduction in the overall volume caused by electrorestrictive effects of the water molecules around the unpaired charged residues. In a similar way, solvation of polar groups results in a decrease in volume. These effects compensate

for the increase in volume as the crystalline-like state of the protein interior is disrupted, exposed to solvent and hydrated upon unfolding. Finally, hydrophobic interactions have been shown to weaken upon pressurization (*130*).

It is to be noted that using the pressure variable *vs.* the temperature variable in studies of protein folding and stability can offer a great number of advantages (*125, 126*). Pressure affects only the volume of the system in focus, while temperature denaturation involves changes in both the volume and the thermal energy of the system. Also, temperature-induced aggregation generally results in an irreversible aggregation process, which may be explained by less disfavoured hydrophobic interactions at higher temperatures. On the contrary, denaturation by high pressure is generally a reversible process. Furthermore, high pressure treatment can lead to dissociation of aggregated structures and may result in formation of monomers and natively folded structures (*9, 115, 127, 128*). Moreover, the measurement of the activation volume for pressure-induced kinetic folding or unfolding reactions is one of the few methods yielding structural information regarding the transition states. Hence, in addition to co-solvent and temperature perturbation, pressure dependent studies can shed new light on alternative folding/aggregation pathways and their intermediate states.

To the best of our knowledge, there are no reports regarding the effects of HHP on IAPP so far. Due to the fact that high hydrostatic pressure acts to disfavour hydrophobic and electrostatic interactions that cause protein aggregation, this parameter can be used as efficient tool to reveal new important information on the nucleation and growth processes of the peptide.

In order to investigate the stability of IAPP towards high pressure, either fresh peptide or pre-formed fibrils were subjected to pressures up to 3.5 kbar and the changes were measured by tapping-mode AFM and FT-IR spectroscopy to yield information about the transformation process and the structures evolving at various levels of complexity.

Incubation under pressure was carried out in a pressure cell equipped with sapphire optical windows, similar to that originally described by Paladini and Weber (*131*). The temperature of the pressure cell was controlled by means of a jacket connected to a circulating bath. Pressure was increased stepwise in increments of 150 bar until 3 and 3.5 kbar, respectively. The windows of the pressure cell were flushed with nitrogen at low temperatures to prevent water condensation.

2.3. Studies on IAPP fibril formation at lipid interfaces by fluorescence microscopy

2.3.1. Advanced fluorescence microscopy techniques

Optical microscopy is based on macroscopic properties such as phase gradients, light absorption, and birefringence. In contrast, fluorescence microscopy has the ability of monitoring the distribution of single molecular species based solely on the properties of fluorescence emission. By using intracellular components labeled with specific fluorophores, this method offers the possibility to detect their precise location as well as their associated diffusion coefficients, transport characteristics, and interactions with other biomolecules. While other methods used to study lipids, e.g., fluorescence spectroscopy, DSC, IR, NMR, X-ray diffraction, can provide mean parameters on the basis of data collected from bulk solutions of many liposomes (or cells), nowadays microscopy techniques, such as advanced fluorescence microscopy, can provide information about lateral lipid organisation at the level of single vesicles (or cells) (*87*).

Improvements in conventional fluorescence microscopy

A conventional fluorescence microscope differs from a standard microscope by the light source (xenon or mercury lamp), which produces UV-VIS light. The excitation wavelength is selected by an interference filter or a monochromator, and observation of the fluorescence is achieved by eye, photographic film or CCD (charge coupled device) camera (*132*). The depth of field of a conventional fluorescence microscope is 2-3 μm and the maximal resolution is approximately equal to half the wavelength of the radiation used (i.e. 0.2-0.3 μm for visible radiation). For samples thicker than the depth of field, the images are blurred by out-of-focus fluorescence. Corrections using a computer are possible, but other techniques are generally preferred, i.e., *confocal microscopy* or *two-photon excitation microscopy* (*133*).

2.3.1.1. Confocal fluorescence microscopy

The confocal microscope was invented in the mid 1950s, the principle of the method being as follows: a focused spot of light scans the specimen, the fluorescence emitted by the specimen is separated from the incident beam by a dichroic mirror and focused by the objective lens through a pinhole aperture to a photomultiplier (*132*). The major advantage of this technique is that fluorescence from out-of-focus planes above and below the specimen strikes the wall of the

aperture and cannot pass through the pinhole (Figure 11). A laser is often used in confocal fluorescence microscopy, but scanning is achieved by using vibrating mirrors or a rotating disk containing multiple pinholes in a spiral arrangement (Nipkow disk). In laser scanning confocal microscopy, images are stored on a computer and displayed on a monitor.

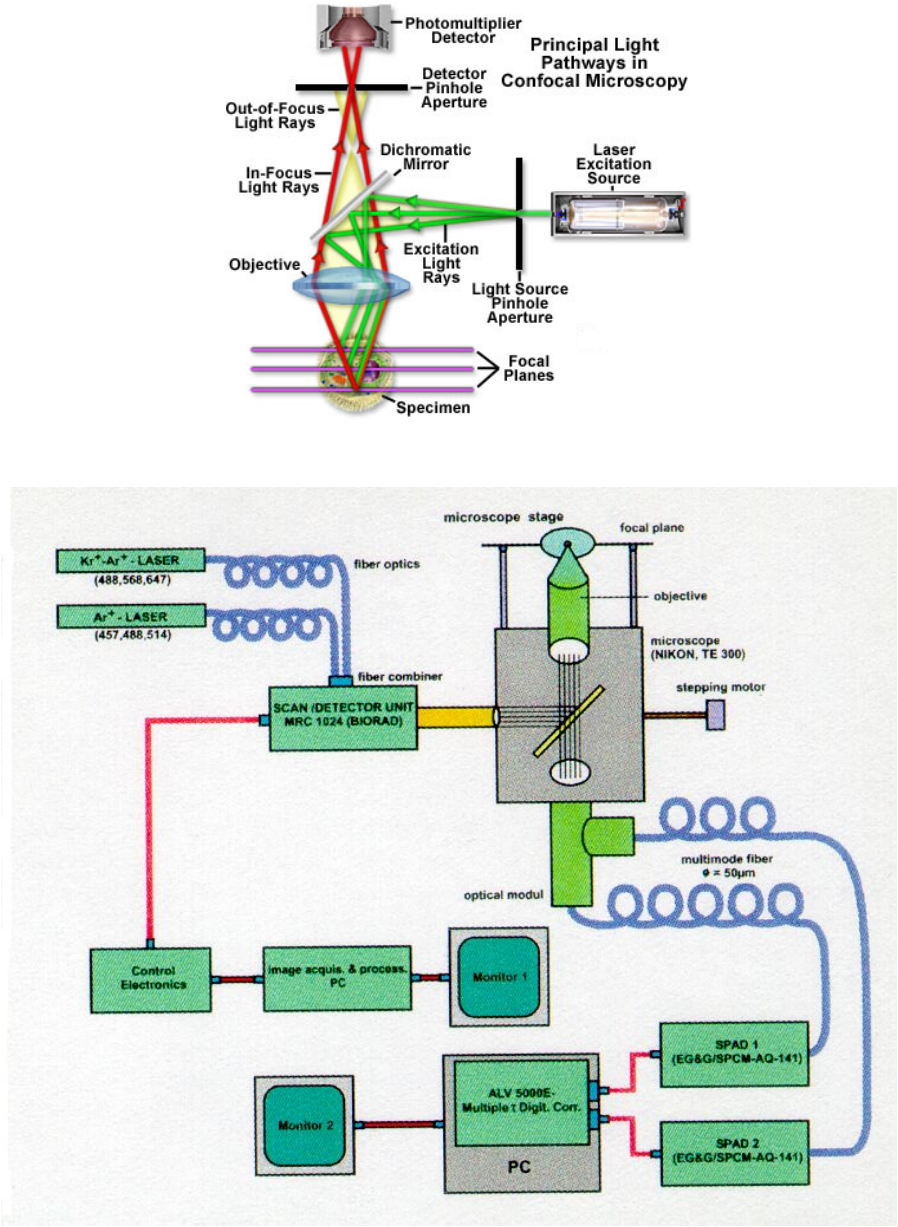

Figure 11 Principle of confocal microscopy (top) and the set-up used in this thesis (bottom).

One of the main features of confocal microscopy is that it can produce optical slices of defined thickness through thick specimens. Using a lens of high numerical aperture, the thickness of confocal sections can reach a theoretical limit of about 0.5 μm. Thus, by moving the specimen up and down, a 3D image can be recorded. However, it should be noted that, because confocal microscopy collects only a fraction of the total fluorescence emitted by a sample, the excitation energy required to image this fluorescence must be higher than in conventional fluorescence microscopy. Therefore, the amount of photobleaching per detected photon is higher. Photobleaching should be minimized by using stable fluorophores and by operating the confocal microscope at low laser power, high detector sensitivity, and maximum objective numerical aperture. Confocal fluorescence microscopy has been widely used in cell biology; single living cells and cellular processes can be studied by this technique, e.g. for visualization of organelles, distribution of electrical potential, pH imaging, calcium imaging, etc. (*134*).

Interesting applications in chemistry have also been reported, for example in studies of colloids, liquid crystals, polymer blends, photodegradation of naturally occurring polymers, dyeing of fibers and measurement of the glass transition temperature. Confocal fluorescence microscopy can be combined with time-domain and frequency-domain techniques to produce lifetime imaging (*132*).

2.3.1.2. Two-photon excitation fluorescence microscopy

In conventional fluorescence spectroscopy, a fluorophore is excited by absorption of one photon whose energy corresponds to the energy difference between the ground and the excited state, respectively. Excitation is also possible by the simultaneous absorption of two photons of lower energy (i.e. of longer wavelength) via a short-lived virtual state (Figure 12). For instance, absorption of two photons in the red can excite a molecule that absorbs in the UV. Two-photon excitation is a non-linear process; the absorption following a quadratic dependence on the intensity of the excitation light.

When a single laser is used, the two photons are of identical wavelength, and the technique is called two-photon excitation fluorescence microscopy (*135*). When the photons are of different wavelengths, the technique is called two-colour excitation fluorescence microscopy. The

probability of two-photon absorption depends on both the spatial and temporal overlap of the incident photons (the photons must arrive within 10^{-18} s). The cross-sections for two-photon absorptions are small, typically 10^{-50} cm^4s $photon^{-1}$ $molecule^{-1}$ for rhodamine B. Consequently, only fluorophores located in a region of very large photon flux can be excited. Mode-locked, high-peak lasers like titanium-sapphire lasers can provide enough intensity for two-photon excitation in microscopy (*132*).

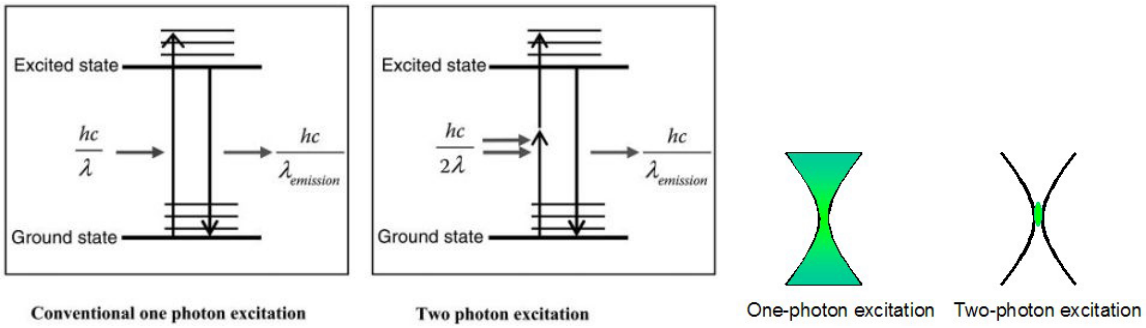

Figure 12 One-photon excitation *vs.* two-photon excitation. The high photon densities required for adsorption (left) are achieved by focusing a high peak power laser light source on a diffraction-limited spot through a high numerical aperture objective. Therefore, in the areas above and below the focal plane, two-photon absorption does not occur (right), because of insufficient photon flux. This phenomenon allows for a sectioning effect (inherent spatial resolution) without the use of emission pinholes as in confocal microscopy.

Because the excitation intensity varies as the square of the distance from the focal plane, the probability of two-photon absorption outside the focal region falls off with the fourth power of the distance along the vertical optical axis. Excitation of fluorophores can occur only at the point of focus. Using an objective with a numerical aperture of 1.25 and an excitation beam at 780 nm, over 80% of total fluorescence intensity is confined to within 1 μm of the focal plane. The excitation volume is of the order of 0.1-1 femtoliter. Compared to conventional fluorometers, this represents a reduction by a factor of 10^{10} of the excitation volume. For a mode locked laser source with an average power p_0, repetition rate f_p, pulse width τ_p, and wavelength λ, focused by an objective with a numerical aperture A, the number of photon pairs absorbed per laser pulse and per chromophore, n_a,is given below:

$$n_a \approx \frac{p_0^2 \delta}{\tau_p f^2{}_p} \left(\frac{\pi A^2}{hc\lambda} \right) \quad (1)$$

where c is the speed of light, h is Plank's constant and δ is the two-photon cross section, typical of the order of 10^{-50} to 10^{-49} cm^4 s photon^{-1} molecule^{-1} (*136*).

Two-photon excitation provides intrinsic 3D resolution in laser scanning fluorescence microscopy. The 3D sectioning effect is comparable to that of confocal microscopy, but it offers two advantages with respect to the latter: because the illumination is concentrated in both time and space, there is *no out-of-focus photobleaching*, and *the excitation beam is not attenuated by out-of-focus absorption*, which results in increased penetration depth of the excitation light.

The advantage of two-colour excitation over two-photon excitation is not an improvement in imaging resolution, but the easier observation of microscopic objects through highly scattering media. In fact, in two-colour excitation, scattering decreases the in-focus fluorescence but only minimally increases the unwanted fluorescence background, in contrast to two-photon excitation.

Two-photon excitation fluorescence microscopy is one of the most promising areas in biological and medical imaging nowadays (*133*).

2.3.1.3. Experimental set-up for fluorescence microscopy studies

Images were recorded by a confocal laser scanning microscope (Biorad MRC 1024, extended for multiphoton excitation, now Zeiss, Germany, figure 13) coupled via a side-port to an inverted microscope (Nikon, Eclipse TE-300 DV, infinity corrected optics) enabling fluorescence excitation in the focal plane of an objective lens (Nikon Plan Fluor 40×, NA 0.6, extra long working distance 3.7 mm, see also figure 13). Fluorescence in the green and red PMT-channels (emission bandpass filters 522 nm/FWHM 35 nm and 580 nm/FWHM 40 nm, respectively) were acquired either sequentially by alternating the excitation with the 488 and 568 nm lines of a Kr-Ar-Laser, or simultaneously by utilizing a Ti-Sap-Laser (Coherent, Mira 900-F, 76 MHz repetition rate, ca. 250 fs pulse width, pumped by a 5 W Verdi) tuned to 820 nm for optimal 2-photon excitation of rhodamine-DHPE. Image acquisition was controlled by the software LaserSharp2000 (formerly Biorad, now Zeiss).

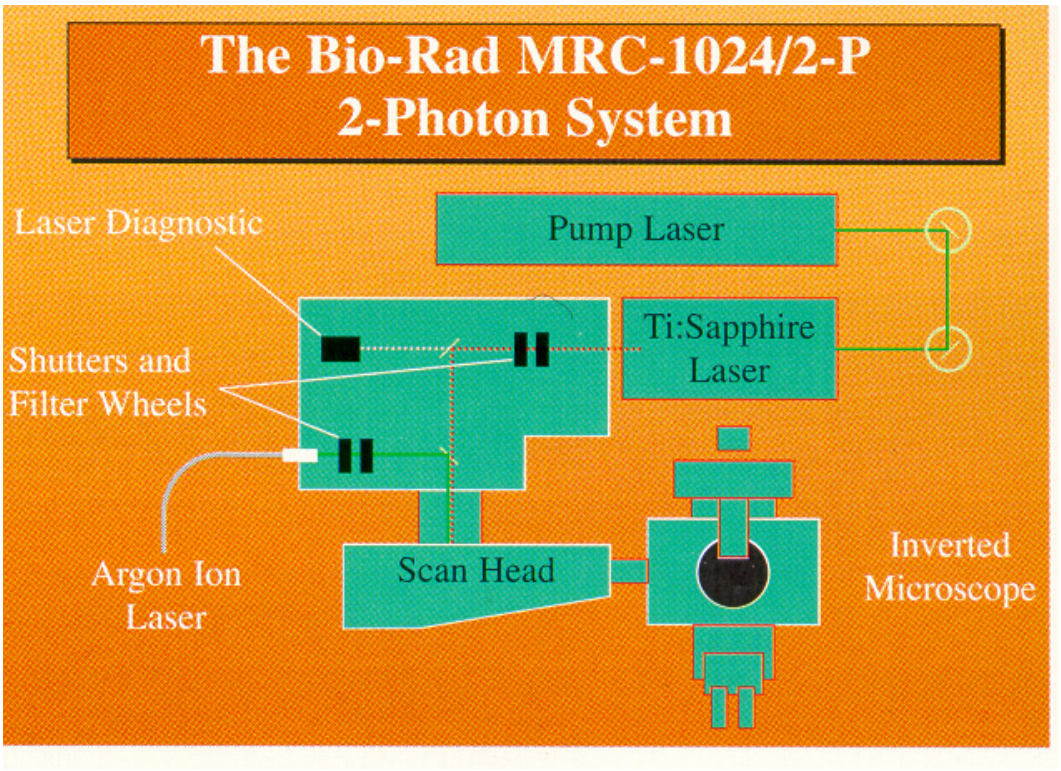

Figure 13 The Bio-Rad 2-photon system extended for confocal excitation.

2.3.2. Giant unilamellar vesicles (GUVs)

2.3.2.1.General aspects about GUVs

The use of giant unilamellar vesicles (GUVs) in biophysics and biochemistry has been increasing over the past 20 years, partially due also to the development of preparation techniques. GUVs are vesicular self-assemblies enclosing an aqueous core, with an average size of 5 to 100 μm, the size range allowing observing them by optical methods as individual macromolecular entitities, and representing the largest form of self-organisation, except for crystalization. Another advantage is that they are geometrically analogue to living cells, due to their size of a few tens of micrometers.

GUVs have been extensively used in recent years as model systems to study, e.g., the lateral structure and mechanical properties of membranes, considering the effect of lipid-lipid, lipid-DNA, lipid-peptide and lipid-protein interactions. Due to the possibility of visualizing single vesicles, the problem of shape and size heterogeneity and the presence of multilamellar vesicles are excluded (*87*).

Due to their similarity to cells, they are used as proto-cell models, to investigate the compartimentation and formation of gradients across the membrane. GUVs can also be used as microreactors; for instance, by the microinjection technique, targeted enzymatic-catalyzed reactions can take place inside the vesicles. GUVs are also applied in medicine and physiology, e.g. to study muscular activity, by building GUVs from muscle tissue membranes, and monitoring the activity of glucose transporters. Also, signal transduction pathways and the influence of toxins could be studied with the aid of GUVs. Native membranes can also built GUVs, e.g. pulmonary surfactants (*137*). Mechanical and elastical properties of membranes using GUVS as model systems have been addressed as well (*138, 139*).

In order to increase the yield and size of GUVs, several preparation methods have been tested over the years, mainly involving either sources of ultra-thin lipid films with minimal mechanical movement, or the fusion of previously formed smaller vesicles. One of the first methods to prepare GUVs was described by Reeves und Dowben in 1969 (*140*). They prepared a thin lipid film from a mixture of chloroform and methanol, which was hydrated after drying and solvent removal wihout any shaking or moving, the result being a very heterogenous dispersion.

As the interest in GUVs increased, further methods and improvements were developed. For instance, the use of Teflon surfaces, the equilibration of lipid films in humidified atmosphere, and the use of spin-coating (*141*) to prepare very thin lipid films can be named as significant examples. Other methods make use of dialysis, freeze-thawing and dehydration-rehydration of small vesicles (*142*).

A by now largely applied method to specifically produce only GUVs is the so-called electroformation method, whereby a dry lipid film is hydrated under an electric field (*143*). The method was since its discovery further optimized to reduce the time required for vesicle formation, and to obtain a more homogenous size range, and improved unilamellarity, by varying either the electroformation conditions (frequency, voltage) or the thickness of the applied lipid film. The method has been used both for planar parallel, as well as for cylindrical chambers, and the electrodes are generally either Pt wires or indium tin oxide (ITO) glass slides. Either steady or alternative current can be used. For a long time, until a novel electroformation protocol using 500 Hz emerged (*137*), electroformation was limited to a ionic strength under 10 mM NaCl, and even a 1 mM Ca^{2+} ions concentration was found to abolish the process of vesicle electroformation completely. Commonly used solvents are chloroform, methanol and diethylether. The lipid concentration to be applied is generally of 0.2 mg/mL, and the distance between the two Pt wired used as electrodes should be 3-5 mm, with a diameter of 0.8 mm. The parameters for the electrical field highly depend on the geometry of the electroformation chamber and must be optimized experimentally. During electroformation, the lipids must be in the fluid phase.

2.3.2.2. Mechanism of GUVs electroformation

The mechanism of GUVs electroformation is still poorly understood, although several effects of the external electric field on lipid swelling and vesicle formation have been suggested, with an increasing degree of speculation, as follows: direct electrostatic interactions between electrode and bilayers, electro-osmotically induced mechanical stresses; redistribution of double layer counter-ions between bilayers, decreased surface, membrane and line tension, electrochemical reactions, injection of charges from electrodes, and reorientation and lateral distribution of lipid molecules, inverse flexoelectric effect (*144*). The diameter of the electroformed GUVs highly depends on the lipid composition, swelling medium, and the external

AC field parameters, which give the amplitude of the electro-osmotic vibration and subsequently the membrane tension of a GUV immediately upon its formation. The predominating mechanism of electroformation is most likely the electro-osmotic periodic movement of the water medium at the water-electrode interface. These vibrations are directed perpendicularly to the electrode surface, where the initial lipid film is deposited. The vibrations pull lipid lamellae off the electrode causing their separation and growth. The vesicles increase in size up to 10-20 μm, this size corresponds to vesicles forming spontaneously from swelling lipid films. At this stage the contact area is increased, and destabilizing due to the AC-field through electroosmotic vibrations takes place. Thus, the neighbour vesicles fuse together into a larger one, become spherical and within a few minutes close their neck and some of them will eventually separate from the electrode (Figure 14).

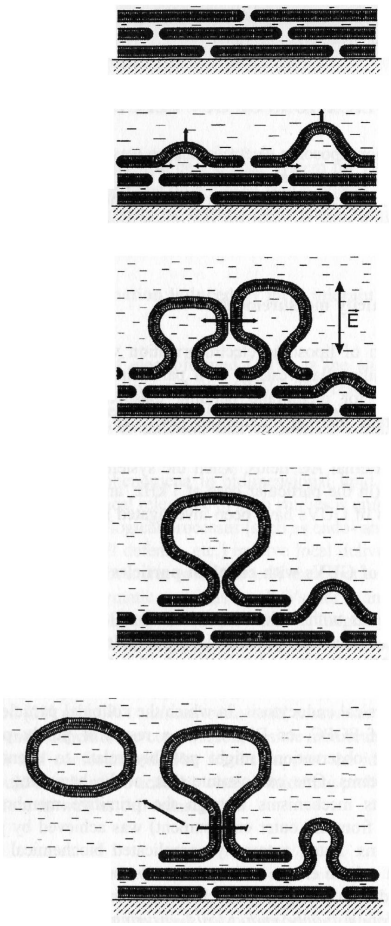

Figure 14 Proposed mechanism of electroformation in aqueous environment (*144*).

2.3.2.3. Electroformation of GUVs on Pt wires

The set-up to grow GUVs using the electroformation method consists of an electroformation chamber and an external AC or DC supply. The AC supply is a low-frequency generator providing a frequency of 0.1-50 Hz and up to 7 V voltage. For electroformation in high ionic strength buffer systems, a higher frequency, i.e. 500 Hz, is an essential parameter in successful GUVs production (*137*).

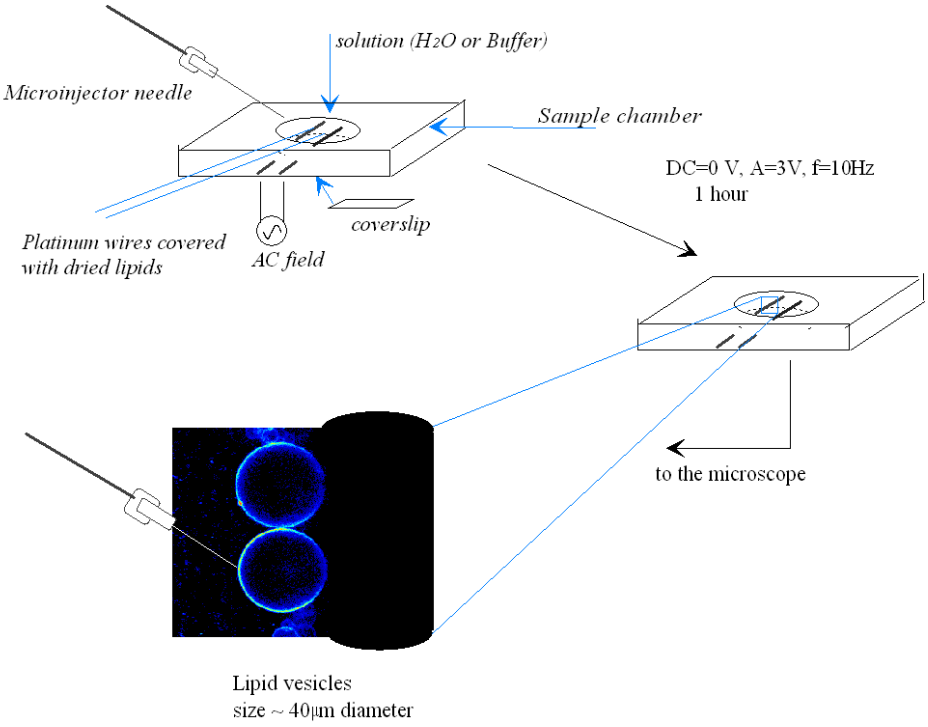

Figure 15 Teflon chamber with two parallel cylindrical Pt wires. The bottom of the chamber was glued to the casing with 0.5 mm glass plates. The top of the chamber was designed to enable the addition of water and peptides into the chamber.

Figure 15 shows a Teflon chamber with two parallel cylindrical Pt wires. The bottom of the chamber was glued to the casing with 0.5 mm glass plates. The top of the chamber remains open to enable adding of Millipore water and peptides.

Thus, GUVs were prepared by electroformation (*143, 145-148*) in a home-made chamber on Pt wires. Individual lipid stocks were prepared at 10 mg/mL and mixed at a 1:2:1 molar ratio (DOPC: DPPC: cholesterol), yielding 200 µL lipid mixture, into which 6 µL of a 1 mM

rhodamine-DHPE (chemical structure illustrated in Figure 16) chloroform stock was added. The sample was further diluted with chloroform and 2 µL of the resulting 0.2 mg/mL lipid mixture were spread on each Pt wire; subsequently, chloroform was removed in a freeze-dryer at high vacuum for 1 h. The chamber was sealed with a cover slip and the lipids were hydrated with 1.5 mL water, pre-warmed at 65 ºC, and electroformation was carried out for 90 min under AC, at 3 V and 10 Hz, at 65 ºC, a temperature at which the lipid mixture is known to be in the l_d phase.

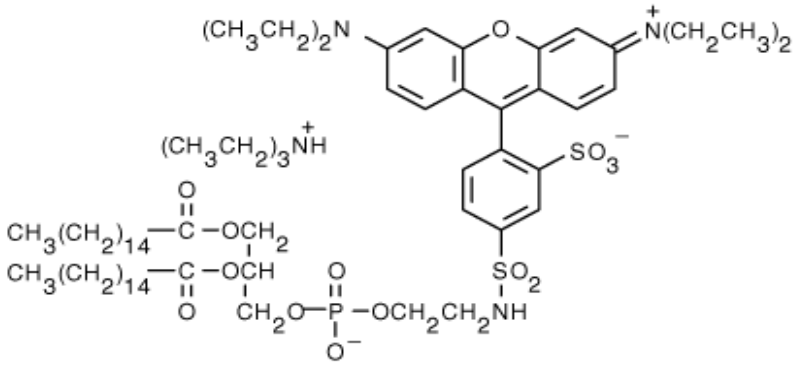

Figure 16 Chemical structure of Lissamine™ rhodamine B 1,2-dihexadecanoyl-sn-glycero-3-phosphoethanolamine, triethylammonium salt (rhodamine DHPE).

After the completion of electroformation, the temperature was slowly reduced at a constant rate of 1 °C/min up to room temperature (25 °C). After choosing a region of interest for imaging of the GUVs (of ~ 30 µm diameter grown on Pt wires), the peptide of interest was added into the chamber and the lipid-peptide interaction was investigated over time via fluorescence microscopy. Rhodamine-DHPE was used to label preferentially the l_d phase.

2.3.2.4. Electroformation of GUVs on ITO slides

In another variant, known as the ITO method (see Figures 17 and 18 for details), the electrodes consist of two plane parallel transparent electrodes – ITO coated glass plates. The dry lipid film is placed on the bottom glass and a silicon spacer separates the two plates and delimits the filling volume. The used chamber was self-made. A 550 µL aqueous volume is required to fill the chamber.

It is important to keep in mind when designing such chambers, that the copper adhesive conductive tape used to close the electrical circuit should not come in contact with the fluid used

for hydration, in order to ensure a homogenous electrical field, and that the electrodes (in this case the ITO glass slides) should be placed in close proximity to each other (several mm). Additionally, ensuring that the lipid is spread homogenously on the electrode surface is desirable (*149*). For this purpose, spin-coating was used (see also Appendix, Figure C), by subjecting 20 µL lipid mixture in $CHCl_3$ spread over the entire ITO surface to 840 rpm for 60 s (4 mg/mL, 1:425 Rhodamine-DHPE: lipid molar ratio). Except for the above mentioned aspects, the electroformation protocol was the same as in the case of the Pt wires.

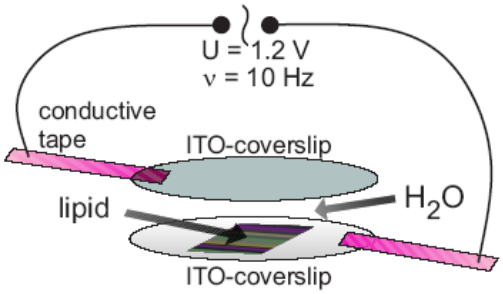

Figure 17 Schematic illustration of the electroformation concept in the case of the ITO method.

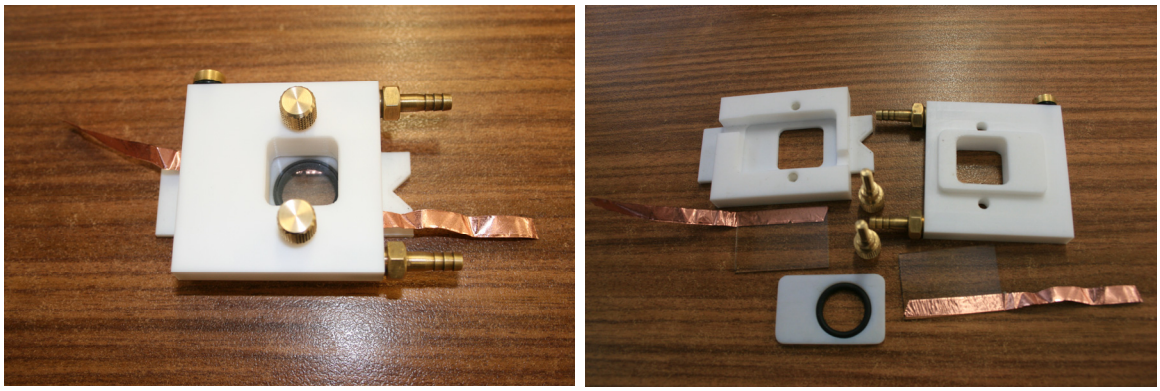

Figure 18 Home-made chamber for electroformation on ITO slides.

2.4. Cytotoxicity tests using the INS-1E cell line as model system

2.4.1. Routine procedure for culturing the INS-1E cells

The cell line employed was INS-1E, insulinoma beta cells from the rat pancreas. The cells were cultured in RPMI 1640 medium (with 2 mM glutamine) supplemented with 5 % foetal calf serum, 10 mM HEPES, pH 7.4, 1 mM sodium pyruvate, 50 µM 2-mercaptoethanol, 100 units/mL penicillin and 0.1 mg/mL streptomycin, at 37 °C, 5 % CO_2, pH 7.4.

RPMI (Roswell Park Memorial Institute) 1640 was established in 1966 byMoore and colleagues based on RPMI 1630. It was originally developed for leukemia cells in monolayer/suspension, and it contains aminoacids, vitamins, serum growth factors, cytokines, being currently used for a large spectrum of cells, including suspension cultures of bone marrow cells, periphereal blood cells, and cells from solid tumors. RPMI 1640 contains the standard recipe of D-glucose and bicarbonate, but sometimes also L-glutamine if required. Like in the case of DMEM (Dulbecco's Modified Eagle Medium), it can also contain HEPES, bicarbonate or reduced bicarbonate and can be used as transport medium (*150*).

Sera are generally used at a 3-25 % ratio in the cell culture media. Nowadays, serum is not always used as supplement in cell culture media, in order to avoid contamination with mycoplasms, viruses and L-shaped bacteria. Serum has no exact composition, can differ from animal to animal, and therefore new lots should be tested prior to being used routine wise. Neither the exact composition of serum, nor the components which are in fact vital for cells are fully known so far. Serum generally contains growth factors, hormones, adhesion molecules, cytokines, amino acids, vitamins, and proteins (50-70 mg/mL). One should distinguish between foetal calf serum (FCS) and newborn calf serum (NCS). FCS is extracted from unborn calves, by butchering the mother cow between the third and the seventh month of pregnancy. PDGF-platelet derived growth factor. NCS is obtained by killing the calf in the first or second week of life, and is known to have a comparatively higher protein content. Currently, there are discussions whether heat-inactivation of serum is indeed required.

The INS-1E cell line was a gift from the group of Dr. Pierre Maechler (Genova University Hospital, Switzerland). The INS-1E cells were cultivated in cell culture flasks, at 37 °C and a 5 %-CO_2-content in the incubator. The cells were passaged once per week under the sterile bench, and a medium exchange was performed twice per week. The old medium was sucked off and the cells were washed with 5 mL diluted PBS, which was again sucked off. 3 mL Trypsin were added to the cells in order to detach them from the bottom surface, and left for incubation for ~ 5 minutes. After the complete solubilization of the cells from the bottom surface, a cell suspension was created by pipetting up-and-down with a sterile 5 mL pipette, until no cell clusters remained (controlled under

a light microscope, 20× air objective, Olympus). Two new cell culture flasks were set for further cultivation by adding 1 mL cell suspension in 25 mL fresh cell culture medium.

Unlike preparing cells for cryoconservation, which has to be done slowly and with optimal cooling rates, defreezing of cells should be carried out as fast as possible. This is justified by the need to discard/dilute toxic cryoconservation products such as DMSO as soon as possible, in order to prevent cellular damage. For this purpose, cryovials containing cells were warmed up in a pre-tempered water bath at 37 °C, until all ice crystals have been dissolved. The content of the cryovials was transferred under the sterile bench into a centrifuge tube, containing already pre-warmed medium. Cells were then centrifuged for 10 minutes at 500 g and 37 °C. The supernatant was dissolved and the cell pellet was resuspendend into 200 µL freshly prepared medium. The cell number was determined as described in chapter 2.4.2 (see also Figure 19) and cells were seeded into new cell culture flasks at the required density (*107, 148, 151*). The cellular adhesion was controlled after 24 h under an optical microscope, prior to further handling.

2.4.2. The WST-1 cell proliferation assay

The WST-1 assay is a colorimetric assay for the quantification of cell proliferation and cell viability, based on the cleavage of the tetrazolium salt WST-1 by mithochondrial dehydrogenases in viable cells (Figure 19). The existence of a high number of viable cells results in an increase in the overall activity of mitochondrial dehydrogenases in the investigated sample, which in turn leads to an increase in the amount of formazan dye formed, thus directly correlating to the number of metabolically active cells in the culture. A strong yellow colour is a first visual indication of increased viability. It is used as a non-radioactive alternative to the [^{3}H]-thymidine incorporation assay (*152*). The cell proliferation reagent WST-1 is a clear, slightly red solution, containing WST-1 and an electron coupling reagent, diluted in phosphate buffered saline, sterile. Quantification of the formazan dye produced by metabolically active cells was realized by using a scanning multi-well spectrophotometer (ELISA reader, Tecan 2000). The absorbance of the dye solution was measured at appropriate wavelengths, i.e. 450 nm with a reference at 620 nm.

In recent years, several different tetrazolium salts like MTT, XTT and MTS have been employed for the measurement of cell proliferation and viability. Some advantages to other tetrazolium salts previously used are, as follows: WST-1 yields water-soluble cleavage products

which can be measured without an additional solubilisation step, it is stable and can be used as a ready-to-use solution and stored at 2-8 °C for several weeks without significant degradation. WST-1 has a wide linear range and shows accelerated colour development compared to other dies. Plates can be read and returned to the incubator several times for further colour development. This technique requires neither washing nor harvesting of cells and the complete assay from the onset of the microculture to data analysis by ELISA reader is performed in the same microplate.

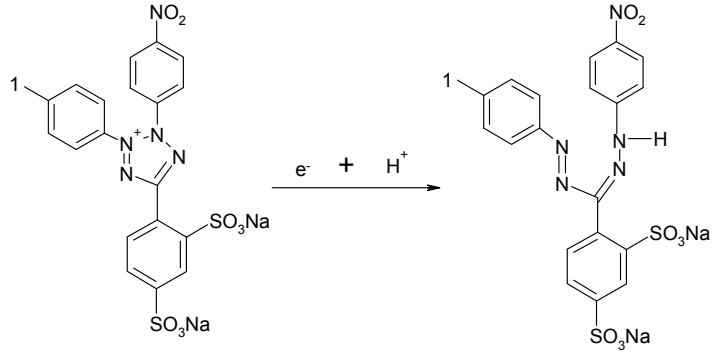

Red Yellow

Figure 19 Cleavage of the tetrazolium salt WST-1 (4-[3-(4-Iodophenyl)-2-(4-nitrophenyl)-2H-5-tetrazolio]-1,3-benzene disulfonate) to formazan; EC = electron coupling reagent; RS= mitochondrial succinate-tetrazolium-reductase system.

For a complete WST-1 assay, the experimental steps were as follows:

Step 1: A cell suspension was prepared as described before. A hemacytometer was used to determine the total number of cells (Figure 20). The hemacytometer was covered with a cover slip and a small amount of cell suspension (~ 16 µL) was uniformly applied between the surface of the cover slip and that of the hemacytomerter with a micropipette. The cells in the 4 big squares (see Figure 20) were counted and the average value was calculated. One big square corresponds to 0.1 µL.

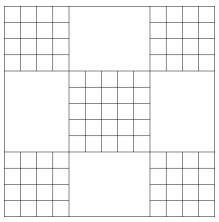

Figure 20 Schematic illustration of a hemacytometer.

This average number was then multiplied with 10^4/mL. The obtained value (e.g. 200 x 10^4) corresponds to 1000 µL. Therefore, the volume corresponding to the desired number of cells to be seeded into each well of the 96-well plate could be calculated, i.e. for 10000 cells/well. The cell suspension was diluted in order to obtain 100µL final volume/well.

A total number of either 36 or 72 wells of 96-well microplates (tissue culture grade, 96 wells, flat bottom) were used for each experiment. Each measurement was carried out in triplicate. The wells corresponding to rows A and H were left empty. The cells were seeded into the remaining wells. Lines 2-12, rows B-D were filled with 100 µL diluted cell suspension. In line 1, rows A and H, only 100 µL medium was pipetted. The cells were incubated at 37 °C and 5% CO_2 for 24 h.

Step 2: The active substance was added into the wells at the desired concentrations. Solutions of IAPP, IAPP and inhibitor, or free inhibitor, were prepared in Eppendorf cups prior to pipetting into the wells, for a total volume of 330 µL, out of which 100 µL was applied in each well (triplicate readings). The old medium was removed under the sterile bench from the wells. Several sterile tissues of corresponding size were placed under the bench and the wells were turned upside down, so that the medium could be adsorbed on the tissues. Further washing of the wells or directly sucking off the medium out of each well is not to be desired, since it would also detach some cells from the well bottom, interfering with the accuracy of the assay. 100 µL of the diluted stocks of active substances were thereupon distributed into the corresponding wells, i.e. rows B to G and lines 2 to 10. In rows A and H, and lines 1 and 12, only 100 µL medium were pipetted. Row 12 corresponded thus to the 100% value, or control value, i.e. with no active substance to affect the survival of the cells. Row 1 served as blank value. The cells were exposed to the potential cytotoxic agents and further incubated at 37 ºC and 5% CO_2 for the respective desired incubation times.

Step 3: The WST-1 cell proliferation reagent was diluted 1:4 with PBS, and subsequently 1:10 with culture medium. 100 µL of this diluted solution was added to each well and allowed to react for 24 h, upon which the absorbance was measured. A control containing 100 µL of the diluted WST-1 (column 1) reagent, only, was measured as blank (applied in the wells which were treated in steps 1 and 2 with cell culture medium, only).

2.4.3. Sample preparation for fluorescence microscopy experiments

Cells were cultured as described in section 2.4.1. The cells were then seeded into 96-well plates at 10000 cells/well, grown for 24 h prior to exposure to the agent to be tested (10 μM IAPP, a mixture of IAPP and resveratrol (1:1 molar ratio), or 10 μM resveratrol, respectively), and then exposed for different incubation times. After this step, the supernatant was replaced with a 5 μM membrane lipid probe (Texas Red-DHPE, 1 mM stock in DMSO) in serum-free medium for 20 min, and afterwards the medium was replaced with PBS buffer, pH 7.4, containing 0.9 mM $CaCl_2$, 0.5 mM $MgCl_2$ and 5 mM glucose, prior to the fluorescence microscopy investigations. IAPP-K-Bodipy-FL was used to allow fluorescence imaging of the fibrils.

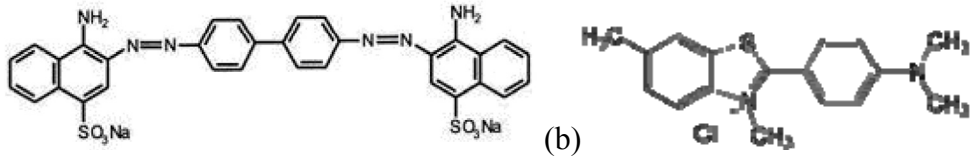

Figure 21 The fluorescent markers used in the illustrated cellular fluorescence imaging studies for amyloid staining: (a) Congo Red and (b) Thioflavine T.

We have also tried to use staining with Congo Red and Thioflavine T (ThT), two amyloid-specific dyes (Figure 21), known to bind essentially only to mature fibrils, but not to monomers or oligomers. However, we encountered that ThT was found to be toxic to INS-1E cells in the concentration range required for quantitative estimation of IAPP fibril formation (several μM). Also Congo Red showed pronounced non-specific binding to the cellular membranes of INS-1E cells. Moreover, we found a pronounced spectroscopic cross-talk between this dye and the cellular membrane marker Bodipy-DHPE, which was used in this approach in combination with Congo Red. As a consequence, we have opted for a different approach, where we simultaneously monitored two fluorescent dyes, with Bodipy being covalently coupled to the IAPP molecule, and either rhodamine-DHPE or Texas Red-DHPE as cellular membrane labels.

2.4.4. Isolation of different IAPP aggregates and their cytotoxicity

An IAPP stock was prepared by dissolving 3 vials of 0.5 mg IAPP each (84% peptide content) in 3 mL HFIP (108 μM IAPP). 100 μL from this stock were lyophilized overnight to yield a 100 μM IAPP solution upon redissolving in 108 μl acetate buffer, supplemented with 50 μM

ThT, for the ThT assay. The rest of the stock solution was liophylized overnight. The liophylized powder was redissolved in 10 mM natrium acetate buffer, pH 5.5, yielding a 100 μM IAPP solution, which was allowed to aggregate in 10 mM Natriumacetate buffer, pH 7.4, at 10 ºC, up to 4 weeks. At different time points, i.e. 0 h, 7 h, 10 h, 25 h, 50 h, 100 h, 150 h, 150 h, 250 h, 3 weeks, 4 weeks, and 5 weeks, respectively, aliquots were removed on ice, frozen in liquid nitrogen and then placed at -80 ºC for preservation, for future investigation by AFM for detection of predominant aggregation species, or for cytotoxicity tests for the determination of the major cytotoxic species. After all species of interest have been isolated, samples were defrosted (originally 1 h on ice) and diluted to either 10 or 20 μM peptide concentration with cell culture medium. A WST-1 assay was performed, as described in chapter 2.4.2., with the exception that in this case blanks corresponded to cell culture medium diluted 1:10 (for 10 μM IAPP final concentration) or 1:5 (for 20 μM IAPP final concentration) with natrium acetate buffer.

Fluorescence spectroscopy measurements were carried out on a K2 multifrequency phase and modulation fluorometer with photon counting mode equipment (ISS, Urbana, IL). A schematic set-up is illustrated in Figure 22.

ThT is a benzothiazole dye (Figures 20b and 23), which displays enhanced fluorescence upon non-covalent binding to mature amyloid fibrils. No intermediate/amorphous aggregate binding was reported. It has two maxima, $\lambda_{1exc\ max}$ = 335 nm, $\lambda_{1emis\ max}$ = 438 nm (425-455 nm), $\lambda_{2exc\ max}$ = 440 nm, $\lambda_{2emis\ max}$ = 482 nm, only the latter one being relevant for fibril binding studies. There are several hypotheses regarding the mechanism by which ThT interacts with amyloid fibrils. Although it is tempting to speculate that ThT may bind between the β-sheets of the fibrils, no experimental proof exists so far to support this statement (*153*); binding probably stabilizes the planar form of the molecule and leads to a 10-500 fold increase in ThT fluorescence intensity (*153*). Some studies suggest that the positive charge of ThT is involved in its micelle formation (above 4 μM) , which then binds to amyloid fibrils (*154*). The emission intensity at 482 nm was recorded upon excitation at 440 nm as a function of time *t*. The data were normalized by dividing the intensity at every point to the intensity recorded for the final aggregates.

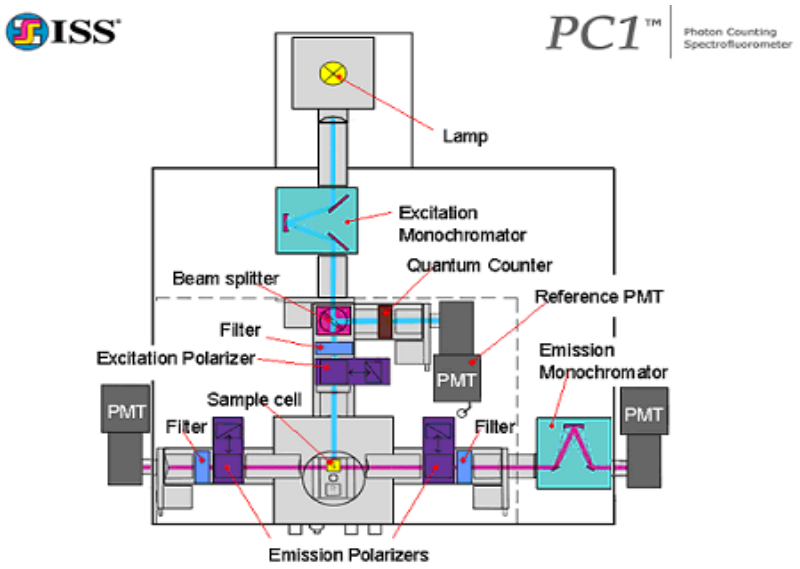

Figure 22 A schematic set-up of the K2 fluorometer A xenon arc lamp acts as source of excitation light. The emitted light is focused with the help of lenses on the entrance slit of the excitation monochromator.; the spectral dispersion in the monochromator occurs in the concave, holographic gratings with 1200 grooves per millimeter. The spectral region ranges from 200-800 nm with $\Delta\lambda$ = 0.25 nm. Both monochromators are equipped with a set of interchangeable slits, of 2, 1, 0.5 mm; the linear dispersion of the monochromator being 8 nm/mm, slits have a bandwidth of 16, 8, and 4 nm. The monochromatic light is then stirred over a mirror, fastened to the corner of a two-way polarizer, directly on the beam splitter provided in the excitation light path, reflecting part of the excitation light to a reference cell, containing a "quantum counter", a rhodamine-B concentrated solution which virtually absorbs all incidents light from 200-600 nm. The intensity can be converted to a signal proportional to the number of incident photons by the use of rhodamine B as reference, since excitation spectra are distorted primarily by the wavelength dependence of the intensity of the exciting light. The quantum yield and emission maximum (~630 nm) are essentially independent of excitation wavelength from 220-600 nm.

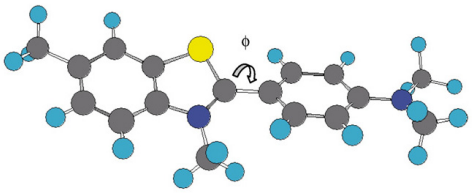

Figure 23 Model for the structure of ThT, showing the rotation of the rings. The amyloid state is thought to stabilize the planar structure of the molecule, thus causing intense fluorescence (*153*).

3. Results and discussion

3.1. Studies on IAPP and IAPP fragments fibril formation in the absence of lipid membranes

Here we report on high-pressure work with IAPP, including IAPP fragments, aim to reveal new information about their aggregation pathways and the structural properties and polymorphic nature of their aggregate and/or fibril structures. The conceptual framework for using such pressure-axis experiments is as follows: The interior of proteins is largely composed of rather efficiently packed residues (with a void volume on the order of less than 0.5%), more likely hydrophobic than those at the surface. High hydrostatic pressure induces conformational fluctuations due to a decrease in the strength of hydrophobic and electrostatic interactions, finally leading to partial pressure-induced unfolding through transfer of water molecules into the protein interior, gradually filling cavities and leading to the dissociation of close hydrophobic contacts and subsequent swelling of the hydrophobic protein interior (*129, 130*).

3.1.1. High pressure studies on full-length IAPP

In order to investigate the stability of IAPP towards high pressure, either fresh peptide or pre-formed IAPP fibrils were subjected to pressures up to 3.5 kbar (350 MPa) and the changes were monitored by FT-IR spectroscopy and AFM to yield information about the transformation process and the structures evolving at various levels of complexity. The protein solutions were prepared from stock solutions in a water buffer with 1 % residual TFE. Such condition has been shown to give raise to or to synchronize the formation of pre-assembled β-sheet structures which are rich in fibrils and protofibrils (*155*). FT-IR spectroscopy was used to monitor the secondary conformational changes, a common tool used for monitoring α-helix to β-sheet transitions and to disentangle between different β-sheet structures that accompany the aggregation process, and which can also be used for pressure-dependent spectroscopic studies (*113, 114, 127, 129*).

Figure 24 shows FT-IR spectra of various IAPP samples: freshly dissolved IAPP and IAPP aggregated for 3 days at ambient pressure and at 3.5 kbar, respectively. All spectra were taken at room temperature (25 °C). The FT-IR spectrum of the freshly prepared IAPP sample (5 min after preparation) at a concentration as high as 0.1 wt% exhibits an intense IR band appearing at ~ 1622 cm^{-1}, which is due to intermolecular parallel β-sheet structures, and a pronounced peak at 1673 cm^{-1}, which is due to turns and residual trifluoracetic acid (TFA) in the sample. Such IR pattern is

indicative of the aggregated state of IAPP according to data of other amyloidogenic proteins, like insulin (*115, 156*). After the incubation period of 3 days at ambient temperature and pressure, the IR spectrum shows similar features, with a broadening and a small shift of the amide I' band to slightly smaller wavenumbers (~ 1618 cm^{-1}), however.

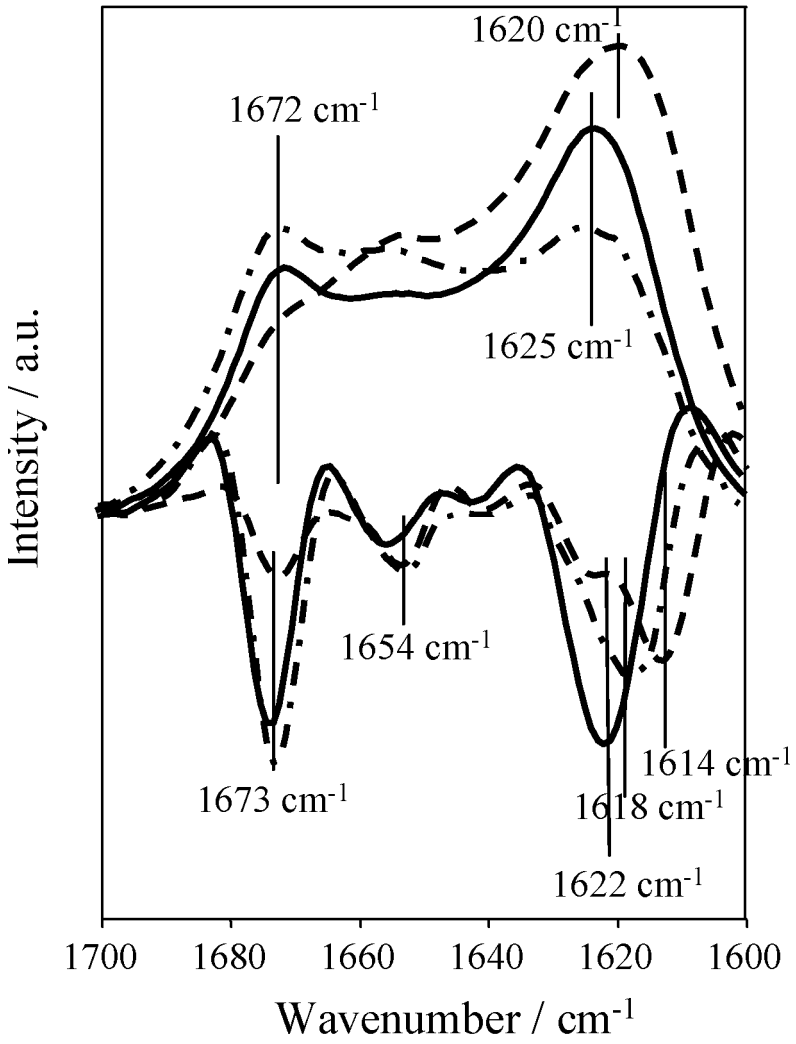

Figure 24 FT-IR spectra (at the top) of IAPP: (-) freshly dissolved sample at time zero, (- · - · -) after 3 d of aggregation in 50 mM NaH_2PO_4 (pD 7.4) at ambient pressure, (- - -) after 3 d at 3.5 kbar. All data were taken at T = 25 °C. At the bottom of the figure, also the second derivative spectra are shown, which allow a more accurate determination of peak positions.

Very likely, a distribution of different sizes and shapes of IAPP aggregate is found initially, and the overall size of the structures evolving increases with increasing IAPP concentration. After

the incubation period it seems that the □-strands are realigning from a non-perfectly packed initial state to more ordered structures with stronger H-bonding, leading to the observed shift of the amide I' band to 1618 cm^{-1} accompanied by an increase of the β-turn content. When IAPP was aggregated under pressure (3.5 kbar), the aggregate band shifts to significantly smaller wavenumbers (~ 1614 cm^{-1}), indicating that the pressure treatment leads to the formation of a different aggregate structure with stronger intermolecular H-bonding between □-sheet strands, or to a larger population of these species.

In order to reveal the different morphological structures formed, AFM measurements were carried out for this IAPP concentration under the same preparation conditions (Figure 25). Most of the aggregate structures seen in the sample that was not subjected to HHP are short (< 1 □m) fibrils with an average of 5 - 15 nm diameters as determined from the AFM height profile. Such rather short fibrillar structures probably appear due to a comparably fast nucleation process at this rather high protein concentration. The pressure treated sample (Figure 25, panel B) still contains fibrils, but also a significant amount of smaller oligomeric particles (of 0.5 - 1.5 nm size).

Taking the FT-IR spectroscopic and AFM results together, we may conclude that the sample subjected to high pressure treatment displays less fibrillar β-sheet structures and a larger population of smaller amorphous aggregates with a different H-bonding pattern. To support these conclusions, the samples without and with 3 days of pressure treatment were centrifuged at 16.000 rpm at 4 ^{o}C for 20 min in order to remove any insoluble material and the protein concentration of the supernatant was determined from the UV absorbance at 274.5 nm, using a molar extinction coefficient of 1440 $M^{-1}cm^{-1}$ (*43*). Protein was detected only for the pressurized IAPP (~ 17 % of the overall protein concentration). Immediately after the absorbance measurements, also far-UV CD spectra were taken. The HHP treated sample showed a strong negative band at about 200 nm and a positive band at 230 nm, characteristic for the presence of unordered structures (data not shown). The different fibrillar and non-fibrillar amorphous/oligomeric morphologies found for the high pressure treated sample indicate that not all IAPP aggregate structures are equally sensitive to pressure, hence suggesting the existence of pressure resistant fibrils with densely packed cores and a population that can be dissociated by HHP.

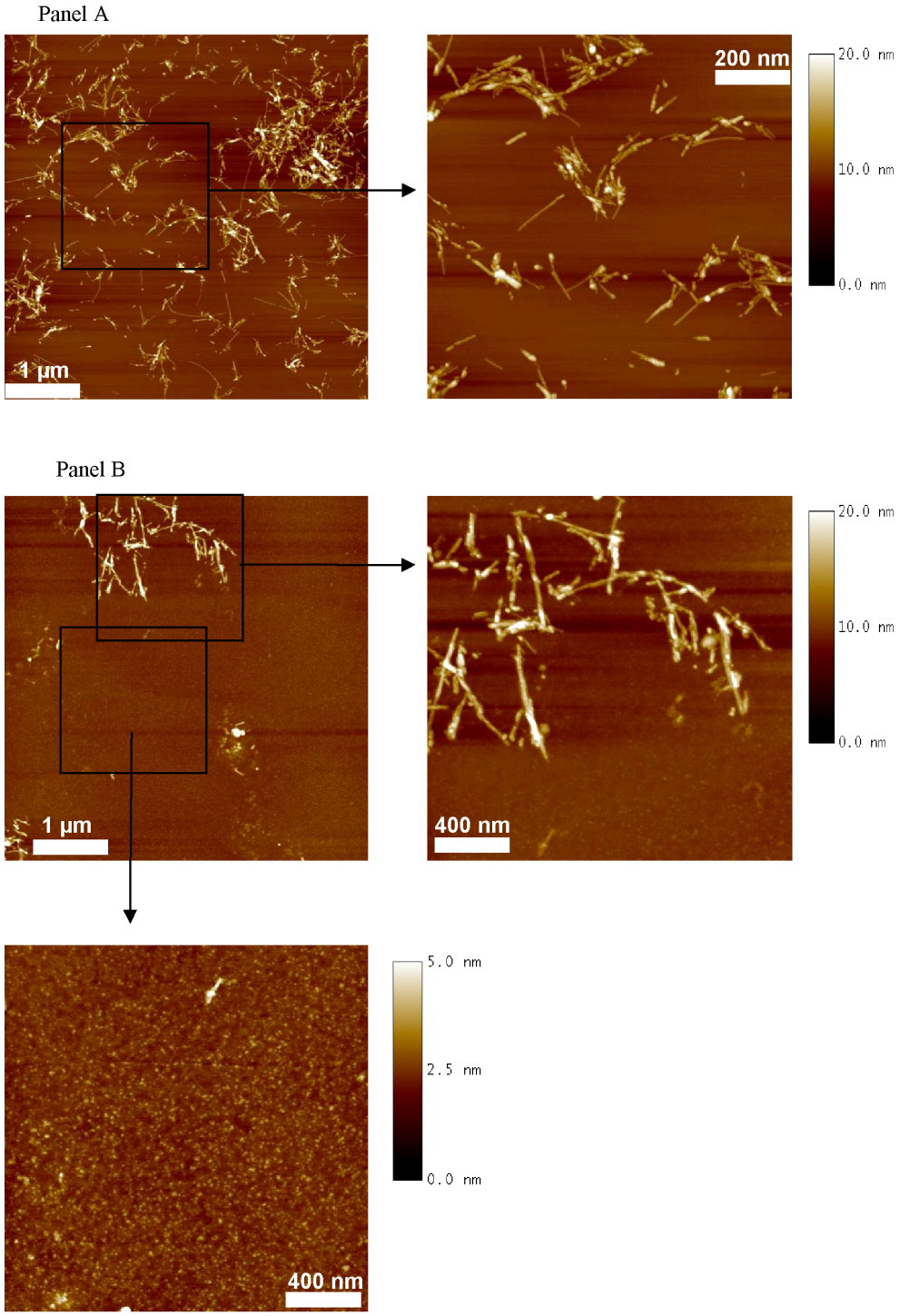

Figure 25 AFM height images of 0.1 wt% IAPP aggregates after 3 d without (panel A) and after pressure treatment at 3.5 kbar (panel B). The same samples analyzed by FT-IR spectroscopy were diluted with deionized water to yield a final concentration of 1 µM. 20 µL were applied onto freshly cleaved muscovite mica and allowed to dry before the AFM analysis.

3.1.2. Kinetics of aggregation of IAPP and IAPP fragments

We also carried out a detailed comparative kinetic study of the aggregation/fibrillation reaction of IAPP, IAPP 1-19 and IAPP 1-29 in neutral buffer at 37 °C by FT-IR spectroscopic analysis.

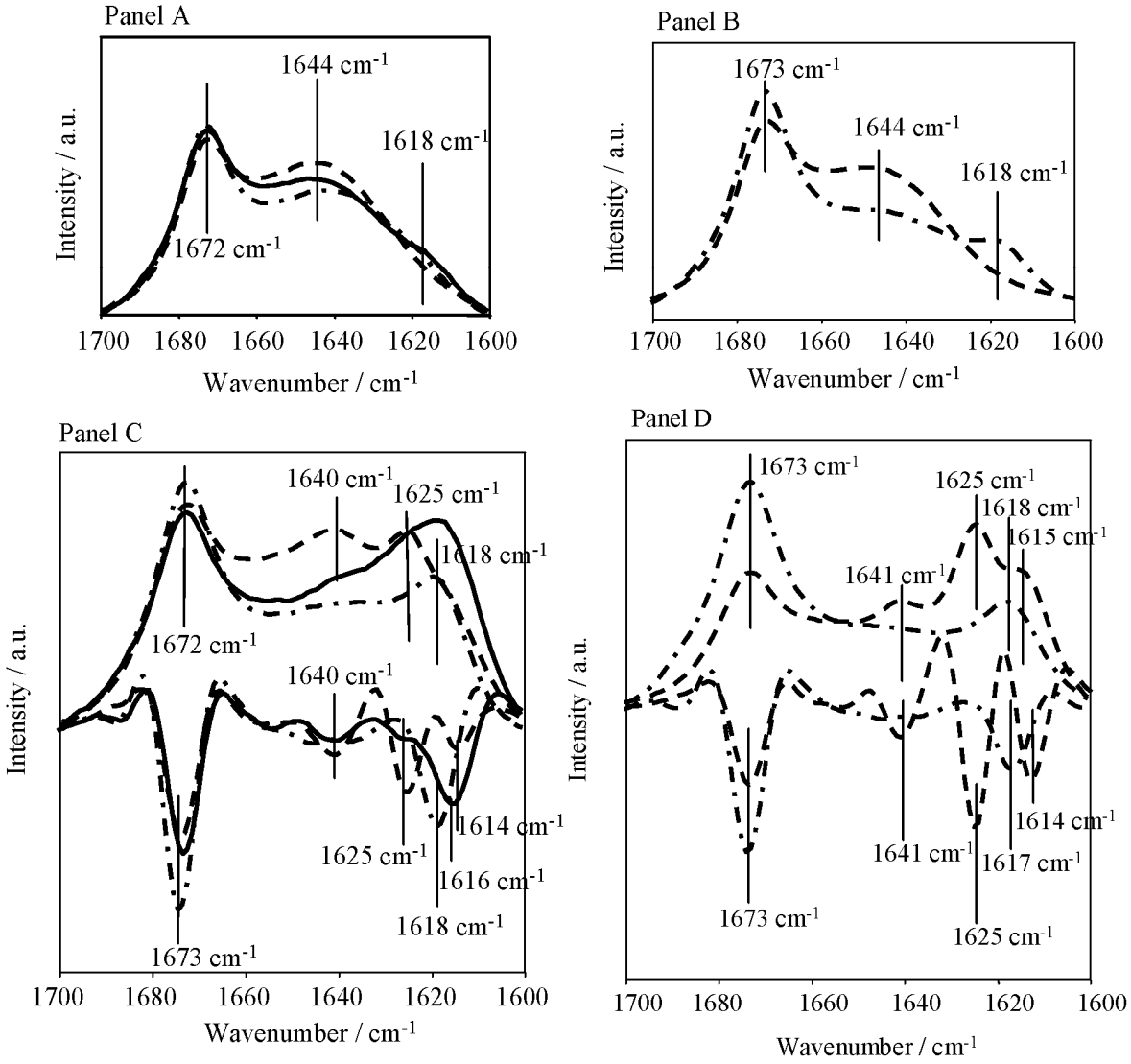

Figure 26 FT-IR spectra of freshly dissolved IAPP and fragments of IAPP at a concentration of 0.1 wt% (panel A) and 0.5 wt% (panel B): (-) IAPP, (- - -) IAPP 1-19, (-·-·-) IAPP 1-29. At the bottom of the figure, also the second derivative spectra are shown, which allow a more accurate determination of peak positions. All data were taken at T = 37 °C in 50 mM phosphate buffer (pD 7.4).

The peptides were originally dissolved in HFIP and subjected to overnight lyophilization prior to re-hydration in buffer. Whereas the full-length IAPP readily forms fibrils even at concentrations in the low μM range, the aggregation reaction of the fragments occurs in a reasonable time range at much higher concentrations, only. Hence, kinetic experiments were carried out at 0.1 and 0.5 % wt% solutions at $T = 37\ ^{o}C$.

All freshly dissolved peptides analyzed by FT-IR spectroscopy show a predominantly disordered conformation at time zero (Figure 26, panel A), indicated by a broad amide I' peak at ~ 1642-1644 cm^{-1}. Both, full length IAPP and IAPP 1-29 already contain a significant amount of □-sheet structures from the very beginning of the experiment at these concentrations. A characteristic shift from random coil to β-sheet structures is observed for all three peptides, with a significant amount of random/turn structures still present in the case of the two fragments even after 24 h (Figure 26, panel C). As revealed in Figure 26 (panel C), the random coil to beta-sheet conversion is much more pronounced for the full-length IAPP in comparison to the fragments. The position of the IR aggregate bands occurs at slightly different positions: at 1625 cm^{-1} for IAPP 1-19, at ~1618 cm^{-1} for IAPP 1-29 and at 1616-1618 cm^{-1} for full-length IAPP. For both the 1-19 and 1-29 IAPP fragments, the shift from random coil to β-sheet conformation occurs rather rapidly within the first 20 minutes, followed by a much slower increase in β-sheet content, not even reaching plateau values even after 3 h (Figure 27). Conversely, for full-length IAPP, after a slightly slower initial nucleation process, the random to β-sheet conversion is completed after about 40 min.

In order to ensure sufficient time for complete fibril maturation in all three cases, we incubated samples prepared in the same manner as for the FT-IR experiments at 37 ºC for 24 h prior to take aliquots for the AFM analysis (Figure 28). Due to the peak of remaining TFA in the sample, peak fitting of the data is not very precise, but the β-sheet content of the mature fibrillar state can be estimated from the FT-IR data assuming similar transition dipole moments for the various conformers. The β-sheet content at the end of the experiment (after ~20 h) is higher than 50 % for IAPP, ~ 32% for IAPP 1-19 and ~ 27 % for IAPP 1-29.

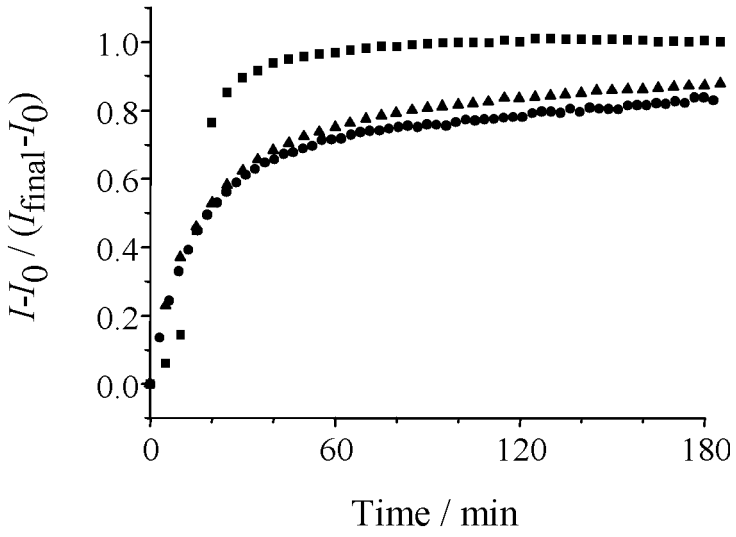

Figure 27 Kinetics of the aggregation process for all three (▪▪▪ IAPP, ▲▲▲ IAPP 1-19, +++ IAPP 1-29) based on the normalized maximum peak intensities in the β0-sheet region of the amide I' band. All data were taken at T = 37 °C in 50 mM phosphate buffer (pD 7.4).

Comparing the second derivative IR spectra at the final fibrillar structures (Figure 26, panel C), it can be seen that fragment IAPP 1-29 is the only one with a single peak in the β-sheet region, which appears at 1618 cm^{-1}. IAPP 1-19 shows two β-peaks, a major one at 1625 cm^{-1} and a small one at ~ 1614 cm^{-1}. For comparison, full-length IAPP shows a main peak at ~ 1616 cm^{-1} with a shoulder at ~ 1625 cm^{-1}. Both, full IAPP and fragment 1-19 exhibit an additional peak around 1640 cm^{-1} (much more pronounced for IAPP 1-29), indicating a high population of remnant unordered structures.

The different wave numbers assigned to individual peptide β-aggregate structures indicate different packing properties. The smaller the wave number is, the stronger the H-bond strength of the intermolecular β-sheet structure. Hence, compared to IAPP and fragment 1-29, fragment 1-19 seems to form less strongly H-bonded and more disordered β-sheet fibrillar structures. Considering the fact that fragment 1-29 shows essentially one peak in the β-sheet region, only (at ~ 1618 cm^{-1}), this indicates that in fragment 1-29 the amino-acid regions 1-19 and 20-29 seem to take part in forming β-strands cooperatively and pack efficiently against each other.

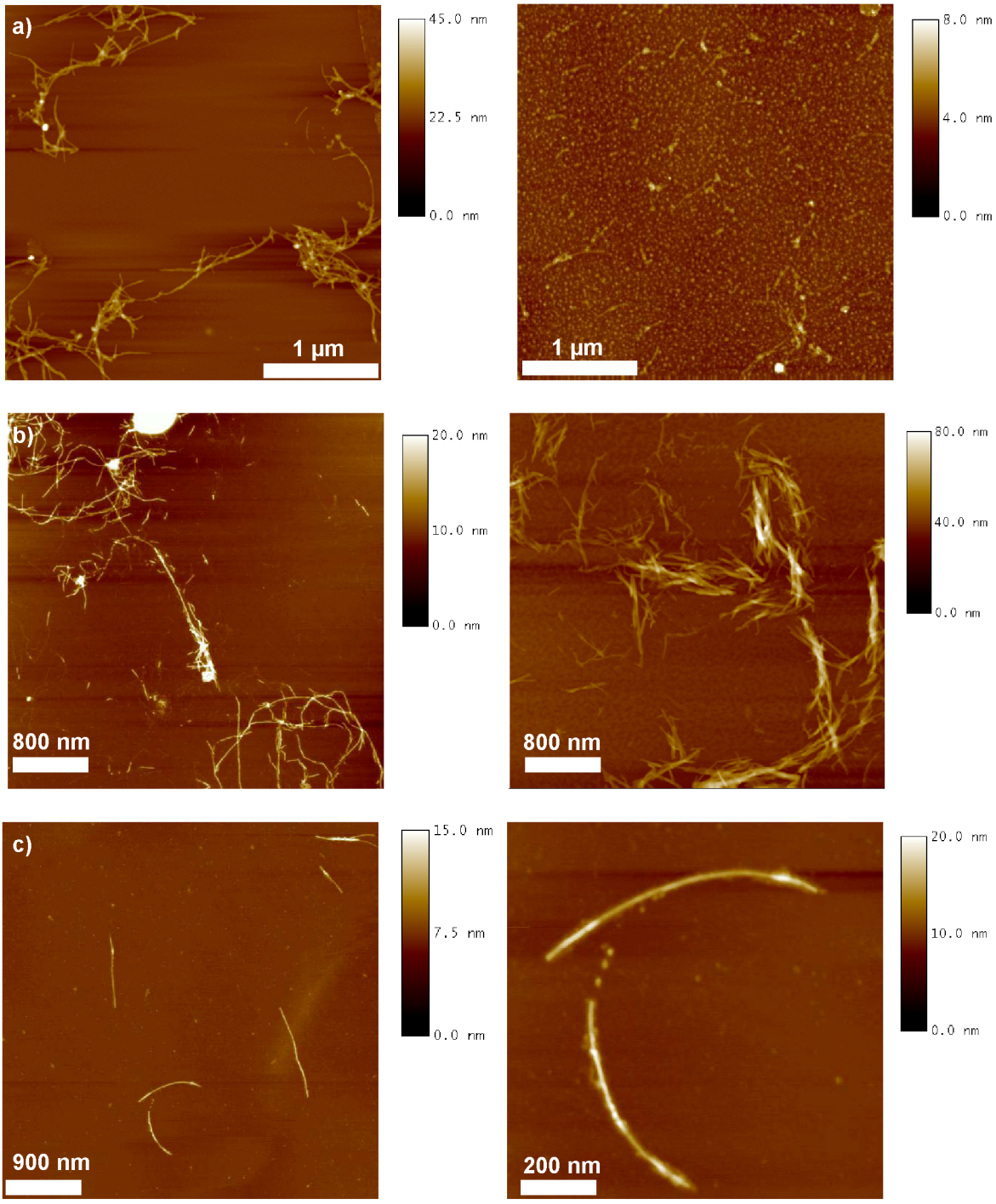

Figure 28 Selection of AFM height images of 0.1 wt% of a) IAPP 1-19, b) IAPP 1-29, and c) full-length IAPP aggregates after 24 h at 37 ºC. Samples incubated under the same conditions as those measured in the FT-IR sample cell were diluted with deionized water to yield a final concentration of 1 µM. 20 µL were applied onto freshly cleaved muscovite mica and allowed to dry before the AFM analysis.

To gain insight into the morphology and particular characteristics of the aggregate / fibril structures (size, length) formed by these three peptides, tapping-mode atomic force microscopy (AFM) studies were employed. Most aggregate structures seen for IAPP 1-19 (Figure 28a) under these preparation conditions are about 1-2 μm long. The sample seems to be rather polymorphic, with a relatively large population of different aggregate types with probably correspondingly different hydrogen bonding patterns (see the discussion of the FT-IR data above).

The following main types of structures could be identified: fibrils with 5-15 nm height and about 1-2 μm long, similarly to what is normally seen for full-length IAPP (Figure 26), thin protofibrils, having 1-2 μm length and 0.5-1.5 nm diameter, but also thick and short fibrils of less than 1 μm length and about 50 nm thickness are observed, probably as a result of considerable lateral growth of oligomers. In addition, some bent structures and a large population of oligomers (upper right corner of Figure 28 a) has been detected as well.

The corresponding fibrillar structures for IAPP 1-29 and full-length IAPP are shown in Figures 28b and 28c, respectively. IAPP 1-29 also presents a polymorphic behavior forming different types of fibrillar structures upon aggregation, ranging in length from 200 nm up to 2 μm with diameters of 5-15 nm as seen for IAPP as well. The fibrils are often found to be branched and sometimes also bent fibrils are found. Under these experimental conditions, IAPP forms mostly one type of fibrils, about 1-2 μm long with 15 nm diameter (Figure 28c). Often, bent structures are found as well. Oligomeric species and protofibrils are also present, but to a much lesser extent than for the IAPP fragments.

We have further increased the concentration of the fragments up to 0.5 wt%. A similar kinetics of aggregation was observed as in the case of the 0.1 wt% solution. The spectral characteristics are also similar to those of the lower concentration (Figure 26, panels B, D). For the IAPP 1-19 aggregate, we observe again two peaks, a major peak at 1625 cm^{-1} and a second one at 1614 cm^{-1}, the latter being more pronounced at this higher concentration (Figure 26, panel D). Hence, all the characteristics observed for the 0.1 wt% concentration are observed at this higher concentration as well, including the AFM morphologies of the fibrillar structures formed.

3.1.3. High pressure studies on IAPP fragments

High pressure studies were carried out on both IAPP fragments as well to reveal if high pressure treatment is able to disrupt the mature fibrillar structures formed by the 1-19 and 1-29 fragments. Samples were first incubated at 37 ºC for 24 h, thus allowing complete fibrillation. From these samples, aliquots were taken for FT-IR spectroscopic and AFM analysis. The samples were then subjected to high hydrostatic pressure (3 kbar) for 24 additional hours at 25 ºC.

Representative FT-IR results are shown in Figure 29. Unlike what we have previously observed for the pressurized full-length IAPP samples, the fragments show no major spectral changes when comparing the pressure-treated samples with the untreated ones. This suggests that the fragments form aggregates which are rather pressure-insensitive, i.e. contain densely packed cores which are more pressure-stable than full-length IAPP. This obviously holds true for all aggregate structures present which have been detected by AFM analysis, the oligomeric and the fibrillar ones. In accordance with the FT-IR spectroscopic data, the AFM pictures of the pressurized samples did not exhibit significant morphological changes as well (data not shown).

We pointed out in the introductory section that IAPP has not only one but several amyloidogenic cores that are interacting to form an organized aggregate structure and that hydrophobic interactions may drive the initial stage of the aggregation process. According to the literature, aggregation of the C-terminal domain of IAPP (amino acid residues 20-29 and 30-37) is thought to be most likely driven by hydrophobic interactions (*50*). Previous theoretical studies regarding secondary structure predictions of human IAPP indicate that there is one potential R-helical region between amino acid residues 8 and 14 and three potential β-strand regions. A β-turn has been predicted at Asn31, which would result in two adjacent β-strands (32-37 and 24-29); a third β-strand is proposed to exist in region 18-23 (*50*). These predictions have been complemented by experimental studies, showing aggregation into ordered fibrillar structures of fragments 8-20 and 8-37 as well (*47, 50*). Additionally, in our study, the comparison of the fibrillation of the different peptides indicates that IAPP 1-19, IAPP 1-29, and full length IAPP are all three capable of self-assembly under similar conditions in vitro, to different extents, however. Interestingly, we found that fragment IAPP 1-19 is also prone to self-assembly and fibrillation. These findings suggest that the only region of IAPP reported not to form fibrils so far is region 1-

13, to be more precise, region 1-8, which is the region exhibiting amino acid residues not prone to forming β-sheets. Rather, this region has been suggested to be responsible for membrane insertion (*52, 53*) and has most likely a modulating influence on conformational conversions and fibril formation (*50*). As HHP is acting to weaken or even prevent hydrophobic self-organization and electrostatic interactions, we may expect that application of HHP may be used as a measure to reveal the importance of these interactions in formation of aggregates and/or fibrils of IAPP and its fragments.

With all data taken together, a hypothetical model for IAPP fibril formation may be suggested: IAPP undergoes fast nucleation (due to several amyloidogenic "cores"), largely driven by hydrophobic interactions. Hence, formation and packing of fibrils are not perfect, and mixed-registry β-sheet structures might exist, in particular at these high protein concentrations that were used, which can partially be dissociated by pressure leading to smaller aggregate structures and oligomers. An HHP as low as 3 kbar is sufficient to weaken and (at least partially) disrupt the hydrophobic cores, thus leading to formation of a heterogeneous population of fibrillar aggregates with IR amide I′ bands in the low-wavenumber region (which is typical of a more strongly H-bonding pattern of intermolecular β-sheets) and a large amount of nonfibrillar smaller aggregates and oligomers, as detected by AFM. Our data also indicate that at least some of the preformed IAPP fibrils are sensitive to high hydrostatic pressure, similar to loosely packed, amorphous aggregates and inclusion bodies (*131, 157, 158*). Considering the fact that high hydrostatic pressure is an effective means of disturbing ionic and hydrophobic interactions but not hydrogen bonds, we can conclude that these former two types of interactions are also important for the stability of full-length IAPP fibrillar aggregates, as also suggested in work using denaturing agents (*43*).

Unlike full-length IAPP, the fragments investigated here exhibit an enhanced stability toward high-hydrostatic pressure treatment with maintenance of their fibrillar structures even up to pressures of 3 kbar. This points toward more densely packed aggregate structures with less defect volume and strong cooperative hydrogen bonding in these fragments when compared to full-length IAPP. The FT-IR data clearly indicate that fragment 1-29 has intermolecular β-sheet conformational properties different from those of fragment 1-19, the latter exhibiting polymorphic

behaviour with more disordered structures and less strongly H-bonded fibrillar assemblies. Obviously, hydrophobic interactions and electrostatic interactions as well as packing defects play a minor role in the IAPP 1-29 assemblies. Also, this indirectly implies that in the C-terminal region, hydrophobic interactions and/or less efficient packing for amino acid residues 30-37 (present in full-length IAPP, sensitive to high pressure) becomes more important than in fragment 20-29 (present in IAPP 1-29), which leads to the marked pressure sensitivity observed for full-length IAPP. The different molecular configurations of the peptides are probably the basis for the various structures and morphologies observed here. The packing of the residues outside the backbone region may constitute the observed polymorphisms.

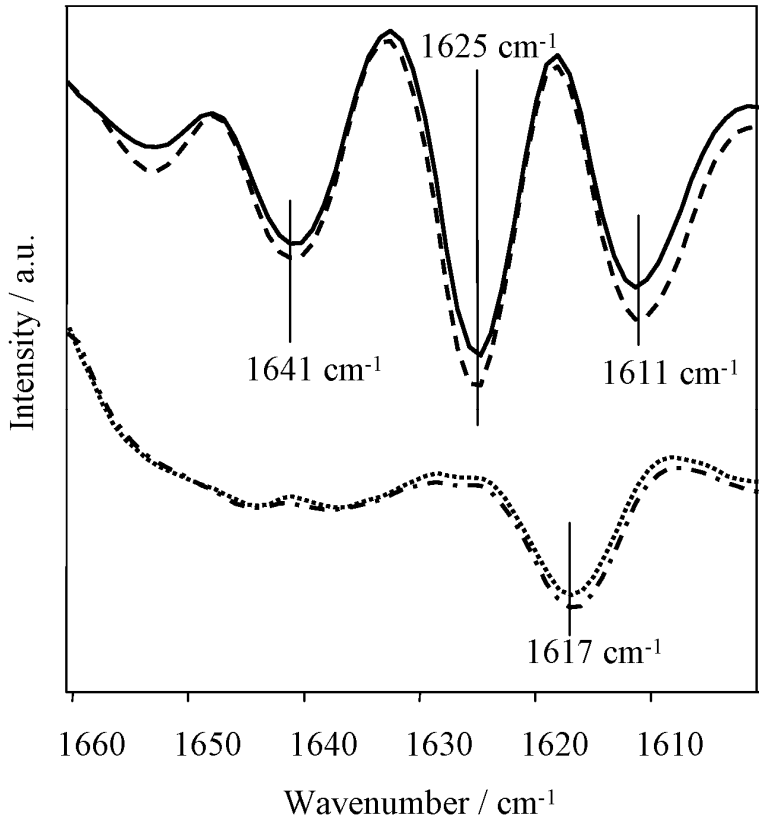

Figure 29 FT-IR spectra and the corresponding second derivative spectra of IAPP 0.5 wt% 1-19 (at the top of the figure) after 24 h of aggregation in 50 mM NaH_2PO_4 (pD 7.4) at ambient pressure (- - -), and after additional 24 h at 3 kbar (-). At the bottom of the figure, the FT-IR spectra and the corresponding second derivative spectra of IAPP 1-29 after 24 h of aggregation in 50 mM NaH_2PO_4 (pD 7.4) at ambient pressure (-.-.-) and after additional 24 h at 3 kbar (**…..**) are shown. All data were taken at $T = 37\ ^{o}C$.

3.2. Studies on IAPP fibril formation at heterogenous raft lipid interfaces (by confocal/two-photon excitation fluorescence microscopy

The lipid mixture DOPC: DPPC: cholesterol 1:2:1 displays liquid-ordered (l_o) / liquid-disordered (l_d) phase coexistence at room temperature. By gradually increasing the temperature, the transition to the all-fluid l_d phase was detected to take place at ~ 40 °C (Figure 30). For visualization, we used the membrane fluorescence marker rhodamine-DHPE which is known to preferentially label the l_d phase (displayed in grey in Figure 30), rather than the l_o phase (displayed in black). Above ~ 40 °C, the fluorophore was found to be homogenously distributed all over the membrane surface of the GUVs, indicating the presence of a homogenous l_d phase. Below that temperature, phase separation can be clearly seen.

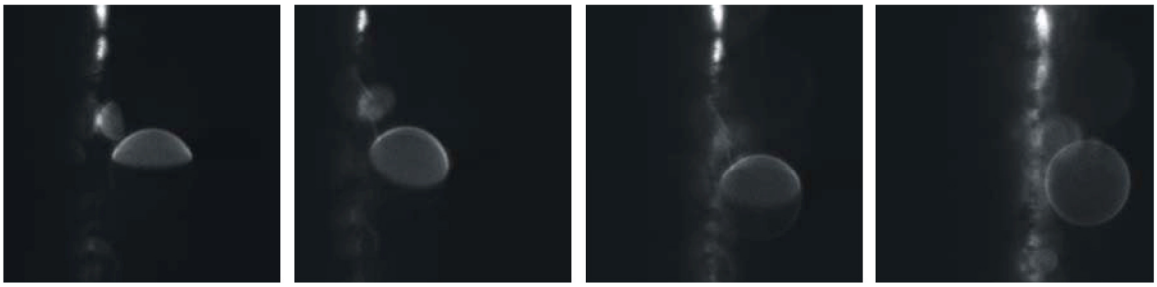

26.6 ºC 34.2 ºC 39.9 ºC 43.1 ºC

Figure 30 Temperature scan for GUVs made from DOPC : DPPC : cholesterol 1:2:1. The GUVs display l_o / l_d phase coexistence at room temperature. The transition from the l_o / l_d-coexistence region to the l_d phase occurs at ~ 40 ^{o}C. Rhodamine-DHPE was used as membrane marker, labeling preferentially the l_d domains (displayed in grey). The vesicle size is ~ 30 μm.

Since we are essentially interested in the lipid phase coexistence region here, and how it can modulate peptide insertion and the fibril formation process of IAPP, the peptide was added into the system at room temperature, i.e., at 25 °C (Figure 31). Prior to peptide insertion into the membrane, no significant cross-talk between the red (rhodamine-DHPE) and the green (Bodipy-FL) channel was detected (Figure 31, 0 min). Within 1-2 minutes after peptide addition, insertion of the C-terminally Bodipy-FL-labeled IAPP (IAPP(1-37)-K-Bodipy-FL) into the GUVs membranes is already detected. Moreover, the peptide seems to preferentially partition into the l_d phase, already strongly affecting the lipid bilayer integrity within minutes after its addition.

Our time-lapse study indicates drastic changes in the GUVs morphology due to the strong interaction with IAPP, especially within the first hour of interaction (readings at 2, 35 and 60 min, after exposing the membrane to the peptide). With time, IAPP induces detachment of the otherwise stable GUVs from the platinum wires and incorporation of membrane lipids into the growing fibrils. Therefore, bent structures (after ~ 1 h) and circularly-shaped fibrils (after ~ 72 h) grow on the surface of available GUV templates. After ~ 72 h of incubation, a perfect overlap of the fluorescent signals in the two detection channels is seen, and no intact GUVs are detectable at this point anymore. These findings indicate an overall pronounced association/incorporation of lipids into the growing IAPP fibrils.

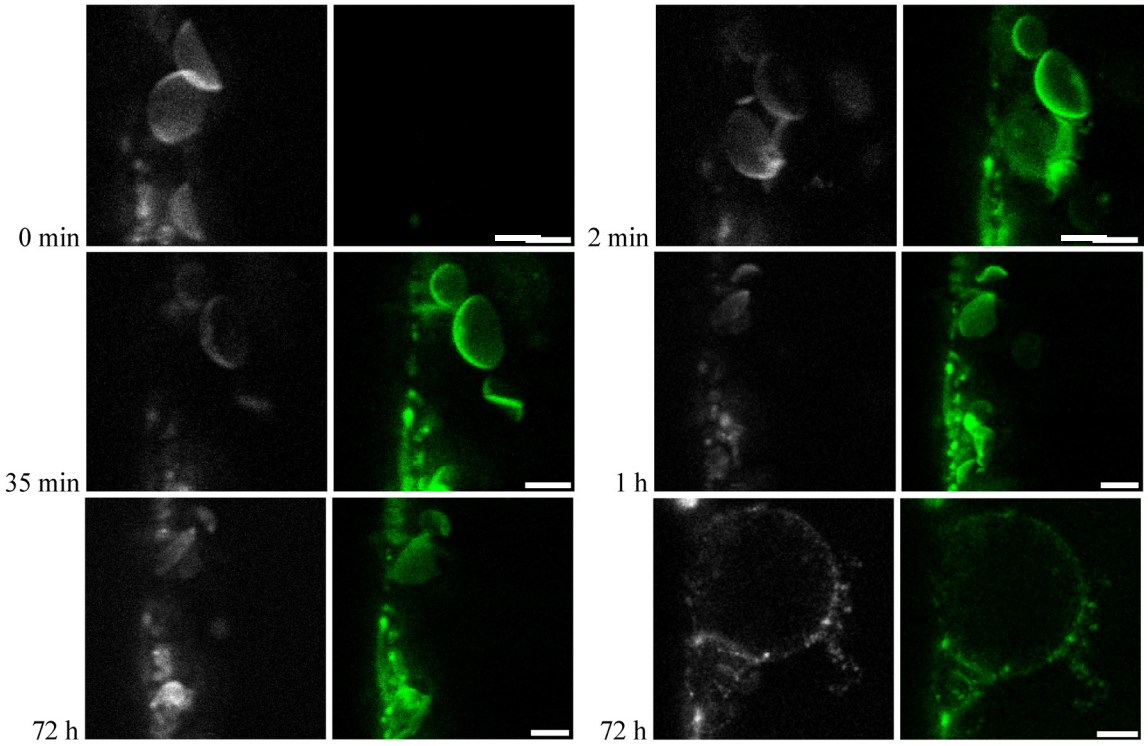

Figure 31 Interaction of IAPP with raft-like GUVs (DOPC : DPPC : cholesterol 1:2:1) monitored at room temperature. C-terminally labeled IAPP (IAPP-K-Bodipy-FL, displayed in green) inserts preferentially into the l_d lipid phase (displayed in grey), the insertion being already detectable 2 min after peptide addition (5 µM). The strongest effects are observable within the first hour of interaction. With time, IAPP fibrils grow at the expense of membrane material, adopting a circular shape, thus reflecting the shape and size of the GUVs which serve as template here (~ 30 µm diameter). The scale bar represents 10 µm.

For comparison, we have also investigated the interaction of the same lipid system with unlabeled IAPP (data not shown). Identically prepared GUVs were in this case treated with 5 μM IAPP instead of 5 μM IAPP-K-Bodipy-FL. Under these conditions, we did not detect any influence of the fluorescence label on the interaction with the lipid membrane, and thus, on the mechanism and kinetics of IAPP aggregation. A similar kinetics of interaction and effect on membrane interaction and disruption is observed, with the most drastic changes occurring within the first hour after addition of the peptide. This finding is also in agreement with supplementary atomic force microscopy (AFM) measurements showing disruption of the raft membrane at an early stage of the fibrillation reaction of IAPP (data not shown).

Several studies reported in the literature had previously indicated that the positively charged N-terminus is responsible for the insertion of IAPP into negatively lipid monolayers mainly via electrostatic interactions (*53*), and this is also the reason why we opted for the C-terminal labeling of IAPP (PSL Laboratories, Heidelberg). However, understanding IAPP-membrane interactions seems to be more complex, and electrostatic interactions are probably not the only important type of interaction present (*52*). It is to be noted that the even more positively charged rodent IAPP does not seem to insert strongly into negatively charged membranes (H18 in human IAPP corresponds to R18 in rodent IAPP) (*53*) and that the negatively charged DNA has a less pronounced accelerating effect on IAPP fibril formation as compared to anionic lipids (*37*), thus strengthening the important role of the hydrophobic lipid core region in IAPP fibril formation.

Recently, it has been suggested that the interaction of IAPP with lipid head-groups via charge interaction might essentially lower the energy barrier for separating neighboring lipid molecules and inserting between the lipid chains (*27*). The previously reported literature data, and the strong peptide-membrane interaction observed in our study on the zwitterionic raft-model system, involving membrane damage, associated fibril growth and lipid incorporation into the growing fibrils, clearly demonstrate that the nature of the interaction is not purely electrostatic, but rather that, once adsorbed and partially inserted, IAPP will interact with the membrane via hydrophobic interactions, thus facilitating further peptide penetration, which leads to an increase in local peptide concentration in the core region of the membrane.

Once hydrophobic patches of membrane lipid chains are exposed to IAPP, the peptide will probably start "pulling" membrane lipids into the growing fibrils. In fact, hydrophobic interactions are also considered to be a major driving force in IAPP fibril formation in the absence of membranes (*124*). These findings may as well be the starting point of further studies on amyloidogenic peptides regarding the modulation of fibril formation by lipid *in vivo*.

To diminish energetic costs, initial incorporation of the peptides at the rim of the domains of the heterogeneous membrane, where the volume fluctuations are most prominent, would be most likely, leading to a favorable decrease of the associated line energy. The increase in membrane defects upon incorporation of the peptide will facilitate further peptide penetration, which leads to an increase in local peptide concentration in the core region of the membrane, thus allowing condensation of oligomeric particles and fibril growth. As the biological membranes are composed of a plethora of more or less fluid-like and raft-like domains, the strong membrane-disrupting potency of IAPP oligomers in heterogeneous membranes might be the reason for its cytotoxicity. Furthermore, extraction of lipids may be a common feature of amyloid formation *in vivo*, since extracellular amyloid deposits from a number of diseases have been found to be associated with cellular lipids (*19*). These findings would have to be taken into account in the design of inhibitors for therapeutic approaches.

3.3. Studies on IAPP fibril formation, associated cytotoxicity and their inhibition by resveratrol using the INS-1E cell line as model system

3.3.1. Fluorescence imaging and cytotoxicity studies on the interaction of IAPP with INS-1E cells and the inhibitory effect of resveratrol

We also visualized the interaction of IAPP with INS-1E cells (Figure 32), and additionally reveal the IAPP species formed in the presence of this potent inhibitor, with the aid of fluorescence microscopy imaging. IAPP readily inserts into the cell membrane within the first minutes of interaction (readings at 10, 20, 30 min, 1 h, data not shown), and fibrils grow at the expense of cellular membranes. After 3 h, fibrils already incorporated lipid membrane material, leading to structures of about 10 μm lengths and 2 μm thicknesses (Figure 32, 3 h).

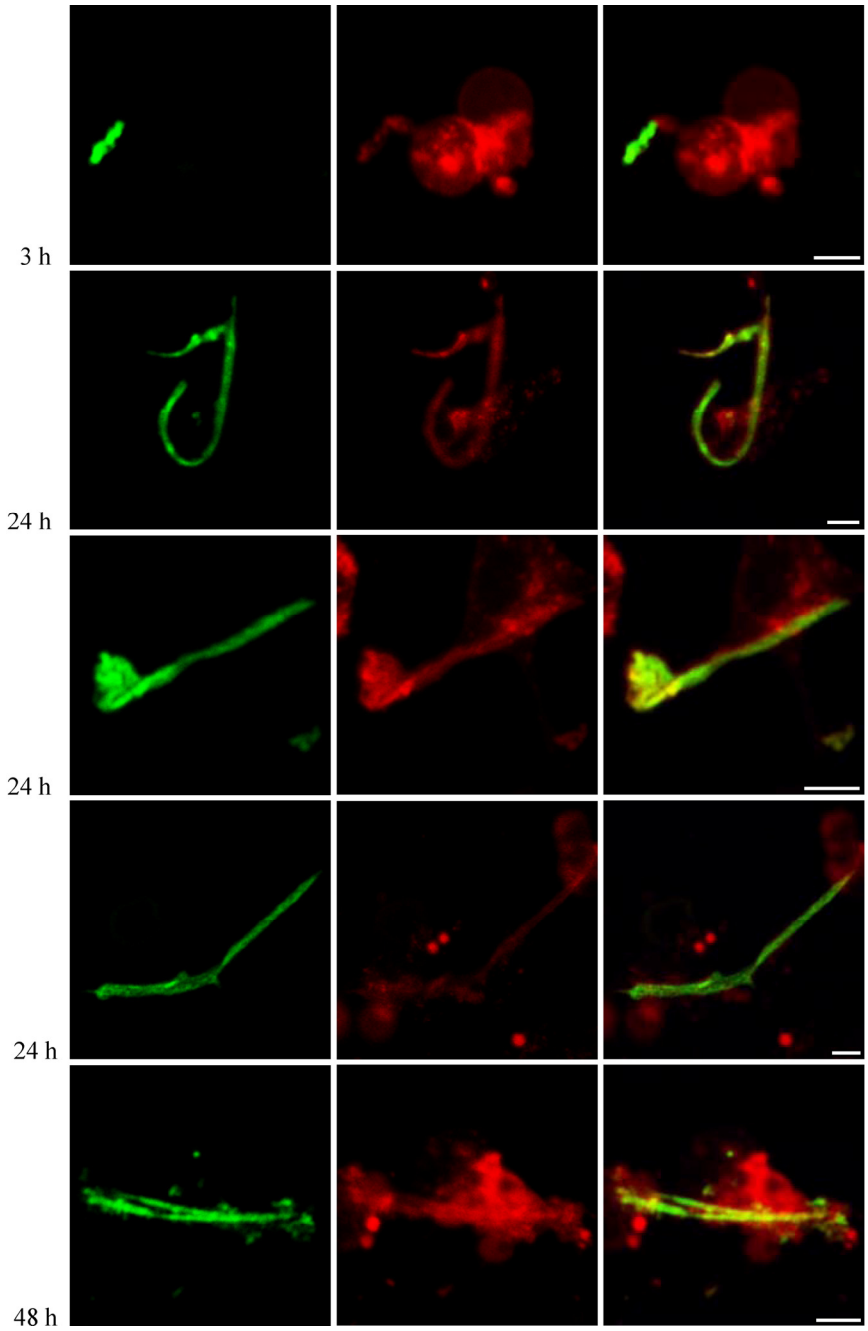

Figure 32 Interaction of IAPP with INS-1E cells at different time points monitored by fluorescence microscopy. The barrier function of cellular membranes is lost in the presence of IAPP, lipids getting incorporated into the growing IAPP fibrils (25 - 50 µm length, 1.5 - 4 µm thickness). After 24 h, no significant increase in fibril dimensions was observed anymore. Non-treated cells were used as control (data not shown). Green: IAPP-K-Bodipy-FL, red: Texas-Red DHPE labeled INS-1E cells, yellow: merge of the two detection channels showing co-localization of IAPP and cell membranes. The scale bar corresponds to 10 µm.

As the barrier function of the cellular membranes is lost, lipids and cellular material gets incorporated into the growing fibrils, thus explaining the unusual thickness and length of the fibrils (i.e., 25 - 50 μm length, 1.5 - 4 μm thickness) compared to the corresponding dimensions in the *in vitro* studies (*72, 124, 151*). A branching and twisting tendency was also observed. In all investigated samples, cellular lipids were incorporated into the fibrils, and after 24 h no significant increase in fibril dimensions was observed anymore. By using non-treated cells as well, it was obvious that the observed cellular morphological changes can be attributed to IAPP-induced cell death, in line with results using the WST-1 assay (Figure 33).

Extending the discussion regarding the interaction of IAPP with lipid membranes, it is quite obvious that in the case of cellular studies, the situation may be much more complex. It is not only the lipid membranes that create a hydrophobic environment, thus allowing IAPP to penetrate into the lipid bilayer. Additional factors might also play an important role in attracting IAPP to the cellular surface, thus facilitating its aggregation. For example, binding to basement membrane heparan sulphate proteoglycans might additionally contribute to amyloid formation (*159*).

A synthetic compounds, phenolsulfonphthalein, has been shown to inhibit IAPP fibril formation also (*160*), but still, with synthetic compounds, cell toxicity remains an issue for drug development. On the other hand, naturally occurring polyphenolic compounds have an advantage over synthetic ones because of their nontoxicity as well as their biocompatibility. These characteristics of naturally occurring polyphenolic compounds have been exploited for the discovery of A β and other amyloid inhibitors. In an elegant study, Wanker's group has shown that EGCG, a naturally occurring polyphenolic compound, can inhibit amyloid formation of Aβ and α-synuclein (*75, 76*). One other important polyphenolic compound, resveratrol, which is found in grapes and red wine, has been shown to inhibit the cytotoxicity of Aβ (25–35) and to prevent its fibril formation (*77, 161, 162*).

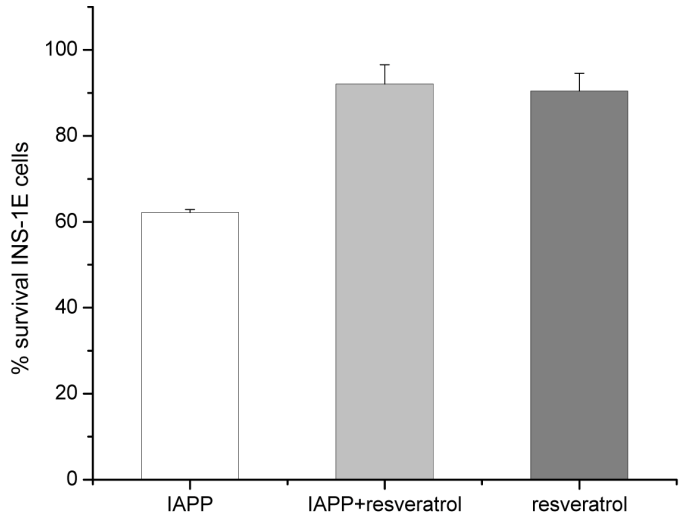

Figure 33 Cell viability of pancreatic β-cells (cell line INS-1E) after exposure to 10 μM IAPP (white), 10 μM of both IAPP and resveratrol (light grey), and 10 μM resveratrol, only (dark grey).

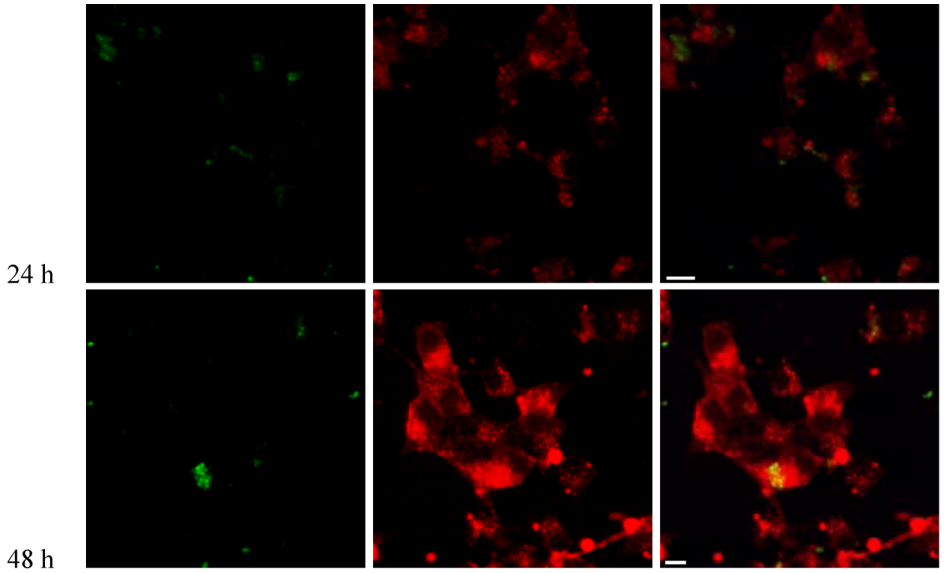

Figure 34 Inhibition of IAPP fibril formation and reduced cytotoxicity in the presence of resveratrol on INS-1E cells at different time points. Cells were exposed to mixtures of IAPP and resveratrol at a 1:1 molar ratio. Both for the 24 and 48 h-treated samples, no fibrillar structures are observed. The intact cell morphologies account for the reduced cytotoxicity acquired by efficient inhibition of IAPP aggregation by resveratrol at an early stage. Small spherical oligomeric particles (~1.5 μm diameter), possibly non-toxic off-pathway oligomers, are detected both in the vicinity of the cell membrane as well as in the bulk. Green: IAPP-K-Bodipy-FL, red: Texas-Red DHPE labeled INS-1E cells, yellow: merge of the two detection channels, showing the localization of IAPP non-toxic oligomeric aggregates, both near INS-1 E cell membranes as well as in the bulk. The scale bar corresponds to 10 μm.

The effect of resveratrol on IAPP fibril inhibition was studied by using the pancreatic cell line INS-1E. The first test was a standard WST-1 assay, performed as described in the methods section. In a control experiment, only 60% cells survived in the presence of 10 IAPP (Figure 33). In the presence of 10 μM resveratrol, the survival of the cells increased to about 90 %. As depicted in Figure 33, resveratrol itself is nontoxic to the cells at 10 μM concentrations. This shows that resveratrol is not only an effective *in vitro* inhibitor, it can also be considered a potent inhibitor in the cellular model system as well. Inhibiting the formation of oligomeric and fibrillar species during amyloid formation is a promising approach to prevent amyloid-related diseases.

It is clearly seen that resveratrol arrests IAPP fibril formation and associated cytotoxic effects at an early stage (Figure 34). Since it is generally believed that early oligomers may be more cytotoxic than mature fibrils, it can be speculated that in this case resveratrol leads to formation of non-toxic, off-pathway amorphous aggregates of approximately 1.5 μm diameter. Insertion into the membrane is largely prevented, since such structures are also visible in the bulk as illustrated in Figure 34, both for the 24 h-, as well as for the 48 h-treated sample.

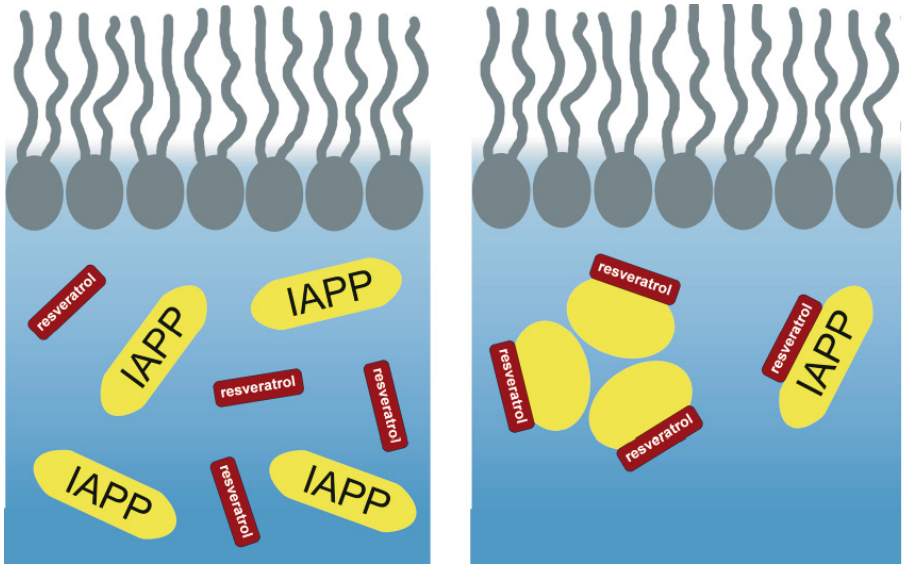

Figure 35 Schematic illustration of the inhibitory effect of resveratrol on IAPP fibrillation at lipid membrane interfaces (*59*).

We have also tried to use Congo Red and Thioflavine T (ThT) staining of the fibrils formed. However, we encountered that ThT was found to be toxic to INS-1E cells in the

concentration range required for quantitative estimation of IAPP fibril formation (several μM). Also Congo Red showed pronounced non-specific binding to the cellular membranes of INS-1E cells. Moreover, we found a pronounced spectroscopic cross-talk between this dye and the cellular membrane marker Bodipy-DHPE, which was used in this approach in combination with Congo Red. As a consequence, we have opted for a different approach, where we simultaneously monitored two fluorescent dyes, with Bodipy covalently coupled to the IAPP molecule, and rhodamine-DHPE as cellular membrane label.

Interestingly, membrane incorporation into IAPP fibrils was also observed in our cellular studies on INS-1E cells, fibrillar structures being typically 25-50 μm long and 1.5-4 μm thick. Our conclusions on model-raft systems and INS-1E cells are very well complemented by studies of Sparr et al. (*25*), who used different (non-raft) model lipid systems and a different cell line, and also observed lipid uptake into amyloid fibers, ruling out formation of discrete protein pores (*26*). All these results clearly point towards the incorporation of lipid upon IAPP fibril formation, with hydrophobic interactions being a major player in membrane-associated amyloid formation and thus possibly in the onset of T2DM, once the barrier function of the cell membrane is lost. It may very well be that lipid-containing amyloid aggregates are universal structures of amyloid in living cells.

The imaging studies additionally indicate that the pronounced cytotoxicity of IAPP on INS-1E cells can be largely overcome by inhibition of IAPP fibrillation by the red wine compound resveratrol, which is able to arrest IAPP fibril formation at an early stage, possibly leading to the formation of non-toxic, "off-pathway" large oligomeric and amorphous structures. Our fluorescence microscopy results, taken together with the WST-1 assay outcome (*151*), clearly show that the changes in morphology observed for cells treated with IAPP-resveratrol mixtures, compared to IAPP-treated cells, correlate with a change in toxicity. The findings presented here are also in line with additional X-ray reflectivity studies on the interaction of IAPP with resveratrol in the presence and absence of membrane interfaces (*59*). Several studies from our group (*59, 148, 151*) indicate a stoichiometric interaction between IAPP and resveratrol, which leads to the formation of soluble complexes of peptide-inhibitor in the bulk, most likely via π-π stacking interactions, thereby preventing the insertion of IAPP into membrane bilayers (see also figure 35 for a proposed model for the inhibition mechanism). Since resveratrol is non-toxic to pancreatic β-

cells, this natural polyphenol might have the potential to be developed as drug candidate against T2DM, and presumably towards other amyloidogenic diseases as well in the future.

3.3.2. Identifying the nature of the major IAPP cytotoxic species

3.3.2.1. Kinetics of IAPP fibril formation monitored by the ThT assay

The ThT assay for 100 μM IAPP in acetate buffer, pH 5.5, at 10 ºC (Figure 36), indicates a slow kinetics of aggregation with a lag phase of ~ 100 h, followed by a slow exponential growth phase, the fibril formation process being almost complete only after ~ 400 h.

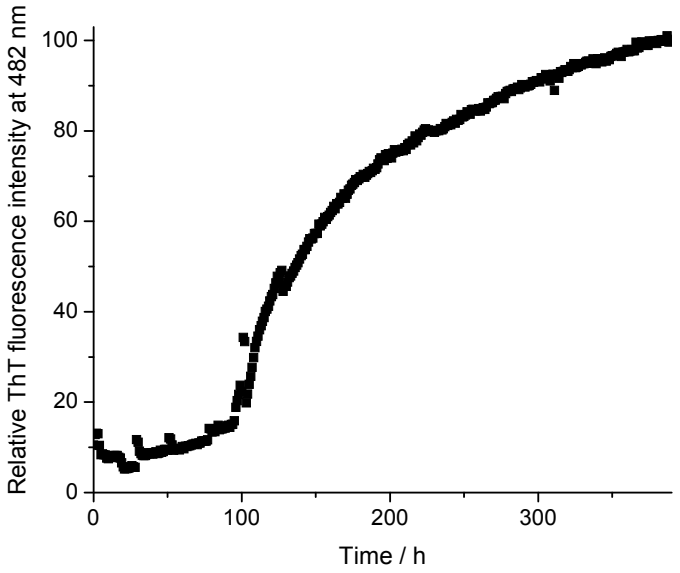

Figure 36 100 μM IAPP incubated with a final 50 μM ThT concentration (after blank subtraction and normalization) in 10 mM natrium acetate buffer, pH 5.5, 10 °C, monitored for 400 h (when the maximum ThT fluorescence intensity was reached, where the fibril formation process was assumed to be essentially complete).

The findings of the ThT kinetics assay are in good agreement with the characterization of monomeric, oligomeric, protofibrillar and mature fibrillar IAPP species, as detected by AFM analysis of samples aliquoted at different time points (Dr. Katrin Weise, personal communication). The same time points, i.e. 0 h, 7 h, 25 h, 50 h, 100 h, 150 h, 250 h, 504 h (3 weeks), and 672 h (4 weeks), respectively, were also considered for isolating the species to be tested for their cytotoxicity on INS-1E cells by the WST-1 assay.

3.3.2.2. Comparative cytotoxicity of various IAPP aggregation species investigated by the WST-1 cell proliferation assay

Figures 37 (10 μM IAPP final concentration, after 1:10 dilution with cell culture medium of 100 μM IAPP samples aliquoted at different time points) and 38 (20 μM IAPP final concentration, after 1:10 dilution with cell culture medium of 100μM IAPP samples aliquoted at different time points) clearly indicate differential effects of various IAPP aggregation stages on the survival rate of INS-1 E cells; moreover, a concentration dependence can be detected, the cytotoxic effects being more pronounced in the case of cells treated with 20 μM IAPP.

Thus, comparing the ThT curve with the WST-1 outcome, a strong correlation between the time frame of the lag phase (0-100 h) and the pronounced cytotoxicity registered for samples aliquoted within this time period is seen. The data suggest an increased cytotoxicity of the monomeric and early oligomeric IAPP species. Almost no significant difference can be noticed among the 0 h, 7 h, 25 h, 50 h and 100 h samples, the survival rates for these particular time points being practically in a plateau region (~ 5 - 10 % for 10 μM IAPP and 1 - 2 % for 20 μM IAPP, respectively).

As the nucleation and growth reaction proceeds, the ThT intensity increases, correlating with a significant decrease in cytotoxicity for samples tested within this time region, both in the case of the 10 μM, as well as for the 20 μM IAPP-treated cells. Late protofibrils (samples isolated after 150 h, 250 h) lead to 80-85% survival rates for 10μM IAPP-treated samples, and 50-60% survival rates for 20 μM IAPP-treated samples, respectively. The mature fibrils (samples isolated after 3 weeks, 4 weeks) display the lowest comparative cytotoxicity, cellular survival reaching in this case 90 % for 10 μM IAPP and 75 - 80 % for 20 μM IAPP, respectively.

Our findings support the recent hypothesis stating that the early IAPP oligomers are the species responsible for IAPP cytotoxicity (*70*). This is also to be expected, considering the proposed mechanism of interaction of IAPP with lipid membranes. Monomeric IAPP molecules are able to insert into membranes *via* their positively charged N-terminus. Hence, monomers and/or early oligomers probably accumulate at the membrane surface *via* electrostatic interactions between the peptide N-terminus and the zwitterionic lipid head-groups. For oligomeric species

hydrophobic interactions with the membrane acyl chain region might play a significant role as well. Once initial binding is achieved, further peptides are recruited and elongation is promoted.

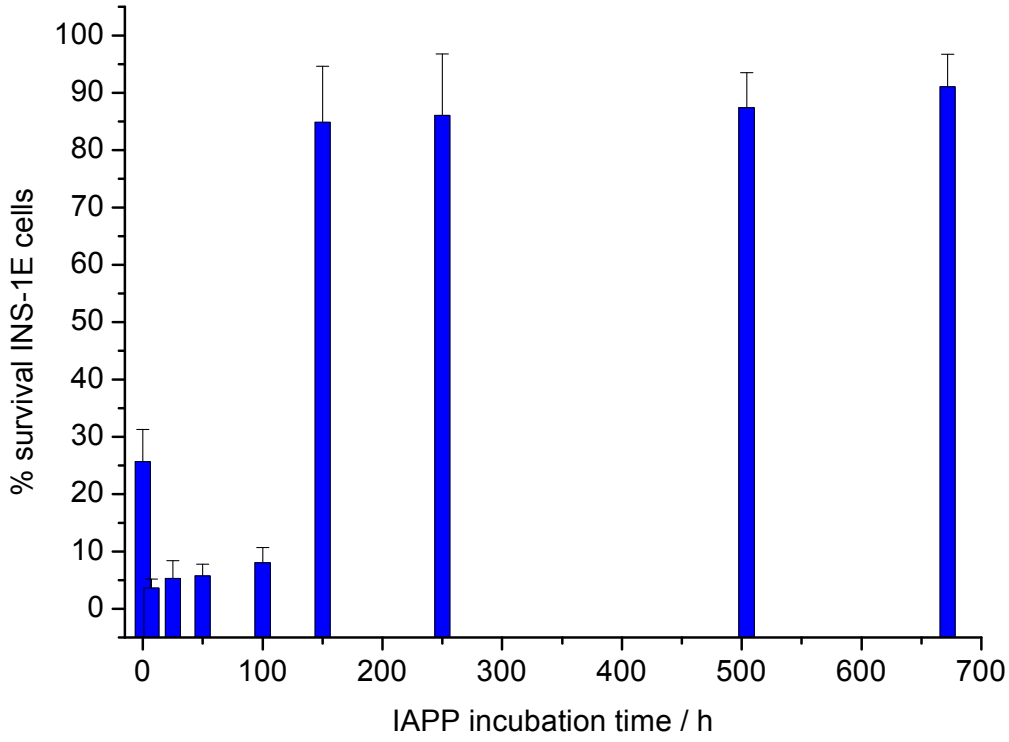

Figure 37 Cytotoxicity of IAPP aggregates added at a final concentration to 10 µM IAPP in cell culture medium onto INS-1E cells, estimated by the WST-1 cell proliferation assay. Cells were seeded into 96-well microtiter plates and allowed to grow (5% CO_2, 37 ºC) for 24 h prior to a 24 h-exposure to potentially cytotoxic IAPP species (incubation time: 0 h, 7 h, 25 h, 50 h, 100 h, 150 h, 250 h, 504 h, 672 h). The peptide was then removed and the cells were incubated for 24 h with the WST-1 reagent.

Thus, when previously isolated monomers, oligomers, protofibrils, late fibrils, and mature fibrils, respectively, are added onto the cellular membranes, the strongest interaction will be with the smallest species, i.e. monomers and early oligomers. Mature IAPP fibrils and late IAPP protofibrils are the least reactive IAPP species, already stabilized by intermolecular interactions between individual peptides, and thus they are less likely to interact with membranes. However, their increased size (several µm length) compared to individual monomeric peptides, can still exert

mechanical stress on the cell membranes, which might lead to perturbations in their barrier function, and thus could account for the slight cytotoxicity observed (~ 25% for 20 μM IAPP, ~ 10% for 10 μM IAPP, respectively).

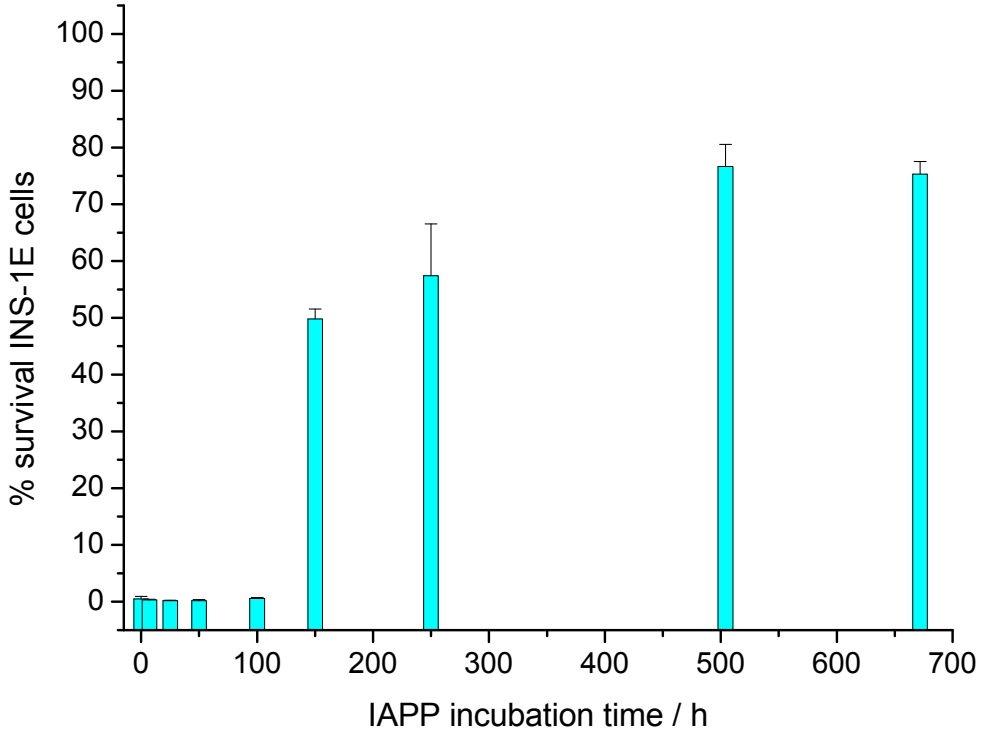

Figure 38 Cytotoxicity of IAPP aggregates added at a final concentration of 20 μM IAPP to cell culture medium onto INS-1E cells, estimated by the WST-1 cell proliferation assay. Cells were seeded into 96-well microtiter plates and allowed to grow (5% CO_2, 37 ºC) for 24 h prior to a 24 h-exposure to potentially cytotoxic IAPP species (incubation time: 0 h, 7 h, 25 h, 50 h, 100 h, 150 h, 250 h, 504 h, 672 h). The peptide was then removed and the cells were incubated for 24 h with the WST-1 reagent.

Identifying and characterizing the major cytotoxic species is of great importance for amyloidogenic diseases research, as understanding the mechanism of interaction and cytotoxicity on cellular membranes might provide the platform for successful strategies for the rational design of anti-amyloid (anti-fibrillogenesis, anti-cytotoxicity) inhibitors.

4. Summary

In this work, several aspects regarding the aggregation of IAPP which are essential for understanding T2DM were investigated. The fibril formation process was studied both in the absence and presence of lipid and cellular membranes. The first approach was to study the effect of high hydrostatic pressure on IAPP fibril formation, and comparatively on IAPP fragments, to understand the nature of the interactions governing fibrillar self-assembly. Additionally, the interaction of IAPP with the so far neglected model raft systems was investigated. Finally, the studies were to cellular membranes as well. IAPP cytotoxicity and the nature of the toxic species to pancreatic cells in culture was also addressed, including potential strategies to inhibit IAPP cytotoxicity and fibril formation by the red wine compound resveratrol. Based on all these data taken together, a model of interaction and inhibition could be proposed.

Using the pressure variable, additional details of the polymorphic forms of amyloid and its precursors as well as the transformation processes between these polymorphic states could be revealed. It was seen that the conformational stability of the fibrils varies, probably reflecting the difference in side chain packing inside the amyloid fibrils. The amino acid sequence of a polypeptide is optimized by evolution for folding into the native conformation, but it is unlikely that a tight packing of the side chains can also be achieved for all residues in the non-native fibrillar structures. This is in accord with findings that amyloid fibrils made of short peptides or fragments of amyloidogenic proteins, such as of IAPP in this study or of TTR, can be more densely packed. Fragments of IAPP showed a relative increased stability against pressure-treatment, suggesting tighter packing of their peptidic chains. An amyloid structure without optimal packing is likely to enable formation of various isoforms, suggesting the structural basis of multiple forms of amyloid fibrils in contrast to the unique native fold of functioning proteins. A disease caused by fibrillation of a protein often shows variations in terms of phenotypes and incubation periods. Such phenomena are termed strains and are thought to be connected to the fact that fibrils, also depending on the environmental conditions, can have various structural isoforms known as morphologies. IAPP seems to belong to this class of amyloidogenic proteins as well. In analogy to the multiple-kinetic-pathway folding tunnel described by the energy landscape for

globular protein folding, it seems very likely that there are generally also multiple routes to the formation of mature amyloid.

The interaction studies with the model-raft lipid system DOPC : DPPC : cholesterol 1:2:1 (a lipid mixture displaying l_d / l_o phase coexistence at room temperature) have shown that IAPP partitions preferentially into the liquid-disordered (l_d) lipid phase within minutes after the addition of the peptide, which is followed by subsequent membrane disintegration. Under such experimental conditions (5 μM IAPP, 25 ^oC), fibrillation of IAPP does not take place in the bulk solvent in this time range. To diminish energetic costs, initial incorporation of the peptides at the rim of the domains of the heterogeneous membrane, where the volume fluctuations are most prominent, would be most likely, leading to a favourable decrease of the associated line energy. The increase in membrane defects upon incorporation of the peptide will facilitate further peptide penetration, which leads to an increase in local peptide concentration in the membrane core region, thus allowing condensation of oligomeric particles and fibril growth. Insertion into the l_0 raft domains can be clearly ruled out. Predominantly circularly-shaped IAPP amyloid constructs are formed on the GUV templates, incorporating membrane lipids. The amyloid-lipid aggregates reach sizes of about 30 μm in diameter. Hence, this study clearly demonstrates the important ability of heterogeneous membranes in IAPP amyloid formation *in vitro* and most likely *in vivo* as well. Besides electroformation on Pt wires, a new chamber suitable for electroformation on ITO glass slides was developed, and the conditions for GUVs preparation were optimized, a major concern being the production of predominantly unilamellar species; spin-coating was found to favour this process.

Interestingly, membrane incorporation into IAPP fibrils was also observed in our cellular studies on INS-1E cells, fibrillar structures being typically 25-50 μm long and 1.5-4 μm thick. Our conclusions on model-raft systems and INS-1E cells are very well complemented by studies of Sparr et al. (*25*), who used different (non-raft) model lipid systems and a different cell line, and also observed lipid uptake into amyloid fibers, ruling out formation of discrete protein pores. All these results clearly point towards the incorporation of lipid upon IAPP fibril formation, with hydrophobic interactions being a major player in membrane-associated amyloid formation and thus

possibly in the onset of T2DM, once the barrier function of the cell membrane is lost. It may very well be that lipid-containing amyloid aggregates are universal structures of amyloid in cells.

Inhibitor design is a major concern in the field of amyloidogenic diseases. In this study, resveratrol, a small polyphenolic compound present in high amounts in grapes and red wine, has been shown to have pronounced effects on the survival of INS-1E cells treated with IAPP, by using the WST-1 assay, as well on the interaction of IAPP with model membrane systems, as revealed by imaging studies. An earlier role of resveratrol in cell survival has been attributed to its antioxidant activity. However, our inhibition results do not depend on the antioxidant activity. The imaging studies additionally indicate that the pronounced cytotoxicity of IAPP on INS-1E cells can be largely overcome by inhibition of IAPP fibrillation by the red wine compound resveratrol, which is able to arrest IAPP fibril formation at an early stage, possibly leading to the formation of non-toxic, "off-pathway" large oligomeric and amorphous structures. Since resveratrol is non-toxic to pancreatic β-cells, this natural polyphenol might have the potential to be developed as drug candidate against type II diabetes, and presumably towards other amyloidogenic diseases as well in the future. A model of interaction with IAPP and inhibition of IAPP fibril formation by resveratrol has also been proposed, and concomitant methods, i.e. AFM, ThT assay, ATR-FTIR, SAXS (*59, 148, 151*), have demonstrated a stoichiometric inhibition mechanism, pointing towards the fact that resveratrol acts by π-π stacking interactions with IAPP molecules.

To gain further insight into the mechanism of interaction between IAPP and cell membranes, and related cytotoxic effects, we isolated IAPP monomers, early, intermediate and late oligomers, protofibrils, as well as mature IAPP fibers, and carried out cytotoxicity tests with these compounds. It was thus revealed that it is the monomers and early oligomers which are cytotoxic, and much less the late protofibrils and mature fibrils. This once again points out the permeabilizing effect of IAPP oligomers to membranes, as suggested by model raft studies. The late protofibrils and mature fibrils seem to act through mechanical stress, only. Once the fiber has matured, interaction with the membrane (insertion into the membrane and further damage) is most likely prevented.

As the biological membranes are composed of a plethora of more or less fluid-like and raft-like domains, the strong membrane-disrupting potency of early IAPP oligomers in heterogeneous

membranes might be the reason for their cytotoxicity. Furthermore, extraction of lipids may be a common feature of amyloid formation *in vivo*, since extracellular amyloid deposits from a number of diseases have been found to be associated with cellular lipids. These findings would have to be taken into account in designing inhibitors for therapeutic approaches.

5. Zusammenfassung

In dieser Arbeit wurden verschiedene Aspekte der Aggregation des IAPPs, welche notwendig für das Verständniss von T2DM sind, untersucht. Der Fibrillenbildungsprozess wurde sowohl ohne als auch mit Lipid- und Zellmembranen analysiert. Zuerst wurde der Effekt von hohem hydrostatischen Druck auf die Bildung von IAPP-Fibrillen und im Vergleich dazu auf IAPP-Peptidfragmente untersucht, um die Art der Wechselwirkungen zu verstehen, welche für die fibrilläre Selbstorganisation auschlaggebend sind. Zudem wurde die Wechselwirkung von IAPP mit den bis jetzt vernachlässigten Modellraftmembranen, sowie mit Zellmembranen studiert. Die IAPP-Zytotoxizität und die Art der auf β-Zellen der Bauchspeicheldüse in Zellkultur toxisch wirkenden Spezies wurden ebenfalls analysiert. Auβerdem wurden mögliche Strategien entwickelt, um die Zytotoxizität und Fibrillenbildung von IAPP durch z.B. Resveratrol (ein Rotweinbestandteil) zu inhibieren. Mit Hilfe der erhaltenen Daten konnte hierfür ein Wechselwirkungs- und Inhibierungsmechanismus vorgeschlagen werden.

Unter Verwendung der Druckvariable konnten zusätzliche Details des Polymorphismus der Amyloide, sowie ihre Vorstufen und Übergänge zwischen diesen Zuständen aufgedeckt werden. Die Konformationsstabilität der verschiedenen Fibrillen unterscheidet sich, was möglicherweise auf Unterschiede in der Packungsdichte der Seitenketten in den Amyloidfibrillen zurückgeführt werden kann. Die Primärstruktur eines Polypeptids wurde im Laufe der Evolution so optimiert, dass sie sich in die native Form faltet. Normalerweise wird aber eine solch hohe Packungsdichte der Seitenketten in nichtnativen Fibrillenstrukturen nicht für alle Aminosäuren erreicht. Dies ist in Übereinstimmung mit der Beobachtung, dass Amlyoidfibrillen, die aus kleinen Peptiden oder Fragmenten von Amyloiden, wie z.B. dem hier untersuchten IAPP oder TTR, bestehen, dichter gepackt werden können. Im Vergleich zu IAPP zeigen die IAPP-Fragmente unter Druck eine höhere Stabilität, was auf die höhere Packungsdichte ihrer Peptidketten zurückzuführen ist. Eine Amyloidstruktur ohne optimale Packungsdichte neigt dazu, die Bildung von verschiedenen Isoformen zu begüngstigen, im Gegensatz zu der einzigartigen Faltung von funktionstüchtigen Proteinen. Eine durch Amyloidbildung verursachte Krankheit zeigt oft unterschiedliche Phänotypen und Inkubationszeiten. Das Auftretten dieser „Erregerstämme“ hängt vermutlich damit zusammen, dass Fibrillen, in Abhängigkeit der Umgebungsbedingungen, verschiedene strukturelle

Isoformen (Morphologien) annehmen können. IAPP scheint auch zu dieser Kategorie von Amyloidproteinen zu gehören. Ähnlich wie für globuläre Proteine, gibt es für reife Fibrillen einen Faltungstrichter („Aggregationstrichter“) mit zahlreichen möglichen Routen.

Die Wechselwirkungsstudien mit dem Modellraftlipidsystem DOPC : DPPC : Cholesterin 1 : 2 : 1 (eine bei Raumtemperatur l_d/l_o - Phasenkoexistenz zeigende Lipidmischung) zeigten, dass IAPP einige Minuten nach Peptidzugabe vorzugsweise in die l_d-Phase insertiert, was zur Membranzerstörung führt. Unter diesen experimentellen Bedingungen (5 µM IAPP, 25 ^oC) findet die Fibrillbildung des IAPPs in der reinen Phase (Bulkphase) in diesem Zeitraum nicht statt. Die anfängliche Einlagerung der Peptidmoleküle in die Phasengrenze der heterogenen Membran, wo die Volumenfluktuationen am größten sind, ist wohl am wahrscheinlichsten, da dies den Energieaufwand durch bevorzugte Verringerung der assozierten Grenzenergie reduziert. Die Zunahme an Membran-Defekten nach Peptideinlagerung erleichtert die weitere Einlagerung von Peptidmolekülen. Dies führt zu einem Anstieg der lokalen Peptidkonzentration im Membraninneren und damit zu einer Kondensation der Oligomere und zum Fibrillenwachstum. Eine Einlagerung in die l_o-Raftdomänen kann eindeutig ausgeschlossen werden. Es werden vorwiegend ringförmige IAPP-Amyloidstrukturen an den GUV-Templaten gebildet, welche Lipid in ihrem Inneren miteinschließen. Die Amyloid-Lipidaggregate erreichen Größen von ~ 30 µm im Durchmesser. Diese Studie zeigt daher sehr deutlich, dass heterogene Membranen eine groβe Rolle bei der IAPP-Amyloidbildung *in vitro* und wahrscheinlich auch *in vivo* spielen. Neben der Elektroformation an Pt-Drähten wurde auch eine neue Kammer für Elektroformation auf ITO-Objektträgern entwickelt. Ziel dabei war, hauptsächlich unilamellare Spezies zu produzieren; Spin-coating (Rotationsbeschichtung) favorisierte diesen Prozess.

Interessanterweise wurde auch eine Einlagerung des IAPPs in natürliche Membranen anhand von Zellstudien (INS-1E Zellen) beobachtet. Hierbei waren die fibrillären Strukturen typischerweise 25-50 µm lang und hatten einen Durchsmesser von 1.5-4 µm. Schlussfolgerungen aus den Untersuchungen an dem Modellraftsystem und den INS-1E-Zellen stehen im Einklang mit Studien von Sparr et al (*25*). Diese verwendeten andere (nicht-Raft) Modelllipidsysteme und eine andere Zelllinie, und fanden auch eine Membranaufnahme in den Amyloidfibrillen gefunden wurde, was gegen die Bildung der diskreten Protein-Poren in den Membranen spricht. Alle diese

Ergebnisse weisen auf die Aufnahme von Lipiden in IAPP-Amyloidfibrillen hin, wobei hydrophobe Wechselwirkungen eine wichtige Rolle spielen, und deshalb wahrscheinlich auch für das Auftreten des T2DMs von großer Bedeutung sind, wenn die Barrierefunktion der Zellmembran verloren geht. Es kann daher sehr wohl der Fall sein, dass Lipid-Amyloid-Aggregate Universalstrukturen bei der Amyloidbildung in natürlicher Zellumgebung sind.

Die Entwicklung von Inhibitoren ist ein wichtiges Anliegen auf dem Gebiet der Amyloidforschung. In dieser Arbeit wurde durch Anwendung des WST-1 Assays und mit Hilfe von Visualisierungsstudien beobachtet, dass Resveratrol, ein kleines Polyphenol, das in grßen Mengen in Weintrauben und Rotwein zu finden ist, eine ausgeprägte Wirkung auf die Überlebensrate der IAPP-behandelten INS-1E Zellen hat. Zuvor wurde die Rolle des Resveratrols für das Überleben der Zellen in Zellkultur auf seine antioxidative Aktivität zurückgeführt. Die hier durchgeführten Inhibierungsstudien stehen jedoch in keinem Zusammenhang mit den antioxidativen Eingeschaften. Die Mikroskopiestudien zeigten außerdem, dass die ausgeprägte Zytotoxizität des IAPPs auf INS-1E Zellen durch die Inhibierung der IAPP-Fibrilbildung in Anwesenheit von Resveratrol unterdrückt wird. Resveratrol kann die Fibrilbildung des IAPPs frühzeitig unterbinden, wobei sich sehr wahrscheinlich große „off-pathway“ - Oligomere und amorphe Aggregate bilden. Da Resveratrol selbst keine Toxizität auf β-Zellen aufweist, könnte dieses natürliche Polyphenol in Zukunft als Medikament gegen T2DM und sehr wahrscheinlich auch gegen andere Amyloidkrankheiten weiter entwickelt werden. Ein Mechanismus der Wechselwirkung und Inhibierung der IAPP-Fibrilbildung durch Resveratrol konnte vorgeschlagen werden, und ergänzende Methoden (AFM, ThT Assay, ATR-FTIR, SAXS) (*59, 148, 151*) zeigten einen stöchiometrischen Inhibierungsmechanismus. Dieser lässt sich wahrscheinlich auf die Inhibierung der Wechselwirkung zwischen unterschiedlichen IAPP Molekülen durch π-π-Bindung des Resveratrols mit dem IAPP zurückführen.

Um einen weiteren Einblick in den Mechanismus der IAPP-Zellmembran-Wechselwirkung sowie deren assoziierte zytotoxische Effekte zu gewinnen, wurden IAPP Monomere, frühe, mittlere und größere Oligomere, Protofibrillen und reife Fibrillen isoliert und hinsichtlich ihrer Zytotoxizität untersucht. Es wurde gefunden, dass die Monomere und kleinen Oligomere sehr toxisch auf INS-1E Zellen wirken, im Gegensatz zu den größeren Protofibrillen

und reifen Fibrillen. Dies belegt nochmals, dass die IAPP Oligomere Hauptursache für die Zerstörung der Membran sind. Die großen Proto- und reifen Fibrillen scheinen relativ zu den Monomeren und Oligomeren nur durch mechanische Beanspruchung einen minimalen Einfluss auf die Integrität der INS-E Zellen zu haben. Insofern kann die Wechselwirkung von reifen Fibrillen mit der Membran (Einlagerung in die Membran und Membranzerstörung) weitgehend ausgeschlossen werden.

Da biologische Membranen aus einer Fülle von mehr oder weniger fluiden und Raft-ähnlichen Domäne bestehen, könnte die hohe membranzerstörende Potenz der kleinen IAPP-Oligomere auf heterogene Membranen auch ein Grund für die beobachtete Zytotoxizität sein. Weiterhin könnte die Rekrutierung von Lipiden aus der Membran eine allgemeine Erscheinung der Amyloidbildung *in vitro* sein, da extrazelluläre Amyloid-Ablagerungen schon bei mehrere Krankheiten gefunden wurden. Diese Befunde sollten dann auch in der Zukunft bei der Inhibitor-Entwicklung für therapeutische Anwendungen Berücksichtigung finden.

6. Appendix

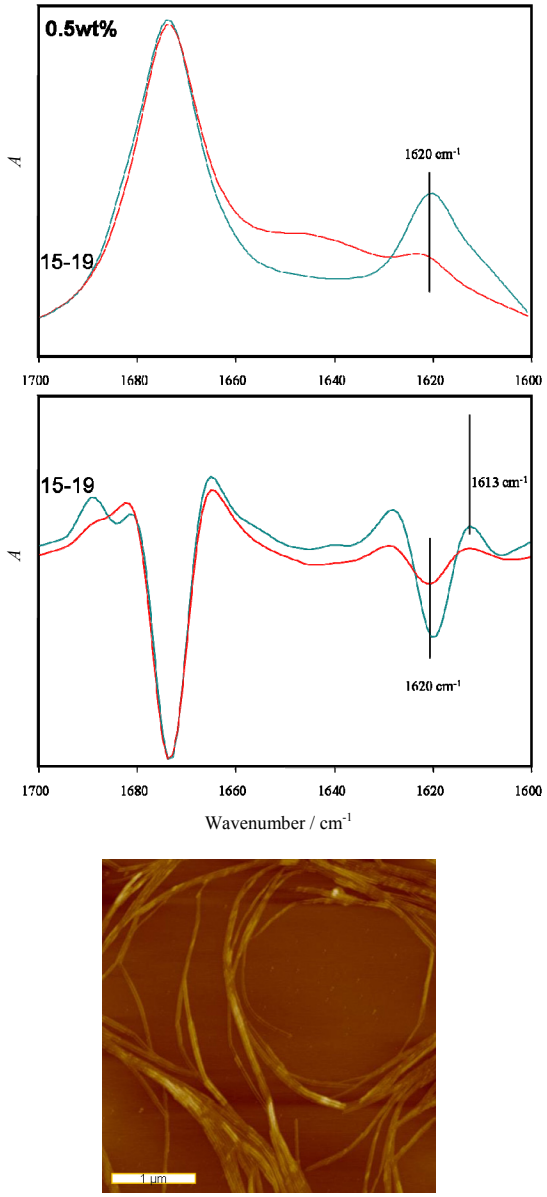

Figure A CH_3-FLVHS-CH_3 (IAPP 15-19 amino-acid region, 0.5 wt%) fibril formation monitored by FT-IR spectroscopy (upper panel: primary spectra, lower panel: second derivative spectra, red curves: time zero, green curves: after 20 h) and the morphology of mature fibers after 20 h incubation in 50 mM deuterated natrium phosphate buffer, pH 7.4, at 37 °C. The peak at 1620 cm^{-1} and the shoulder at 1613 cm^{-1} indicate the presence of β-strands, typical of fibrillar morphologies, in line with the AFM results, where fibers of several µm length, with pronounced twisting and a tendency for circular shapes, were detected. At lower concentrations, the peptide did not form fibers under the same experimental conditions.

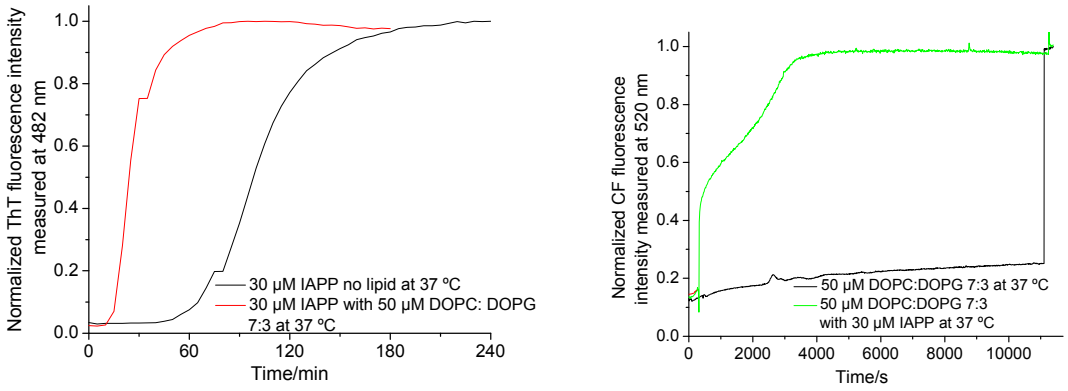

Figure B The interaction of 30 μM IAPP with LUVs (100 nm diameter) made of DOPC:DOPG 7:3, in 10 mM HEPES, 150 mM NaCl, pH 7.4. The ThT aggregation kinetics, with and without membrane, is displayed in the left panel, and the corresponding CF leakage curves, with and without peptide, in the right panel, respectively. The presence of the negatively charged membrane has an accelerating effect on IAPP fibril formation, and IAPP induces 100 % leakage of CF-filled LUVs within 1 h after peptide addition. Full release of the otherwise self-quenched CF, encapsulated in LUVs (100 mM CF), is achieved by treatment of LUVs samples with the detergent Triton-X 100. Within 1 h from the initial exposure (IAPP and negatively charged LUVs), both IAPP fibrillation (ThT assay, left) and liposomal leakage (CF assay, right) are complete, suggesting that the lipid barrier destruction and IAPP fibrillation are concomitant processes.

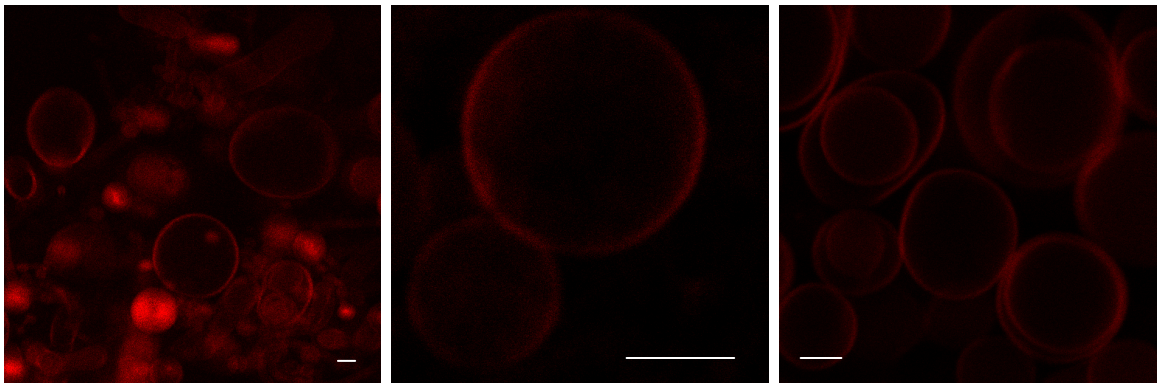

Figure C DOPC Rhodamine-DHPE labelled GUVs, electroformed in water on ITO slides (left), in water, at room temperature. GUVs were prepared under various conditions: (left) no spin-coating, 2.5 μL 0.2 mg/mL lipid, electroformation for 90 min at 3V and 10 Hz; (middle) spin-coating (800 rpm / 60 s), 200μL 4mg/mL lipid, electroformation: for 180 min at 3V and 10Hz; (right) spin-coating (800 rpm / 60 s), 20μL 4mg/mL lipid, electroformation for 100 min at 3V and 10Hz. Spin-coating ensures a homogeneous distribution of the lipid film on the ITO slide, thereby promoting the formation of mainly vesicular, predominantly unilamellar, structures. A higher lipid concentration and volume is needed in the former case. The scale bar represents 10 μm.

References

(1) Sunde, M., Serpell, L. C., Bartlam, M., Fraser, P. E., Pepys, M. B., and Blake, C. C. (1997) Common core structure of amyloid fibrils by synchrotron X-ray diffraction. *J Mol Biol 273*, 729-39.

(2) Glenner, G. G., and Terry, W. D. (1974) Characterization of amyloid. *Annu Rev Med 25*, 131-5.

(3) Kelly, J. W., and Balch, W. E. (2003) Amyloid as a natural product. *J Cell Biol 161*, 461-2.

(4) Stefani, M., and Dobson, C. M. (2003) Protein aggregation and aggregate toxicity: new insights into protein folding, misfolding diseases and biological evolution. *J Mol Med 81*, 678-99.

(5) Dobson, C. M. (1999) Protein misfolding, evolution and disease. *Trends Biochem Sci 24*, 329-32.

(6) Chiti, F., Webster, P., Taddei, N., Clark, A., Stefani, M., Ramponi, G., and Dobson, C. M. (1999) Designing conditions for in vitro formation of amyloid protofilaments and fibrils. *Proc Natl Acad Sci U S A 96*, 3590-4.

(7) Grudzielanek, S., Smirnovas, V., and Winter, R. (2007) The effects of various membrane physical-chemical properties on the aggregation kinetics of insulin. *Chem Phys Lipids 149*, 28-39.

(8) Grudzielanek, S., Smirnovas, V., and Winter, R. (2006) Solvation-assisted pressure tuning of insulin fibrillation: from novel aggregation pathways to biotechnological applications. *J Mol Biol 356*, 497-509.

(9) Jansen, R., Dzwolak, W., and Winter, R. (2005) Amyloidogenic self-assembly of insulin aggregates probed by high resolution atomic force microscopy. *Biophys J 88*, 1344-53.

(10) Barral, J. M., Broadley, S. A., Schaffar, G., and Hartl, F. U. (2004) Roles of molecular chaperones in protein misfolding diseases. *Semin Cell Dev Biol 15*, 17-29.

(11) Chiti, F., and Dobson, C. M. (2006) Protein misfolding, functional amyloid, and human disease. *Annu Rev Biochem 75*, 333-66.

(12) Dobson, C. M. (2006) Protein aggregation and its consequences for human disease. *Protein Pept Lett 13*, 219-27.

(13) Jahn, T. R., and Radford, S. E. (2005) The Yin and Yang of protein folding. *FEBS J 272*, 5962-70.

(14) Jarrett, J. T., and Lansbury, P. T., Jr. (1992) Amyloid fibril formation requires a chemically discriminating nucleation event: studies of an amyloidogenic sequence from the bacterial protein OsmB. *Biochemistry 31*, 12345-52.

(15) Tomski, S. J., and Murphy, R. M. (1992) Kinetics of aggregation of synthetic beta-amyloid peptide. *Arch Biochem Biophys 294*, 630-8.

(16) Jarrett, J. T., Berger, E. P., and Lansbury, P. T., Jr. (1993) The carboxy terminus of the beta amyloid protein is critical for the seeding of amyloid formation: implications for the pathogenesis of Alzheimer's disease. *Biochemistry 32*, 4693-7.

(17) Jarrett, J. T., and Lansbury, P. T., Jr. (1993) Seeding "one-dimensional crystallization" of amyloid: a pathogenic mechanism in Alzheimer's disease and scrapie? *Cell 73*, 1055-8.

(18) Kelly, J. W. (2000) Mechanisms of amyloidogenesis. *Nat Struct Biol 7*, 824-6.

(19) Gellermann, G. P., Appel, T. R., Tannert, A., Radestock, A., Hortschansky, P., Schroeckh, V., Leisner, C., Lutkepohl, T., Shtrasburg, S., Rocken, C., Pras, M., Linke, R. P., Diekmann, S., and Fandrich, M. (2005) Raft lipids as common components of human extracellular amyloid fibrils. *Proc Natl Acad Sci U S A 102*, 6297-302.
(20) Simons, K., and Ehehalt, R. (2002) Cholesterol, lipid rafts, and disease. *J Clin Invest 110*, 597-603.
(21) Gorbenko, G. P., and Kinnunen, P. K. (2006) The role of lipid-protein interactions in amyloid-type protein fibril formation. *Chem Phys Lipids 141*, 72-82.
(22) Kakio, A., Nishimoto, S., Kozutsumi, Y., and Matsuzaki, K. (2003) Formation of a membrane-active form of amyloid beta-protein in raft-like model membranes. *Biochem Biophys Res Commun 303*, 514-8.
(23) Arispe, N., Pollard, H. B., and Rojas, E. (1994) beta-Amyloid Ca(2+)-channel hypothesis for neuronal death in Alzheimer disease. *Mol Cell Biochem 140*, 119-25.
(24) Stefani, M. (2004) Protein misfolding and aggregation: new examples in medicine and biology of the dark side of the protein world. *Biochim Biophys Acta 1739*, 5-25.
(25) Sparr, E., Engel, M. F., Sakharov, D. V., Sprong, M., Jacobs, J., de Kruijff, B., Hoppener, J. W., and Killian, J. A. (2004) Islet amyloid polypeptide-induced membrane leakage involves uptake of lipids by forming amyloid fibers. *FEBS Lett 577*, 117-20.
(26) Mirzabekov, T. A., Lin, M. C., and Kagan, B. L. (1996) Pore formation by the cytotoxic islet amyloid peptide amylin. *J Biol Chem 271*, 1988-92.
(27) Jeworrek, C., Hollmann, O., Steitz, R., Winter, R., and Czeslik, C. (2009) Interaction of IAPP and insulin with model interfaces studied using neutron reflectometry. *Biophys J 96*, 1115-23.
(28) Sharp, J. S., Forrest, J. A., and Jones, R. A. (2002) Surface denaturation and amyloid fibril formation of insulin at model lipid-water interfaces. *Biochemistry 41*, 15810-9.
(29) Westermark, P., Wilander, E., and Johnson, K. H. (1987) Islet amyloid polypeptide. *Lancet 2*, 623.
(30) Cooper, M. E., and Wookey, P. J. (1997) Amylin-its role in the kidney. *Nephrol Dial Transplant 12*, 8-10.
(31) Cooper, G. J., and Tse, C. A. (1996) Amylin, amyloid and age-related disease. *Drugs Aging 9*, 202-12.
(32) Westermark, G. T., Falkmer, S., Steiner, D. F., Chan, S. J., Engstrom, U., and Westermark, P. (2002) Islet amyloid polypeptide is expressed in the pancreatic islet parenchyma of the teleostean fish, Myoxocephalus (cottus) scorpius. *Comp Biochem Physiol B Biochem Mol Biol 133*, 119-25.
(33) Westermark, P., Wernstedt, C., Wilander, E., and Sletten, K. (1986) A novel peptide in the calcitonin gene related peptide family as an amyloid fibril protein in the endocrine pancreas. *Biochem Biophys Res Commun 140*, 827-31.
(34) Cooper, G. J. (1994) Amylin compared with calcitonin gene-related peptide: structure, biology, and relevance to metabolic disease. *Endocr Rev 15*, 163-201.
(35) Jaikaran, E. T., and Clark, A. (2001) Islet amyloid and type 2 diabetes: from molecular misfolding to islet pathophysiology. *Biochim Biophys Acta 1537*, 179-203.

(36) Westermark, P., Wernstedt, C., O'Brien, T. D., Hayden, D. W., and Johnson, K. H. (1987) Islet amyloid in type 2 human diabetes mellitus and adult diabetic cats contains a novel putative polypeptide hormone. *Am J Pathol 127*, 414-7.
(37) Knight, J. D., and Miranker, A. D. (2004) Phospholipid catalysis of diabetic amyloid assembly. *J Mol Biol 341*, 1175-87.
(38) Cluck, M. W., Chan, C. Y., and Adrian, T. E. (2005) The regulation of amylin and insulin gene expression and secretion. *Pancreas 30*, 1-14.
(39) Kajava, A. V., Aebi, U., and Steven, A. C. (2005) The parallel superpleated beta-structure as a model for amyloid fibrils of human amylin. *J Mol Biol 348*, 247-52.
(40) Westermark, G., Westermark, P., Eizirik, D. L., Hellerstrom, C., Fox, N., Steiner, D. F., and Andersson, A. (1999) Differences in amyloid deposition in islets of transgenic mice expressing human islet amyloid polypeptide versus human islets implanted into nude mice. *Metabolism 48*, 448-54.
(41) Westermark, G. T., Gebre-Medhin, S., Steiner, D. F., and Westermark, P. (2000) Islet amyloid development in a mouse strain lacking endogenous islet amyloid polypeptide (IAPP) but expressing human IAPP. *Mol Med 6*, 998-1007.
(42) Westermark, G. T., Steiner, D. F., Gebre-Medhin, S., Engstrom, U., and Westermark, P. (2000) Pro islet amyloid polypeptide (ProIAPP) immunoreactivity in the islets of Langerhans. *Ups J Med Sci 105*, 97-106.
(43) Kayed, R., Bernhagen, J., Greenfield, N., Sweimeh, K., Brunner, H., Voelter, W., and Kapurniotu, A. (1999) Conformational transitions of islet amyloid polypeptide (IAPP) in amyloid formation in vitro. *J Mol Biol 287*, 781-96.
(44) Padrick, S. B., and Miranker, A. D. (2002) Islet amyloid: phase partitioning and secondary nucleation are central to the mechanism of fibrillogenesis. *Biochemistry 41*, 4694-703.
(45) Green, J. D., Goldsbury, C., Kistler, J., Cooper, G. J., and Aebi, U. (2004) Human amylin oligomer growth and fibril elongation define two distinct phases in amyloid formation. *J Biol Chem 279*, 12206-12.
(46) Green, J. D., Kreplak, L., Goldsbury, C., Li Blatter, X., Stolz, M., Cooper, G. S., Seelig, A., Kistler, J., and Aebi, U. (2004) Atomic force microscopy reveals defects within mica supported lipid bilayers induced by the amyloidogenic human amylin peptide. *J Mol Biol 342*, 877-87.
(47) Goldsbury, C., Goldie, K., Pellaud, J., Seelig, J., Frey, P., Muller, S. A., Kistler, J., Cooper, G. J., and Aebi, U. (2000) Amyloid fibril formation from full-length and fragments of amylin. *J Struct Biol 130*, 352-62.
(48) Tenidis, K., Waldner, M., Bernhagen, J., Fischle, W., Bergmann, M., Weber, M., Merkle, M. L., Voelter, W., Brunner, H., and Kapurniotu, A. (2000) Identification of a penta- and hexapeptide of islet amyloid polypeptide (IAPP) with amyloidogenic and cytotoxic properties. *J Mol Biol 295*, 1055-71.
(49) Nilsson, M. R., and Raleigh, D. P. (1999) Analysis of amylin cleavage products provides new insights into the amyloidogenic region of human amylin. *J Mol Biol 294*, 1375-85.
(50) Jaikaran, E. T., Higham, C. E., Serpell, L. C., Zurdo, J., Gross, M., Clark, A., and Fraser, P. E. (2001) Identification of a novel human islet amyloid polypeptide beta-sheet domain and factors influencing fibrillogenesis. *J Mol Biol 308*, 515-25.

(51) Azriel, R., and Gazit, E. (2001) Analysis of the minimal amyloid-forming fragment of the islet amyloid polypeptide. An experimental support for the key role of the phenylalanine residue in amyloid formation. *J Biol Chem 276*, 34156-61.
(52) Lopes, D. H., Meister, A., Gohlke, A., Hauser, A., Blume, A., and Winter, R. (2007) Mechanism of islet amyloid polypeptide fibrillation at lipid interfaces studied by infrared reflection absorption spectroscopy. *Biophys J 93*, 3132-41.
(53) Engel, M. F., Yigittop, H., Elgersma, R. C., Rijkers, D. T., Liskamp, R. M., de Kruijff, B., Hoppener, J. W., and Antoinette Killian, J. (2006) Islet amyloid polypeptide inserts into phospholipid monolayers as monomer. *J Mol Biol 356*, 783-9.
(54) Singh, G., Brovchenko, I., Oleinikova, A., and Winter, R. (2008) Peptide aggregation in finite systems. *Biophys J 95*, 3208-21.
(55) Knight, J. D., Hebda, J. A., and Miranker, A. D. (2006) Conserved and cooperative assembly of membrane-bound alpha-helical states of islet amyloid polypeptide. *Biochemistry 45*, 9496-508.
(56) Janson, J., Ashley, R. H., Harrison, D., McIntyre, S., and Butler, P. C. (1999) The mechanism of islet amyloid polypeptide toxicity is membrane disruption by intermediate-sized toxic amyloid particles. *Diabetes 48*, 491-8.
(57) Kurganov, B., Doh, M., and Arispe, N. (2004) Aggregation of liposomes induced by the toxic peptides Alzheimer's Abetas, human amylin and prion (106-126): facilitation by membrane-bound GM1 ganglioside. *Peptides 25*, 217-32.
(58) Brender, J. R., Lee, E. L., Cavitt, M. A., Gafni, A., Steel, D. G., and Ramamoorthy, A. (2008) Amyloid fiber formation and membrane disruption are separate processes localized in two distinct regions of IAPP, the type-2-diabetes-related peptide. *J Am Chem Soc 130*, 6424-9.
(59) Evers, F., Jeworrek, C., Tiemeyer, S., Weise, K., Sellin, D., Paulus, M., Struth, B., Tolan, M., and Winter, R. (2009) Elucidating the mechanism of lipid membrane-induced IAPP fibrillogenesis and its inhibition by the red wine compound resveratrol: a synchrotron X-ray reflectivity study. *J Am Chem Soc 131*, 9516-21.
(60) Jayasinghe, S. A., and Langen, R. (2005) Lipid membranes modulate the structure of islet amyloid polypeptide. *Biochemistry 44*, 12113-9.
(61) Cho, W. J., Jena, B. P., and Jeremic, A. M. (2008) Nano-scale imaging and dynamics of amylin-membrane interactions and its implication in type II diabetes mellitus. *Methods Cell Biol 90*, 267-86.
(62) Ji, S. R., Wu, Y., and Sui, S. F. (2002) Cholesterol is an important factor affecting the membrane insertion of beta-amyloid peptide (A beta 1-40), which may potentially inhibit the fibril formation, *J Biol Chem 277*, 6273-9.
(63) Wolozin, B. (2001) A fluid connection: cholesterol and Abeta. *Proc Natl Acad Sci U S A 98*, 5371-3.
(64) McLaurin, J., Darabie, A. A., and Morrison, M. R. (2003) Cholesterol, a modulator of membrane-associated Abeta-fibrillogenesis. *Pharmacopsychiatry 36 Suppl 2*, 130-5.
(65) Kawarabayashi, T., Shoji, M., Younkin, L.H., Wenlang, L., Dickson, D.W., Murakami, T., Matsubara, E., Abe, K., Ashe, K.H. and Youkin, S.G. (2004) Dimeric amyloid β protein

rapidly accumulates in lipid rafts followed by apolipoprotein E and phosphorylated tau accumulation in the Tg2576 mouse model of Alzheimer's disease. *J Neurosci 24*, 3801-9.
(66) Raffai, R. L., and Weisgraber, K. H. (2003) Cholesterol: from heart attacks to Alzheimer's disease. *J Lipid Res 44*, 1423-30.
(67) Ehehalt, R., Keller, P., Haass, C., Thiele, C., and Simons, K. (2003) Amyloidogenic processing of the Alzheimer beta-amyloid precursor protein depends on lipid rafts. *J Cell Biol 160*, 113-23.
(68) Jayasinghe, S. A., and Langen, R. (2004) Identifying structural features of fibrillar islet amyloid polypeptide using site-directed spin labeling. *J Biol Chem 279*, 48420-5.
(69) Anguiano, M., Nowak, R. J., and Lansbury, P. T., Jr. (2002) Protofibrillar islet amyloid polypeptide permeabilizes synthetic vesicles by a pore-like mechanism that may be relevant to type II diabetes. *Biochemistry 41*, 11338-43.
(70) Hebda, J. A., and Miranker, A. D. (2009) The interplay of catalysis and toxicity by amyloid intermediates on lipid bilayers: insights from type II diabetes. *Annu Rev Biophys 38*, 125-52.
(71) Bulic, B., Pickhardt, M., Khlistunova, I., Biernat, J., Mandelkow, E. M., Mandelkow, E., and Waldmann, H. (2007) Rhodanine-based tau aggregation inhibitors in cell models of tauopathy. *Angew Chem Int Ed Engl 46*, 9215-9.
(72) Mishra, R., Bulic, B., Sellin, D., Jha, S., Waldmann, H., and Winter, R. (2008) Small-molecule inhibitors of islet amyloid polypeptide fibril formation. *Angew Chem Int Ed Engl 47*, 4679-82.
(73) Taniguchi, T., Sumida, M., Hiraoka, S., Tomoo, K., Kakehi, T., Minoura, K., Sugiyama, S., Inaka, K., Ishida, T., Saito, N., and Tanaka, C. (2005) Effects of different anti-tau antibodies on tau fibrillogenesis: RTA-1 and RTA-2 counteract tau aggregation. *FEBS Lett 579*, 1399-404.
(74) Porat, Y., Abramowitz, A., and Gazit, E. (2006) Inhibition of amyloid fibril formation by polyphenols: structural similarity and aromatic interactions as a common inhibition mechanism. *Chem Biol Drug Des 67*, 27-37.
(75) Ehrnhoefer, D. E., Bieschke, J., Boeddrich, A., Herbst, M., Masino, L., Lurz, R., Engemann, S., Pastore, A., and Wanker, E. E. (2008) EGCG redirects amyloidogenic polypeptides into unstructured, off-pathway oligomers. *Nat Struct Mol Biol 15*, 558-66.
(76) Ehrnhoefer, D. E., Duennwald, M., Markovic, P., Wacker, J. L., Engemann, S., Roark, M., Legleiter, J., Marsh, J. L., Thompson, L. M., Lindquist, S., Muchowski, P. J., and Wanker, E. E. (2006) Green tea (-)-epigallocatechin-gallate modulates early events in huntingtin misfolding and reduces toxicity in Huntington's disease models. *Hum Mol Genet 15*, 2743-51.
(77) Riviere, C., Richard, T., Quentin, L., Krisa, S., Merillon, J. M., and Monti, J. P. (2007) Inhibitory activity of stilbenes on Alzheimer's beta-amyloid fibrils in vitro. *Bioorg Med Chem 15*, 1160-7.
(78) Marambaud, P., Zhao, H., and Davies, P. (2005) Resveratrol promotes clearance of Alzheimer's disease amyloid-beta peptides. *J Biol Chem 280*, 37377-82.
(79) Yeagle, P. L. (2004) *The structure of biological membranes*, 2nd ed., CRC Press.
(80) Mouritsen, O. (2005) *Life-as a matter of fat. The emerging science of lipidomics*, Springer.

(81) Singer, S. J., and Nicolson, G. L. (1972) The fluid mosaic model of the structure of cell membranes. *Science 175*, 720-731.
(82) Simons, K., and Ikonen, E. (1997) Functional rafts in cell membranes. *Nature 387*, 569-72.
(83) Parton, R. G., and Richards, A. A. (2003) Lipid rafts and caveolae as portals for endocytosis: new insights and common mechanisms. *Traffic 4*, 724-38.
(84) Helms, J. B., and Zurzolo, C. (2004) Lipids as targeting signals: lipid rafts and intracellular trafficking. *Traffic 5*, 247-54.
(85) Prior, I. A., Muncke, C., Parton, R. G., and Hancock, J. F. (2003) Direct visualization of Ras proteins in spatially distinct cell surface microdomains. *J Cell Biol 160*, 165-70.
(86) Lai, E. C. (2003) Lipid rafts make for slippery platforms. *J Cell Biol 162*, 365-70.
(87) Bagatolli, L. A. (2006) To see or not to see: lateral organization of biological membranes and fluorescence microscopy. *Biochim Biophys Acta 1758*, 1541-56.
(88) Alberts, B., Bray, D., Lewis, J., Ralf, M., Roberts, K., and Watson, J. D. (2002) *Molecular Biology of the Cell*, 4th ed., Garland Publishing
(89) Findley, H. E., and Booth, P. J. (2006) The Biological Significance of Lipid-Protein Interactions. *J Phys: Condens Matter 18*, 1281-1291.
(90) Lee, A. G. (2004) How lipids affect the activities of integral membrane proteins. *Biochim Biophys Acta 1666*, 62-87.
(91) Ches, O., and Mulet, X. (2006) Physical coupling between lipids and proteins: a paradigm for cellular control. *Signal Transduction 6*, 112-132.
(92) New, R. (1990) *Liposomes - a practical approach*, Oxford University Press.
(93) Ulrich, A. S. (2002) Biophysical aspects of using liposomes as delivery vehicles. *Biosci Rep 22*, 129-50.
(94) Heerklotz, H., Tsamaloukas, A., Kita-Tokarczyk, K., Strunz, P., and Gutberlet, T. (2004) Structural, volumetric, and thermodynamic characterization of a micellar sphere-to-rod transition. *J Am Chem Soc 126*, 16544-52.
(95) Munro, S. (2003) Cell biology: earthworms and lipid couriers. *Nature 426*, 775-6.
(96) Munro, S. (2003) Lipid rafts: elusive or illusive? *Cell 115*, 377-88.
(97) Mouritsen, O. G. (1991) Theoretical models of phospholipid phase transitions. *Chem Phys Lipids 57*, 179-94.
(98) Needham, D., and Nunn, R. S. (1990) Elastic deformation and failure of lipid bilayer membranes containing cholesterol. *Biophys J 58*, 997-1009.
(99) Bloom, M., Evans, E., and Mouritsen, O. G. (1991) Physical properties of the fluid lipid-bilayer component of cell membranes: a perspective. *Q Rev Biophys 24*, 293-397.
(100) Li, X. M., Momsen, M. M., Smaby, J. M., Brockman, H. L., and Brown, R. E. (2001) Cholesterol decreases the interfacial elasticity and detergent solubility of sphingomyelins. *Biochemistry 40*, 5954-63.
(101) Ramstedt, B., and Slotte, J. P. (2002) Membrane properties of sphingomyelins. *FEBS Lett 531*, 33-7.
(102) Veatch, S. L., and Keller, S. L. (2002) Organization in lipid membranes containing cholesterol. *Phys Rev Lett 89*, 268101.
(103) Veatch, S. L., and Keller, S. L. (2003) Separation of liquid phases in giant vesicles of ternary mixtures of phospholipids and cholesterol. *Biophys J 85*, 3074-83.

(104) Veatch, S. L., and Keller, S. L. (2003) A closer look at the canonical 'Raft Mixture' in model membrane studies. *Biophys J 84*, 725-6.
(105) Asfari, M., Janjic, D., Meda, P., Li, G., Halban, P. A., and Wollheim, C. B. (1992) Establishment of 2-mercaptoethanol-dependent differentiated insulin-secreting cell lines. *Endocrinology 130*, 167-78.
(106) Praz, G. A., Halban, P. A., Wollheim, C. B., Blondel, B., Strauss, A. J., and Renold, A. E. (1983) Regulation of immunoreactive-insulin release from a rat cell line (RINm5F). *Biochem J 210*, 345-52.
(107) Merglen, A., Theander, S., Rubi, B., Chaffard, G., Wollheim, C. B., and Maechler, P. (2004) Glucose sensitivity and metabolism-secretion coupling studied during two-year continuous culture in INS-1E insulinoma cells. *Endocrinology 145*, 667-78.
(108) Reis, O., Winter, R., and Zerda, T. W. (1996) The effect of high external pressure on DPPC-cholesterol multilamellar vesicles: a pressure-tuning Fourier transform infrared spectroscopy study. *Biochim Biophys Acta 1279*, 5-16.
(109) Auger, M., Jarrell, H. C., Smith, I. C., Wong, P. T., Siminovitch, D. J., and Mantsch, H. H. (1987) Pressure-induced exclusion of a local anesthetic from model and nerve membranes. *Biochemistry 26*, 8513-6.
(110) Gray, C., Tatulian, S. A., Wharton, S. A., and Tamm, L. K. (1996) Effect of the N-terminal glycine on the secondary structure, orientation, and interaction of the influenza hemagglutinin fusion peptide with lipid bilayers. *Biophys J 70*, 2275-86.
(111) Roland Winter, D. L., Stefan Grudzielanek, and Karsten Vogtt. (2007) Towards an understanding of the temperature / pressure configurational and free-energy landscape of biomolecules. *J Non-Equilib Thermodyn 32*, 41-97.
(112) Herberhold, H., Royer, C. A., and Winter, R. (2004) Effects of chaotropic and kosmotropic cosolvents on the pressure-induced unfolding and denaturation of proteins: an FT-IR study on staphylococcal nuclease. *Biochemistry 43*, 3336-45.
(113) Panick, G., Malessa, R., and Winter, R. (1999) Differences between the pressure- and temperature-induced denaturation and aggregation of beta-lactoglobulin A, B, and AB monitored by FT-IR spectroscopy and small-angle X-ray scattering. *Biochemistry 38*, 6512-9.
(114) Panick, G., Vidugiris, G. J., Malessa, R., Rapp, G., Winter, R., and Royer, C. A. (1999) Exploring the temperature-pressure phase diagram of staphylococcal nuclease. *Biochemistry 38*, 4157-64.
(115) Dzwolak, W., Smirnovas, V., Jansen, R., and Winter, R. (2004) Insulin forms amyloid in a strain-dependent manner: an FT-IR spectroscopic study. *Protein Sci 13*, 1927-32.
(116) Haris, P. I., and Chapman, D. (1995) The conformational analysis of peptides using Fourier transform IR spectroscopy. *Biopolymers 37*, 251-63.
(117) Haris, P. I., Chapman, D., and Benga, G. (1995) A Fourier-transform infrared spectroscopic investigation of the hydrogen-deuterium exchange and secondary structure of the 28-kDa channel-forming integral membrane protein (CHIP28). *Eur J Biochem 233*, 659-64.
(118) Wolkers, W. F., Haris, P. I., Pistorius, A. M., Chapman, D., and Hemminga, M. A. (1995) FT-IR spectroscopy of the major coat protein of M13 and Pf1 in the phage and reconstituted into phospholipid systems. *Biochemistry 34*, 7825-33.

(119) Byler, D. M., and Susi, H. (1986) Examination of the secondary structure of proteins by deconvolved FTIR spectra. *Biopolymers 25*, 469-87.
(120) Susi, H., and Byler, D. M. (1986) Resolution-enhanced Fourier transform infrared spectroscopy of enzymes. *Methods Enzymol 130*, 290-311.
(121) Susi, H., Byler, D. M., and Purcell, J. M. (1985) Estimation of beta-structure content of proteins by means of deconvolved FTIR spectra. *J Biochem Biophys Methods 11*, 235-40.
(122) Jansen, R., Grudzielanek, S., Dzwolak, W., and Winter, R. (2004) High pressure promotes circularly shaped insulin amyloid. *J Mol Biol 338*, 203-6.
(123) Dzwolak, W., Grudzielanek, S., Smirnovas, V., Ravindra, R., Nicolini, C., Jansen, R., Loksztejn, A., Porowski, S., and Winter, R. (2005) Ethanol-perturbed amyloidogenic self-assembly of insulin: looking for origins of amyloid strains. *Biochemistry 44*, 8948-58.
(124) Radovan, D., Smirnovas, V., and Winter, R. (2008) Effect of pressure on islet amyloid polypeptide aggregation: revealing the polymorphic nature of the fibrillation process. *Biochemistry 47*, 6352-60.
(125) Foguel, D., and Silva, J. L. (2004) New insights into the mechanisms of protein misfolding and aggregation in amyloidogenic diseases derived from pressure studies. *Biochemistry 43*, 11361-70.
(126) Silva, J. L., Cordeiro, Y., and Foguel, D. (2006) Protein folding and aggregation: two sides of the same coin in the condensation of proteins revealed by pressure studies. *Biochim Biophys Acta 1764*, 443-51.
(127) Heremans, K., and Smeller, L. (1998) Protein structure and dynamics at high pressure. *Biochim Biophys Acta 1386*, 353-70.
(128) Cordeiro, Y., Kraineva, J., Ravindra, R., Lima, L. M., Gomes, M. P., Foguel, D., Winter, R., and Silva, J. L. (2004) Hydration and packing effects on prion folding and beta-sheet conversion. High pressure spectroscopy and pressure perturbation calorimetry studies. *J Biol Chem 279*, 32354-9.
(129) Herberhold, H., Marchal, S., Lange, R., Scheyhing, C. H., Vogel, R. F., and Winter, R. (2003) Characterization of the pressure-induced intermediate and unfolded state of red-shifted green fluorescent protein--a static and kinetic FTIR, UV/VIS and fluorescence spectroscopy study. *J Mol Biol 330*, 1153-64.
(130) Hummer, G., Garde, S., Garcia, A. E., Paulaitis, M. E., and Pratt, L. R. (1998) The pressure dependence of hydrophobic interactions is consistent with the observed pressure denaturation of proteins. *Proc Natl Acad Sci U S A 95*, 1552-5.
(131) Paladini, A. A., Jr., and Weber, G. (1981) Pressure-induced reversible dissociation of enolase. *Biochemistry 20*, 2587-93.
(132) Valeur, B. (2001) *Molecular Fluorescence. Principles and Applications*, Wiley CH.
(133) Diaspro, A. (2002) *Confocal and Two-Photon Microscopy: Foundations, Applications and Advance,* Wiley-Liss.
(134) Lemasters, J. J., Chacon, E., Ohata, H., Harper, I. S., Nieminen, A. L., Tesfai, S. A., and Herman, B. (1995) Measurement of electrical potential, pH, and free calcium ion concentration in mitochondria of living cells by laser scanning confocal microscopy. *Methods Enzymol 260*, 428-44.

(135) Birge, R. (1986) Two-photon spectroscopy of protein-bound chromophores. *Acc. Chem. Res. 19*, 138-146.
(136) Kennedy, S. M., and Lytle, F. E. (1986) p-Bis(o-methylstyryl)benzene as a power-squared sensor for two-photon absorption measurements between 537 and 694 nm. *Anal. Chem. 58*, 2643-2647.
(137) Montes, L. R., Alonso, A., Goni, F. M., and Bagatolli, L. A. (2007) Giant unilamellar vesicles electroformed from native membranes and organic lipid mixtures under physiological conditions. *Biophys J 93*, 3548-54.
(138) Brückner, E., Sonntag, P., and Rehage, H. (2000) Influence of Toluene on the Bending Elastic Properties of Giant Phosphatidylcholine Vesicles. *J Phys Chem B 104*, 2311–2319.
(139) Dimova, R., Aranda, S., Bezlyepkina, N., Nikolov, V., Riske, K., and Lipowsky, R. (2006) A practical guide to giant vesicles. Probing the membrane nanoregime via optical microscopy. *J. Phys.: Condens. Matter 18*, 1151-1176
(140) Reeves, J. P., and Dowben, R. M. (1969) Formation and properties of thin-walled phospholipid vesicles. *J Cell Physiol 73*, 49-60.
(141) Estes, D. J., and Mayer, M. (2005) Electroformation of giant liposomes from spin-coated films of lipids *Colloids and Surfaces B: Biointerfaces 42*, 115-123
(142) Karlsson, M., Nolkrantz, K., Davidson, M. J., Strömberg, A., Ryttsén, F., Åkerman, B., and Orwar, O. (2000) Electroinjection of Colloid Particles and Biopolymers into Single Unilamellar Liposomes and Cells for Bioanalytical Applications. *Anal Chem 72*, 5857–5862.
(143) Angelova, M. I., and Dimitrov, D. S. (1986) Liposome electroformation. *Faraday Discuss. Chem. Soc. 81*, 303–11.
(144) Luisi, P. L., and Walde, P. (2000) *Giant Vesicles (Perspectives in Supramolecular Chemistry),* John Wiley & Sons Ltd.
(145) Dimitrov, D. S., and Angelova, M. I. (1988) Lipid swelling and liposome electroformation mediated by electric fields. *Bioelectrochem. Bioenerg. 19*, 323-336.
(146) Janosch, S., Nicolini, C., Ludolph, B., Peters, C., Volkert, M., Hazlet, T. L., Gratton, E., Waldmann, H., and Winter, R. (2004) Partitioning of dual-lipidated peptides into membrane microdomains: lipid sorting vs peptide aggregation. *J Am Chem Soc 126*, 7496-503.
(147) Nicolini, C., Baranski, J., Schlummer, S., Palomo, J., Lumbierres-Burgues, M., Kahms, M., Kuhlmann, J., Sanchez, S., Gratton, E., Waldmann, H., and Winter, R. (2006) Visualizing association of N-ras in lipid microdomains: influence of domain structure and interfacial adsorption. *J Am Chem Soc 128*, 192-201.
(148) Radovan, D., Opitz, N., and Winter, R. (2009) Fluorescence microscopy studies on islet amyloid polypeptide fibrillation at heterogeneous and cellular membrane interfaces and its inhibition by resveratrol. *FEBS Lett 583*, 1439-45.
(149) Estes DJ , M. M. (2005) Electroformation of giant liposomes from spin-coated films of lipids *Colloids and Surfaces B: Biointerfaces 42*, 115-123
(150) Schmitz, S. (2007) *Der Experimentator: Zellkultur* 1st ed., Elsevier.

(151) Mishra, R., Sellin, D., Radovan, D., Gohlke, A., and Winter, R. (2009) Inhibiting islet amyloid polypeptide fibril formation by the red wine compound resveratrol. *Chembiochem 10*, 445-9.
(152) Berridge MV, T. A., McCoy KD, Wang R. (1996) The biochemical and cellular basis of cell proliferation assays that use tetrazolium salts. *Biochemica 4*, 15-19.
(153) Munishkina, L. A., and Fink, A. L. (2007) Fluorescence as a method to reveal structures and membrane-interactions of amyloidogenic proteins. *Biochim Biophys Acta 1768*, 1862-85.
(154) Khurana, R., Coleman, C., Ionescu-Zanetti, C., Carter, S. A., Krishna, V., Grover, R. K., Roy, R., and Singh, S. (2005) Mechanism of thioflavin T binding to amyloid fibrils. *J Struct Biol 151*, 229-38.
(155) Tatarek-Nossol, M., Yan, L. M., Schmauder, A., Tenidis, K., Westermark, G., and Kapurniotu, A. (2005) Inhibition of hIAPP amyloid-fibril formation and apoptotic cell death by a designed hIAPP amyloid- core-containing hexapeptide. *Chem Biol 12*, 797-809.
(156) Dzwolak, W., Ravindra, R., Lendermann, J., and Winter, R. (2003) Aggregation of bovine insulin probed by DSC/PPC calorimetry and FTIR spectroscopy. *Biochemistry 42*, 11347-55.
(157) Gorovits, B. M., and M., H. P. (1998) High Hydrostatic Pressure Can Reverse Aggregation of Protein Folding Intermediates and Facilitate Acquisition of Native Structure. *Biochemistry 37* 6132–6135.
(158) Richard, J., Carpenter, F., and Theodore, R. (1999) High pressure fosters protein refolding from aggregates at high concentrations. *PNAS 96*, 13029-13033
(159) Marzban, L., Trigo-Gonzalez, G., Zhu, X., Rhodes, C. J., Halban, P. A., Steiner, D. F., and Verchere, C. B. (2004) Role of beta-cell prohormone convertase (PC)1/3 in processing of pro-islet amyloid polypeptide. *Diabetes 53*, 141-8.
(160) Levy, M., Porat, Y., Bacharach, E., Shalev, D. E., and Gazit, E. (2008) Phenolsulfonphthalein, but not phenolphthalein, inhibits amyloid fibril formation: implications for the modulation of amyloid self-assembly. *Biochemistry 47*, 5896-904.
(161) Conte, A., Pellegrini, S., and Tagliazucchi, D. (2003) Effect of resveratrol and catechin on PC12 tyrosine kinase activities and their synergistic protection from beta-amyloid toxicity. *Drugs Exp Clin Res 29*, 243-55.
(162) Jang, J. H., and Surh, Y. J. (2003) Protective effect of resveratrol on beta-amyloid-induced oxidative PC12 cell death. *Free Radic Biol Med 34*, 1100-10.